GEOLOGICAL, PETROLOGICAL AND GEOCHEMICAL INVESTIGATION OF THE c. 3.45 Ga STOLZBURG TTG PLUTON AT CRUSHERS' QUARRY, BARBERTON GREENSTONE BELT, SOUTH AFRICA

THATO MOFAMMERE

Thesis submitted to the Department of Geology, Rhodes University in fulfilment of the requirements for the degree of

MASTER OF SCIENCE

November 2024

Supervised by Doctor Eugene Grosch

Abstract

This study investigates the tonalite-trondhjemite-granodiorite (TTG) suite and associated amphibolite xenoliths of the Stolzburg pluton at Crushers' Quarry in the Barberton Granitoid-Greenstone Terrain, South Africa. Through detailed field mapping, petrography, geochemical analysis, $\delta^{18}O$ investigation of quartz, and U-Pb zircon geochronology, the petrogenesis and geodynamic context of these Archean rocks were explored. Five major lithologies were identified: Coarse-grained trondhjemites, medium-grained tonalites, fine-grained tonalites, granodiorite sheets, and amphibolite xenoliths. Field evidence, including cross-cutting relationships, indicates that the coarse-grained trondhjemites intruded as the earliest phase, followed by medium-grained tonalites, which were then followed by fine-grained tonalites, and finally, granodiorite sheets, which represent the latest intrusive phase.

Petrographic analysis reveals mineralogical differences between the trondhjemites and tonalites, with trondhjemites lacking hornblende and having lower mafic mineral content. Geochemical data support the interpretation that the TTGs formed through partial melting of variably hydrated metabasaltic sources (possibly at depth in the garnet stability field). The metabasaltic melt incorporated varying proportions of older, intermediate trondhjemite crust and volcaniclastic sediments during ascent and emplacement to form the Stolzburg pluton TTG suite of rocks.

Elevated (above mantle) $\delta^{18}O$ quartz values of the Stolzburg pluton TTG rocks ranging between 8.72 to 9.71‰ combined with it's strongly peraluminous geochemical composition indicate the presence of an ancient crustal component that was assimilated into the metabasaltic melt source(s). It is proposed that a number of petrogenetic factors controlled the composition of the Stolzburg TTG rocks, including composition of the metabasalt source, degree of hydration of the metabasalt source and the extent of crustal contamination with older, pre-existing intermediate composition rocks. A possible candidate for the crustal contamination component could be the older 3.509 Ga Steynsdorp trondhjemite as well as ancient volcaniclastic sediments in the greenstone belt. The protolith to the amphibolite xenoliths occurring within the TTG suite are geochemically characterized as komatiitic basalt, recording either a subduction zone or crustal contamination geochemical signature.

U-Pb zircon dating of the coarse-grained trondhjemites and medium-grained tonalites yield Concordia ages of 3429.9 ± 12 Ma (2σ) and 3414.0 ± 14 Ma (2σ), respectively. These

Concordia ages represent an estimate of the igneous crystallization ages of the zircons and confirm that these TTGs were emplaced in close temporal succession. The U-Pb zircon ages are comparable to those in the published literature, although one sample with a significantly younger age is attributed to zircon open-system Pb-loss in complex early Archean zircons and also challenges with the LA-ICP-MS analytical technique used.

The depth of metabasalt melting is not constrained in this study, similar to recent studies on early Archean TTGs. Various TTG geodynamic settings are explored ranging from melting at the base of a thick oceanic plateau to generation at depth in a subduction zone. In light of recent regional field observations, metamorphic constraints, apatite thermochronological data, U-Pb detrital zircon data and greenstone belt metabasalt geochemistry, a model of TTG crust generation in an episodic proto-subduction zone, involving subcretion and tectonic imbrication of oceanic lithosphere at c. 3.45 Ga, is considered.

Declaration

I declare that this thesis is my own work and is being submitted in fulfilment for the Master of Science degree in the Department of Geology at Rhodes University.

THATO MOFAMMERE

Acknowledgements

The completion of this thesis marks a significant milestone in my academic journey, a journey that would not have been possible without the support, guidance and encouragement of numerous individuals.

Firstly, I would like to extend my deepest appreciation to my supervisor, Dr. Grosch. His support, insightful feedback and continuous encouragement have been very instrumental in shaping my research and analytical skills. I would like to show gratitude to him for not giving up on me and being patient when I would lose the motivation and enthusiasm to do my work. I must also acknowledge the funding support I received from him which made it possible for me to pursue my research without any financial burdens.

A heartfelt thank you to Dr. Mcloughlin from the Geology Department and Mrs Joyce Sewry from the Chemistry Department for mentoring me and guiding me; your advice and support did not go unnoticed. I am also grateful to Mr Thulani Royi from the Rhodes University Geology Department for preparing thin sections used in this project. My gratitude extends to Mrs Riana Rossouw and Mrs Mareli Grobbelaar from Stellenbosch University for assistance with producing the XRF major and trace element data used in this research. I would also like to thank Mrs Riana Rossouw of Stellenbosch University for producing zircon geochronology data for this project. I would like to thank Prof. Chris Harris (University of Cape Town) for providing TTG quartz oxygen isotope data.

I appreciate my parents, mme ‘Manthabeleng Mofammere and ntate Moeketsi Mofammere, for their unwavering support. They did not fail to check up on me and my progress at all times and I truly appreciate it. My siblings, nieces and nephews, all of you guys kept me going and I am immensely grateful.

Last but not least, I would like to thank my Geology Department colleagues; Bukho Charles and Siyasanga Dyan for keeping me sane throughout this entire journey. The discussions and laughs we had not only made this journey not only bearable but also enjoyable.

Table of Contents

1. INTRODUCTION

1.1 Overview of the Barberton Greenstone-Granitoid Terrain

The Barberton Greenstone-Granitoid Terrain (BGGT) represents one of the most well-preserved Archean terranes on Earth, with a geological record that extends back to ca. 3.5-3.1 billion years ago (Moyen *et al*., 2007). It is a low-grade sequence of greenstones surrounded by granitoids that forms the eastern margin of the Kaapvaal Craton (Brandl *et al*., 2006). The BGGT is approximately 120 x 50 km in extent and comprises a series of NE-SW striking antiforms and synforms and bedding surfaces that dip vertically or sub-vertically (Brandl *et al*., 2006). It comprises greenstone supracrustal rocks, which are surrounded by generations of tonalite-trondhjemite-granodiorite (TTG) plutons (Anhaeusser *et al*., 1983; de Wit *et al*., 2011).

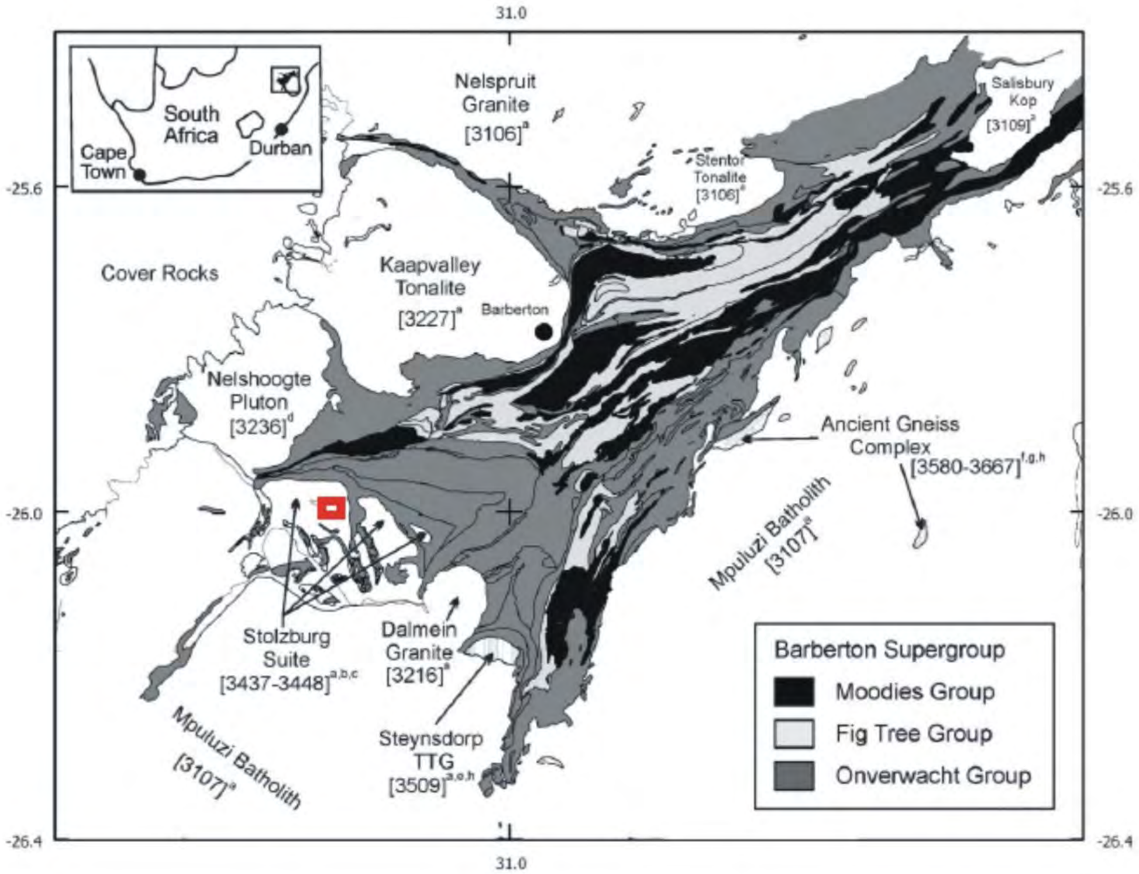

Figure 1.1 *A regional geological map of the Barberton Greenstone-Granitoid Terrain on the Kaapvaal Craton of South Africa (modified after Anhaeusser et al., 1983, Kamo and Davis, 1994). The three stratigraphic groups of the Barberton Supergroup are indicated along with the surrounding TTG plutons and labelled U-Pb zircon ages for various surrounding TTG gneisses and plutons (see Table 2.1 and references therein). The red inset box indicates the location of the study area.*

The BGGT can be sub-divided into four diachronous fault-bounded terranes that record early volcanic events and sedimentation (Anhaeusser, 2019; Byerly *et al.*, 2018). These terranes are the oldest Steynsdorp Block, located towards the south-east of the BGGT (Lowe, 1999 and Lowe & Byerly, 2007). The Steynsdorp block includes the ca. 3509 ± 8 Ma Steynsdorp trondhjemitic gneiss (Lowe, 1994; 1999). The Songimvelo Block includes the ca. 3460-3437 Ma Stolzburg TTG complex and greenstones of the Onverwacht Group (Lowe, 1994; 1999). The central Umuduha Block and the ca. 3227 Ma Kaap Valley Block are located to the north of the Inyoni-Inyoka fault system (Lowe, 1994; 1999, see Figure 2.1).

A unique feature of Barberton TTGs is that they represent a group of well-defined plutons that are relatively little deformed. With the exception of the Badplaas gneisses, they do not constitute a heterogeneous complex of orthogneisses (so-called grey gneisses) like many other TTG complexes that often are polyphase, highly strained, transposed and migmatitic (Moyen *et al*. 2007). The TTGs display various states of deformation and preservation (Moyen *et al*., 2007). Although the TTGs around Barberton are *sensu stricto* gneisses because they underwent solid-state deformation after emplacement, they still preserve their original magmatic textures (Moyen *et al*., 2007). This means that emplacement-related features and intrusive contacts are still preserved in places (e.g. Kisters and Anhaeusser, 1995a) and deformation did not result in transposition and development of a strong gneissic fabric.

The Granodiorite-Monzogranite-Syenogranite (GMS) suite, emplaced between 3140 and 3074 Ma, represents a significant phase of potassic magmatism in the (BGGT). This suite exhibits compositional heterogeneity, comprising syenites, quartz monzonites, and granites, reflecting a transition from Na-rich magmatism to K-rich magmatism (Anhaeusser and Robb, 1983; Robb *et al*., 2006; Chen *et al*., 2023). The GMS plutons are distributed across the BGGT and intrude the basement with sharp contacts, forming sub-horizontal, tabular bodies. Notable examples include the Boesmanskop Alkaline Complex (ca. 3107 ± 2 Ma), Mpuluzi Batholith (ca. 3105 ± 3 Ma), and Heerenveen Batholith (ca. 3105 ± 3 Ma) in the south, as well as the Nelspruit Batholith (ca. 3104 ± 3 Ma), Salisbury Kop Batholith (ca. 3109 ± 10 Ma), and the oldest GMS rocks in the Pigg's Peak Batholith (3144–3074 ± 4 Ma) to the north and east of the BGB (Kamo and Davis, 1994; Robb *et al*., 2006; Clemens *et al*., 2010; Moyen *et al*., 2021).

The Ancient gneiss complex (AGC) is a terrain that lies southeast of the BGGT and is separated from the BGGT rocks by a sheet-like granitoid pluton known as the Mpuluzi

Batholith (Kröner and Tegtmeyer, 1994). Unlike the BGGT TTGs, the rocks of the AGC are deformed and consists of migmatic granitoids (Kröner and Tegtmeyer, 1994).

1.2 What are tonalite-trondhjemite-granodiorite (TTG) plutons?

Tonalite-trondhjemite-granodiorite plutons are felsic to intermediate intrusive bodies that are usually associated with greenstone belts (Arndt, 2013; Moyen *et al*., 2007; Laurent, 2024). The dominant minerals in TTGs are quartz and different types of feldspars (Arndt, 2013; Moyen *et al*., 2007; Laurent, 2024). The main feldspar found in tonalites and trondhjemites is plagioclase; granites (*sensu stricto*) consist of alkali feldspar, but granodiorites can be made up of both alkali feldspar and plagioclase (Arndt, 2013; Moyen *et al*., 2007; Laurent, 2024). Mafic minerals such as biotite and hornblende are present in TTGs at modal proportions ranging from 20-40% (Arndt, 2013; Moyen *et al*., 2007; Laurent, 2024).

Trondhjemites of the BGGT plutons are leucocratic. They consist of 55-65% plagioclase, 15-20% quartz, ~10% microcline and <10% of mafic minerals with the dominant mafic mineral being biotite (Clemens e*t al.*, 2006). The accessory minerals present in trondhjemites include epidote, apatite, and chlorite. Tonalites of the BGGT plutons are also leucocratic and they are made up of ~ 60% plagioclase, 10-20% quartz, ~15% hornblende and minor microcline and biotite. The accessory minerals in tonalites are ilmenite and allanite (Moyen and Martin, 2012).

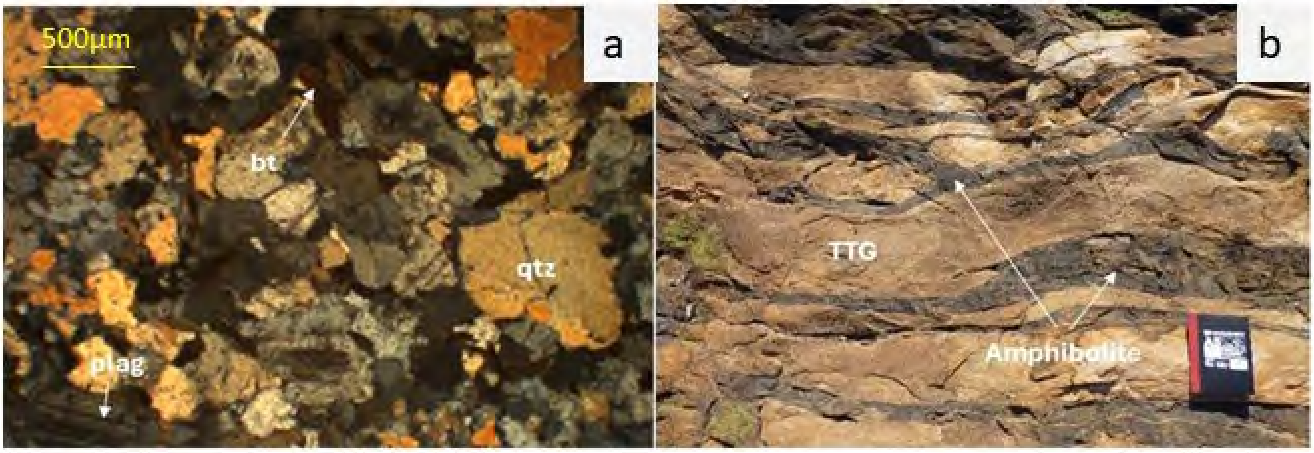

Figure 1.2*: (a) A photomicrograph showing the minerals that make up TTGs and (b) a picture of a TTG and amphibolite outcrop in Barberton, Mpumalanga (A5 notebook for scale).*

TTGs are thought to have formed predominantly during the Archean Eon, through partial melting of hydrated mafic crust, most likely in high-pressure environments, such as subduction zones or thickened lower oceanic plateau crust (Sun *et al*., 2021). These processes involved the melting of garnet-bearing amphibolite or eclogite, leaving a signature in the geochemistry of TTGs that reflects deep-crustal conditions (Sun *et al*., 2021).

1.3 Significance of TTGs

TTG plutons comprise a large portion of Archean cratons therefore they are regarded as the building blocks of the Earth's early continental crust (Clemens *et al*., 2006). TTGs are essentially lacking in the modern-day record, and they appear to be linked to the early part of the Earth's history, recording felsic magmatic processes that are special to the juvenile Earth (Sun *et al*., 2021). TTGs are therefore useful for understanding the thermal evolution of the Archean crust, geodynamic processes, and the evolution of the first landmasses. TTGs are important because their magmatism marks the first stages of continental differentiation where the mafic crust underwent partial melting to form a more evolved felsic crust (Clemens *et al*., 2006).

There remains much controversy concerning exactly how TTGs form, and these various models will be reviewed below, but it is widely accepted that they involve the melting of meta-mafic (greenstone) rocks (Sun *et al*., 2021; Foley *et al*., 2003). It is argued that the Earth in the Archean had higher mantle temperatures (Herzberg, 1992; Sun *et al*., 2021; Foley *et al*., 2003), and the oceanic crust was ~5km thicker than it is in the modern day. The bulk composition of the oceanic crust was also different from the recent, containing a higher proportion of magnesium (Arndt, 2013). Geodynamic processes on the early Earth are also argued to have been different (due to a likely hotter mantle); the nature and timing of the onset of horizonal, modern-style plate tectonic processes are debated (e.g. see Rey *et al*., 2024).

1.4 Geochemical Features and Classification

The continental crust is predominantly felsic in composition and consists of quartz and feldspar minerals. The continental crust is therefore rich in the alkali metals calcium, sodium, potassium, and silicon. However, the Archean continental crust, had a higher sodium content and very low potassium content (Sun *et al*., 2021).

TTGs are typically enriched in sodium, with high sodium to potassium ratios and show a characteristic depletion in heavy rare earth elements (HREEs) such as Yb and Lu, which is indicative of melting in the presence of garnet (Moyen *et al*., 2007; Rapp *et al*., 1991). TTGs also display high Sr/Y and La/Yb ratios which are used as key discriminants when classifying TTGs according to their formation pressures (Moyen *et al*., 2011). Detailed geochemical studies have classified Archean TTGs into three groups interpreted to be low, medium, and high pressure TTGs, although the three groups form a continuous evolution (Moyen, 2011). The low-pressure subseries shows relatively low Al_2O_3, NaO_2, Sr content and relatively high Y, Yb, Ta, and Nb content; the lower Sr/Y and La/Yb ratios reflect shallow melting depths. The high-pressure group shows the opposite geochemical features, with higher Sr/Y and La/Yb ratios which are indicative of deep melting depths (Moyen *et al*., 2011). The medium-pressure group has transitional features between the high- and low- pressure endmember groups and is the most abundant among the three groups (Moyen *et al*., 2011).

1.5 Models of TTG Generation

It is widely accepted that TTGs form from melts of mafic rocks, mostly amphibolites (Moyen *et al*., 2007; Foley *et al*., 2002). However, there are contrasting views on the geodynamic settings under which TTGs are formed (Foley *et al*., 2002). In particular, the depth of melting and the mineralogy of the source, for example, amphibolite melting at less than 15 kbar (Foley *et al*., 2002) versus eclogites melting at more than 15-20 kbar (Rapp *et al*., 2003).

A basaltic source, water, and heat are the essential components required to form TTGs. Two commonly proposed end-member geodynamic models have been suggested, as outlined by Sun *et al*., (2021), to explain the origin of TTGs: the subduction model shown in Figure 1.3 and the delamination model shown in Figure 1.4.

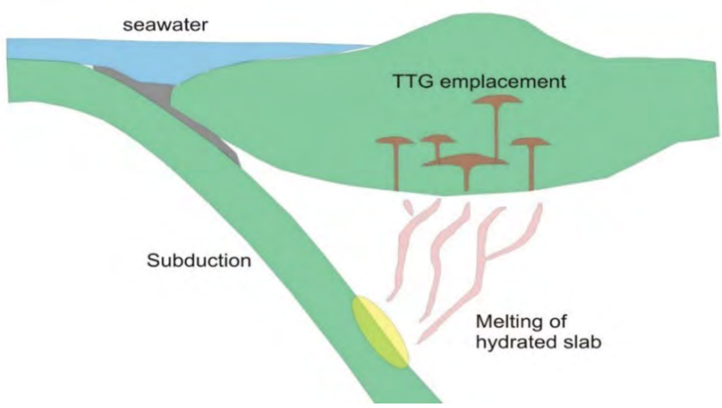

Figure 1.3: *Generation of TTGs by melting of subducting oceanic slab (modified after Sun et al., 2021).*

According to Foley *et al*., (2003) mantle temperatures dropped in the late Archean; thus, the oceanic crust cooled. The cooling of the crust allowed for the onset of subduction because the oceanic crust was dense enough to bend and subduct beneath the more buoyant mantle (Arndt, 2013). The main TTG forming components, namely basalts, heat, and water are all available in subduction zones (Arndt, 2013).

At spreading centres, the oceanic crust migrates away from the mid-oceanic ridge (Arndt, 2013). The crust cools and thickens to the point where the mantle becomes more buoyant than the crust (Reymer and Schubert, 1984; Arculus, 1994; Rudnick,1995; Hamilton, 1995; Arndt, 2013). The oceanic crust also interacts with the seawater, further cooling it down. When the oceanic crust has cooled enough it is ready to subduct (Reymer and Schubert, 1984; Arculus, 1994; Rudnick,1995; Hamilton, 1995). The down going slab bends as it subducts and as it bends, the sea water percolates through fractures thus hydrating the oceanic crust (Arndt, 2013; Foley *et al*., 2003). When the crust reaches depths between 20-160 km, the high temperatures cause the breakdown of serpentine, chlorite, amphibole and the dewatering of sediments (Reymer and Schubert, 1984; Arculus, 1994; Rudnick,1995; Hamilton, 1995; Moyen *et al*., 2007). The fluids are released into the mantle wedge and the fluids in the mantle wedge promote fluid fluxed melting of the overlying mantle peridotites. The buoyant mantle melts rise to the base of the crust where they are homogenized into magmas of tonalitic and trondhjemitic composition (Foley *et al*., 2003).

Foley *et al*., (2002) suggests that TTGs form from melts of garnet amphibolites that have low Mg and not from eclogites, but this hypothesis is insufficient because regardless of the source, the pressures at which TTG melts are produced can be achieved in other settings such as collisional/volcanic thickening of oceanic crust. There are also complexities in explaining how the subducting slab is able to hold the water necessary for TTG formation to the depths required for melting, and how the melts from the subducting slab can ascend to emplacement levels without being consumed by the peridotite in the mantle wedge (Rapp *et al*., 1999; Proteau *et al*., 2001).

Adakites, which are modern slab melts, have high MgO and Mg# thus suggesting that the adakites reacted with the mantle wedge peridotites while travelling through the mantle (Rapp *et al*., 1999). Smithies (2000) compared the major elements of Archean TTGs with those of adakites, which are intermediate to felsic rocks that form by slab melting. Adakites have higher

MgO contents than TTGs because adakite melts interact with mantle rocks. The low MgO content of TTGs suggest that they form at a different geodynamic setting, where they are emplaced without having to travel through the mantle, or that the mantle wedge was not developed or slab melting occurred at shallow depth because of high temperatures in the Early Archean (Martin *et al*., 2005).

Earliest Archean 4.0 Ga old TTGs have low MgO and Mg# in comparison to 3.4-2.5 Ga old TTGs which suggests that before 3.4 Ga, the mantle wedge was very thin; hence, there was little to no interaction of the slab melts with the mantle wedge peridotites (Martin *et al*., 2005).

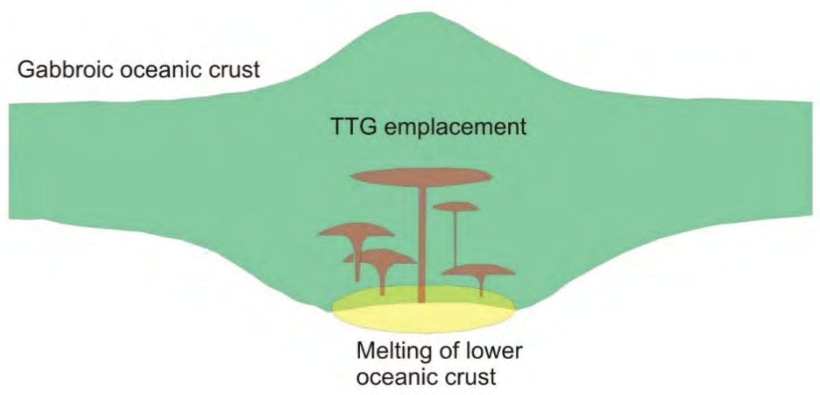

Figure 1.4: *Generation of TTGs by melting of the lower oceanic crust (Modified after Sun et al., 2021)*

The delamination model shown in Figure 1.4 explains another possible model of TTG formation. The oceanic crust is argued to have been thicker than the present-day oceanic crust by ~ 5km in the early Archean (Arndt, 2013). This vertical tectonic model suggests that the crust was too thick to bend and subduct, and instead the thicker lower oceanic crust would become heated by the mantle below it whilst also being incubated by the mafic upper crust. When the ultramafic cumulates layer is removed by delamination, the middle crust is exposed and becomes heated by the mantle producing TTG melts (Sun *et al*., 2021).

Apart from the two end-member models that are described above, there are other models that have been proposed by other researchers which challenge the widely accepted subduction and delamination models.

Reimink *et al*. (2016) propose Iceland-like settings as geodynamic model for the generation of TTG suites. This study suggests that processes in plume-influenced, rift-dominated settings could produce TTGs. Reimink *et al*. (2016) argue that the geochemical characteristics of TTGs, such as high Sr/Y and La/Yb ratios, which are interpreted as evidence for high-pressure melting in subduction zones, can also be generated through partial melting of hydrated mafic crust in rift settings. In a rift setting, mantle plumes induce extensive crustal melting, producing large volumes of mafic magmas that subsequently undergo fractional crystallization and remelting to generate TTG-like compositions (Reimink *et al.*, 2016). This process is facilitated by the presence of water, which lowers the melting temperature of mafic protoliths and promotes the production of felsic melts.

Kendrick and Yakymchuk (2020) critically evaluate the geochemical and petrogenetic processes influencing Archean TTGs, challenging the subduction and delamination models. Their study demonstrates that garnet fractionation during melt migration and melt loss complicate the link between TTG geochemistry and tectonic settings. Garnet fractionation during melt migration can produce HREE-depleted signatures, which are interpreted as evidence for high-pressure melting in subduction zones due to residual garnet (Kendrick and Yakymchuk, 2020). Melt loss from a crystallizing system also changes trace element ratios (e.g. La/Yb, Sr/Y), to those associated with increasing melting depth. The bulk composition variations in metabasalt protoliths also generate geochemical diversity in TTGs independent of melting pressure (Kendrick and Yakymchuk, 2020).

Studies by Kamber (2015) also suggest alternative models for TTG genesis where the melting of basaltic oceanic plateaus occurred under gravitational overturn or mantle plume-induced heating (Bédard, 2006; Johnson *et al*., 2017). In such cases, the basaltic protoliths would have been buried to eclogite-facies depths (>40 km) by crustal thickening through volcanic loading (Van Kranendonk *et al.*, 2014). This mechanism could explain the association of TTGs with greenstone belts, which may represent residues of partial melting. A transitional model reconciles these views, suggesting that early Archean TTGs (pre 3.0 Ga) formed predominantly in non-subduction settings, while late Archean TTGs (post 3.0 Ga) reflect subduction zones as plate tectonics began to emerge (Kamber, 2015; Smit *et al*., 2019).

Johnson *et al*. (2019) illustrate a shift in TTG geochemistry from the Eoarchean to Neoarchean. Early Archean TTGs (pre 3.0 Ga) are characterized by high Sr/Y and La/Yb ratios, indicative of partial melting at depths >40 km where garnet is stable in the residue, while amphibole is absent (Martin, 1987; Moyen, 2011). These signatures align with melting of hydrous metabasaltic crust under eclogite to garnet amphibolite-facies conditions, likely within thickened mafic crust (Johnson *et al*., 2019). In contrast, post 3.0 Ga TTGs exhibit lower Sr/Y ratios and elevated Mg# values, suggesting shallower melting environments with residual amphibole and plagioclase, these features are consistent with modern subduction zone processes (Smithies *et al*., 2009; Johnson *et al*., 2019). This research concludes that Archean geodynamics for TTG production were transitional, with early crustal growth dominated by deep crustal melting, followed by the progressive incorporation of subduction processes after 3.0 Ga.

1.6 TTGs in the Barberton Greenstone Granitoid Terrain

The TTGs of the BGGT are predominantly associated with four major plutonic complexes: the 3.5 Ga, 3.45 Ga, 3.23 Ga and 3.1 Ga. It is found that the ca. 3.45 Ga TTGs (e.g. Stolzburg TTG) are in the east, and the younger 3.23 Ga old plutons (e.g. Kaap Valley Pluton) are in the west, separated from one another by the Inyoni shear zone, which is interpreted to represent a suture zone, formed during ca. 3.25-3.21 Ga orogenesis (Lowe *et al*., 1999; Moyen, 2007; Kisters *et al*., 2010).

The TTGs are divided into two sub-series: a Sr-rich commonly trondhjemitic series and a Sr-poor commonly tonalitic series (Moyen *et al*., 2007). It is reported that the 3.45 Ga TTG generation is only trondhjemitic, whereas the 3.29-3.21 Ga plutons are both trondhjemitic and tonalitic; and in this group the tonalites always represent the youngest phases (Moyen *et al*., 2007; Kisters *et al*., 2010). The switch from trondhjemitic (3.29-3.22 Ga) to tonalitic (3.22-3.21 Ga) compositions at ca. 3.22 Ga has been argued to coincide with a change in geological regime from collision tectonics to orogenic collapse. Moreover, it has been proposed that the two distinct “sub-series” of the BGGT could reflect two different geodynamic environments for their formation, namely formation at the base of a thickened crust, and derivation from a subducting slab (Reymer and Schubert, 1984; Arculus, 1994; Rudnick,1995; Hamilton, 1995; Moyen et al., 2007). These models will be explored in this thesis, but firstly the characteristics of these different TTGs will be summarized.

The ca. 3.55-3.50 Ga plutons (e.g Steynsdorp Pluton) are located on the eastern part of the BGGT (Robb and Anhaeusser,1983; Kröner *et al.*, 1996). They occur mostly as banded gneisses that have a tonalitic protolith (Moyen *et al.*, 2007). The Steynsdorp pluton outcrops in a domal or antiform structure (Kisters and Anhaeusser, 1995b), and its contact with the surrounding supracrustal rocks of the Theespruit Formation is tectonic in nature (Moyen *et al*., 2007).

The ca. 3.45 Ga plutons are located on the southern part of the BGGT (Moyen *et al*., 2007; Kamo and Davis, 1994; Dziggel *et al*., 2002). They are known as the Stolzburg TTG terrane (Moyen *et al*., 2007). The two most prominent plutons of the Stolzburg terrane are the Stolzburg pluton studied here and the Theespruit pluton (Robb and Anhaeusser,1983; Kröner *et al*., 1996). These plutons occur with another small pluton which is the Doornhoek pluton. Further south of the BGGT are other small plutons namely: the Eerstehoek, Honingklip, Theeboom and Weergevonden plutons (Robb and Anhaeusser,1983; Kröner *et al.,* 1996). The Stolzburg terrane/block is truncated by the Komati fault to the north, and it is bounded by the Inyoni-Inyoka shear zone to the west (Robb and Anhaeusser,1983; Kröner *et al.*, 1996).

The ca. 3.29-3.24 Ga TTGs are represented by the Badplaas gneisses and the Batavia pluton (Moyen *et al*., 2007; Kisters *et al*., 2010). The Kaap Valley pluton represents the ca. 3.23-3.22 Ga plutons that occur on the other margin of the BGGT. This TTG complex is located in the central part of the BGGT. It consists mostly of coarse-grained tonalites (Moyen *et al*., 2007). The Kaap Valley pluton differs from the Stolzburg and Theespruit suites, exhibiting lower Na_2O content and less pronounced HREE depletion. The Kaap Valley TTG suite is characterized by lower Sr/Y and La/Yb ratios compared to older TTG plutons, suggesting a shallower depth of formation (Robb *et al*., 1986). Its geochronological and geochemical characteristics indicate that it formed later in the evolutionary history of the BGGT (Robb *et al*., 1986).

The ca. 3.1 Ga plutons include the Mpuluzi batholith, Heerenveen Pluton, Pigg’s Peak pluton, Stenton Pluton and Nelspruit Pluton. These plutons are made up of sheet-like intrusions that predominantly comprise granite and syenite.

The focus of this MSc project will be on the Stolzburg TTG pluton which is located on the south-western margin of the BGGT (Anhaeusser *et al*., 1983). The Stolzburg Pluton is considered to consist of trondhjemite, and it is associated with the Theespruit Pluton and other smaller TTG plutons. These TTG plutons are coherently referred to as the Stolzburg Complex (Anhaeusser *et al*., 1983).

1.7 The Stolzburg Pluton

This MSc study focuses on the Stolzburg TTG Pluton of the BGGT. Further information on the Barberton TTGs is provided in the Regional Geology Chapter 2 of this thesis. The Stolzburg TTG pluton is one of the oldest TTG bodies in the BGGT, dating from ~ 3.460-3.437 Ga (Kamo and Davis, 1994; Dziggel *et al*., 2002). It is reported to consists of medium- to coarse-grained trondhjemite with some minor dioritic dykes on the margins of the pluton (Moyen *et al*., 2007). The Stolzburg Pluton is interpreted to have intruded under brittle conditions because the contacts between the BGGT and the pluton are well preserved (Moyen *et al*., 2007). The Stolzburg Pluton like other TTGs of the BGGT has undergone deformation processes after its intrusion but it still preserves its emplacement textures and features in some areas (Moyen *et al*., 2007). Fresh outcrops of the Stolzburg Pluton are exposed on the wall and floor of Crushers' Quarry that is to the west of Elukwatini (see Map in Figure 1.1).

These recently discovered exposures reported in this MSc thesis contain very fresh TTG and amphibolite xenoliths that will enable petrological studies that are not possible on other TTG pluton outcrops that have experienced greater degrees of alteration and weathering. These studies will include geological mapping of the internal structures in the Stolzburg pluton, petrographic investigation, bulk rock major and trace elemental geochemistry, oxygen stable isotope studies of quartz and zircon U-Pb geochronology. The aims and objectives of these geological and petrological investigations are explained in more detail below.

1.8 Objectives

This MSc project will investigate the geology, petrology, ad geochemistry of the Stolzburg TTG pluton at Crusher's Quarry with the following objectives.

- This study will involve conducting high-resolution geological mapping of exposed felsic and amphibolite rock types at Crushers Quarry to characterize in detail the internal geological structure of the Stolzburg TTG pluton. The aim of this study is to investigate lithological contacts between the amphibolite xenoliths and felsic rocks as well as to understand the field relationships between amphibolites and felsic rocks. Additionally, the study will determine intrusive relationships between the various felsic rock types.
- A detailed petrographic description of each of the rock types encountered will be carried out to characterize both the magmatic and metamorphic assemblages present.
- Geochemical characterization of the fresh rock types will be undertaken using major, trace and rare-earth element whole-rock data in order to identify the protolith (e.g., tonalite, trondhjemite, amphibolite). Geochemical compositional data will be

integrated with field observations, petrography, and regional data to provide a clear understanding of the rocks' origins and relationships.

- Stable oxygen isotope composition of tonalite, trondhjemite and granodiorite quartz will be analyzed as mineral separate to determine the $\delta^{18}O$ of mantle/protolith source characteristics.
- U-Pb age dating will be perfomed on zircon separates from selected TTG rocks by LA-ICPMS (Laser ablation inductively coupled plasma mass spectrometry).
- The field, petrographic, geochemical and geochronological data will be combined to reconstruct the internal geological structure and geological history of the Stolzburg TTG pluton.
- The petrological data will be compared to regional literature data on the Stolzburg pluton in order to assess current petrogenetic and geodynamic models.

1.9 Motivation and rationale

This study aims to conduct a detailed geological, petrological, and geochemical investigation of the Stolzburg Pluton to refine our understanding of the formation and evolution of the pluton using the well-exposed outcrops at Crushers' Quarry.

The Stolzburg Pluton is part of a complex suite of plutonic rocks that record multiple magmatic pulses during the Archean. By examining field relationships and textures within the pluton, this study seeks to identify distinct magmatic pulses and their emplacement history. Understanding these pulses will provide insights into the time and mechanisms of crustal growth during the early Archean.

TTGs are globally recognized as the building blocks of Archean continental crust, but their formation processes remain debated. This study will focus on the local geological setting of the Stolzburg Pluton to determine whether it formed through partial melting of hydrated basaltic crust in a subduction zone setting or through other mechanisms such as crustal thickening or mantle plume activity. By combining field observations with geochemical and isotopic data, this study will attempt to constrain the local geodynamic environment of the Stolzburg TTG Pluton.

The Stolzburg Pluton exhibits a range of compositions, from tonalites to trondhjemites to granodiorites, which possibly reflect variations in the source and melting conditions. This study will conduct petrological and geochemical analyses to characterize the pluton's mineralogy, major and trace element geochemistry, and isotopic signatures. The data will be combined and used to infer the petrogenetic origin (e.g. nature of the source rocks, melting conditions) of the Stolzburg TTG pluton. The Stolzburg TTG pluton provides a window into the processes that shaped the early continental crust. By investigating this pluton on a local scale, this study aims to contribute to the broader discussions on the formation of the early Archean continental crust.

2 REGIONAL GEOLOGY

2.1 Overview of the Geology of the Barberton Greenstone-Granitoid Terrain

2.1.1 Greenstone supracrustal sequence

The Barberton Supergroup is a stratigraphic sequence of volcano-sedimentary rocks that, together with the surrounding TTG intrusions, forms the ca. 3.5-3.1 Ga Barberton Greenstone-Granitoid Terrane (BGGT) (Lowe and Byerly, 1999). The supracrustal rocks of the BGGT are well preserved and mostly low-grade volcano-sedimentary rocks of the Barberton Supergroup (Lowe and Byerly, 1999). The Barberton Supergroup is divided into three lithostratigraphic groups: the Onverwacht Group, the Fig Tree Group and the Moodies Group (Lowe and Byerly, 1999, see Figure 2.1).

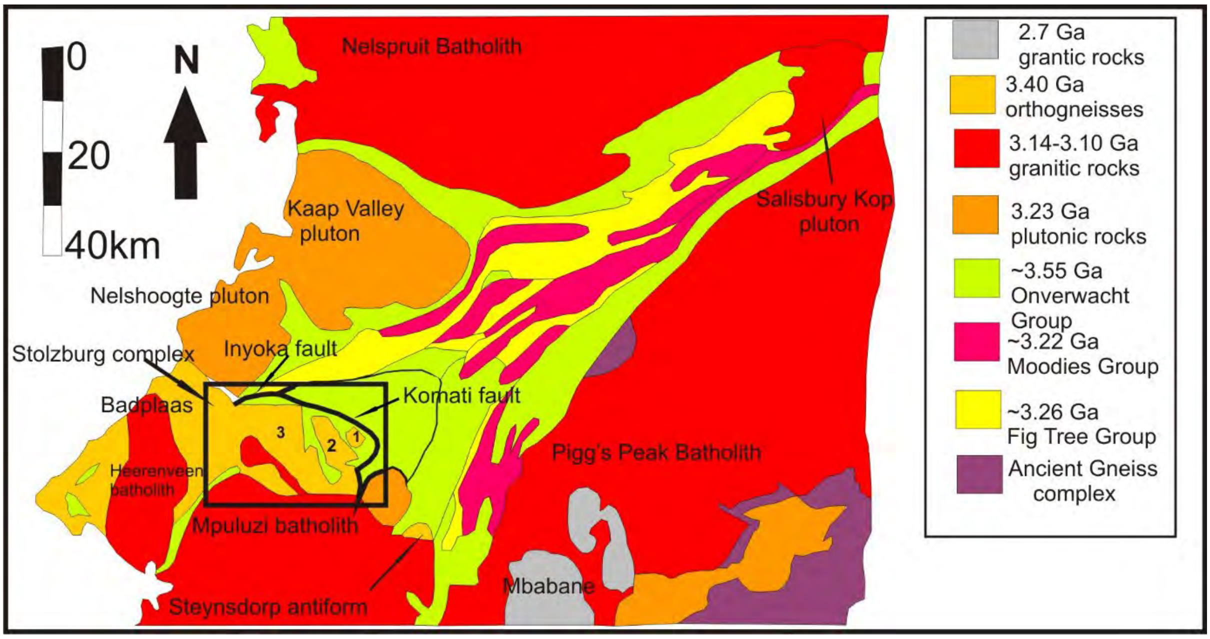

Figure 2.1. *A regional geologic map of the Barberton Greenstone Belt and surrounding TTG plutons. Map modified after Schoene et al., (2008). Black insert box shows the Stolzburg Complex with: 1-Doornhoek Pluton, 2-Theespruit Pluton and 3-Stolzburg Pluton.*

The ca. 3530-3334 Ma Onverwacht Group is located on the northern and southern parts of the BGGT, and it comprises ultramafic and mafic volcanic rocks that occur with silicified metasedimentary rocks and minor felsic rocks such as basalts and komatiites (Figure 2.2; Lowe and Byerly, 1999). The ca. 3258-3226 Ma argillaceous Fig Tree Group is overlain by the Moodies Group, and it is also a sedimentary succession that comprises shales, greywackes, cherts, banded iron formations and some dacitic lavas (Lowe and Byerly, 1999). The ca. 3230-

3110 Ma arenaceous Moodies Group comprises coarse-grained sedimentary rocks such as shales, conglomerates, marine to fluvial sandstones and thin units of basalt (Lowe and Byerly, 1999).

Notable in the Onverwacht Group are komatiitic lava flows, which are characterized by high magnesium content and low silica, reflecting the high temperature conditions of early mantle-derived magmas (Arndt, 1983). The Onverwacht Group is divided into two subgroups, the lower Tjakastad Subgroup and the upper Geluk Subgroup (Anhaeusser *et al*., 1969; Armstrong *et al*. 1990). The lower Tjakastad Subgroup has been divided further into three formations, the Sandspruit, Theespruit and Komati Formations, whereas the Geluk has been subdivided into the Hooggenoeg, Noisy, Kromberg and Mendon Formations (see Grosch *et al*., 2011; Viljoen and Viljoen 1969).

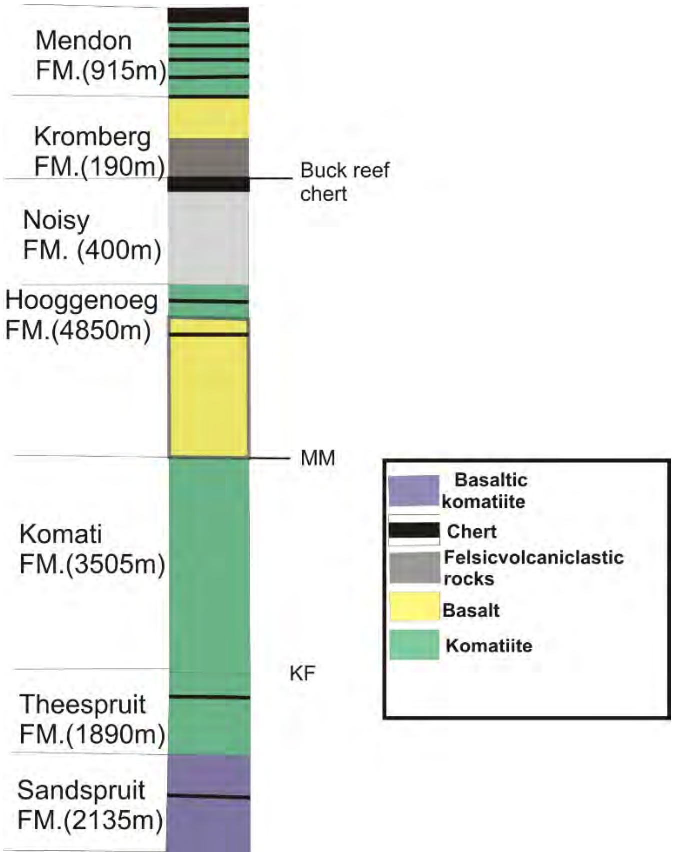

***Figure 2.2**. A simplified stratigraphic sequence of the Onverwacht Group (modified after Knauth and Lowe, 2003).*

The Sandspruit Formation is stratigraphically the lowest and oldest formation which consists of basaltic komatiites and some units of metasedimentary rocks such as cherts and calc-silicates

(Viljoen and Viljoen, 1969). The Sandspruit Formation occurs as xenoliths that are within TTG plutons (Lowe and Byerly, 2007). The Theespruit Formation consists of komatiites, tuffs, cherts as well as aluminous schists (Viljoen and Viljoen, 1969; Grosch *et al*., 2011). Rocks from the Sandspruit and Theespruit Formations have been metamorphosed under amphibolite facies conditions of 500-700°C, 0.6-1.2 GPa (Diener *et al*., 2005; de Wit *et al*., 2011). The Sandspruit and Theespruit Formations are intruded by c. 3440-3460 Ma TTG plutons which are the Theespruit, Stolzburg plutons and other smaller plutons which include the Theeboom, Eerstehoek, and Doornhoek plutons (Viljoen and Viljoen, 1969; Kamo and Davis, 1994).

The Theespruit Formation is truncated by the Komati fault which separates these amphibolite facies rocks from the overlying greenschist facies Komati Formation rocks (Dann, 2000). The Komati fault hosts deformed ca. 3.45 Ga tonalite sills which suggest that the fault was an area of weakness at the time of intrusion (Dann, 2000). The Komati Formation is made up of a succession of olivine komatiites, pyroxene komatiites, komatiitic basalts and tholeiitic basalts (Grosch and Slama, 2021).

The Komati Formation is a ~3 km section that divided into a lower sequence which comprises spinifex textured and serpentinized komatiite as well as tholeiitic metabasalt and an upper sequence comprising pillowed metabasalts (Viljoen & Viljoen, 1969a; Dann, 2000; Grosch *et al*, 2011). Mafic to ultramafic dykes and sills crosscut the Komati Formation. Zircons from volcaniclastic interflow sediments in the mid-lower Komati Formation have been dated to 3472 ± 5 Ma (Armstrong *et al*., 1990) and 3482 ± 2 Ma (Dann, 2000).

The Middle Marker Chert Formation situated stratigraphically above the Komati Formation is a ~10 m thick silicified volcaniclastic sequence. (Viljoen and Viljoen, 1969, de Wit *et al*., 2011). The Middle Marker comprises lapilli tuffs and the top part of the formation comprises black translucent or pale green chert (Lanier and Lowe, 1982). The Middle Marker is dated at 3472 ± 6 Ma based on U-Pb zircon geochronology (Armstrong *et al*., 1990).

The Hooggenoeg Formation, that stratigraphically overlies the Middle Marker Chert, is a ~2.5-3.0 km section divided into upper and lower sections (Dann, 2000) The lower Hooggenoeg Formation comprises well-preserved komatiitic and tholeiitic basalts interlayered with cherts (Dann, 2000; Nijman and de Vries, 2014). These earlier volcanic sequences are crosscut by mafic to ultramafic sills that hint at continued magmatic activity in a tectonically active rift or back-arc basin (Dann, 2000; de Wit *et al*., 2011). The upper section is made of thick felsic (dacitic to rhyodacitic) intrusions and volcaniclastic sediments, collectively referred to as the H6 upper unit. Zircons from these felsic rocks yield U-Pb ages between 3416 and 3455 Ma, are thought to be co-magmatic with the ca. 3460–3437 Ma Stolzburg TTG complex (Byerly *et al*., 1996; de Wit *et al*., 1987a,b; Kamo and Davis, 1994). The formation also includes chert layers and minor banded iron formations (BIFs) (de Wit *et al*., 2011).

The Noisy Formation overlies the Hooggenoeg Formation comprising ~1-2.5 km thick dacites and ~400 m thick volcaniclastic units (Grosch *et al*., 2011; de Wit *et al*., 2011). The entire sequence is overlain by a ~600 m thick succession of banded chert and banded iron formations known as the Buck Ridge Chert (de Wit *et al*., 2011; Viljoen and Viljoen, 1969a,b). The Noisy Formation is interpreted to represent a shallow marine near-shore environment that grades upward into a turbidite succession (Grosch *et al*., 2011). The Noisy Formation formed in a high-energy depositional setting with high sedimentation rates, primarily from clastic material eroded from surrounding TTG plutons, dacite and rhyolite intrusions (Grosch *et al*., 2011).

The Kromberg Formation is a prominent unit within the upper Onverwacht Group and is exposed on both the northwestern and southeastern limbs of the Onverwacht Anticline. It is characterized by alternating layers of basaltic and komatiitic lava flows, (Viljoen and Viljoen, 1969). The middle of the Kromberg Formation is intruded by mafic-ultramafic rocks and the uppermost section of the Kromberg Formation is made up of the ~15 m thick Footbridge Chert (Lowe and Byerly, 1999; Dann and Grove, 2007). Lowe and Byerly, (1999a, 2000) have dated the Kromberg Formation to ~3334 Ma based on zircon ages from the Footbridge Chert. Grosch *et al*. (2020) reinterprets the Kromberg Formation, emphasizing that the majority of the rocks are extrusive in origin and identifying at least three shear zones within the sequence. The uppermost portion of the Kromberg volcanic stratigraphy has undergone significant tectonic deformation and subsequent retrograde fluid alteration (Grosch, 2019; Grosch *et al*., 2020). Additionally, the Kromberg Formation is interpreted to have been tectonically emplaced over polymictic conglomerates of the 3.43 Ga Noisy Formation, based on stratigraphic, metamorphic and structural evidence (Grosch *et al*., 2011, 2012; 2020).

The Mendon Formation forms the uppermost part of the Onverwacht Group and is ~15-20 km thick. It comprises mafic and ultramafic intrusions as well as volcanic komatiites and basaltic pillow lavas interlayered with chert horizons (Byerly, 1999). The Mendon Formation is notable for its transition from predominantly volcanic to more sedimentary sequences, including turbidites, greywackes, and shales. This shift indicates a change from a predominantly volcanic-dominated regime to one influenced by erosion and sedimentation in a more stable, possibly passive margin setting (de Wit *et al*., 2011).

The regional stratigraphy of the BGGT has had contrasting interpretations, with some researchers proposing a continuous stratigraphic sequence of formations (Lowe and Byerly, 1999, 2007), while other researchers argue for litho-tectonic "complexes" in the Onverwacht Group bounded by major shear zones (de Wit *et al*., 1987a,b, 2011).

2.1.2 Surrounding plutons

The Barberton Greenstone-Granitoid Terrain (BGGT) hosts a wide range of tonalite-trondhjemite-granodiorite (TTG) plutons which have distinct ages that range from ca. 3.55 – 3.21 Ga. The different ages reflect multiple phases of magmatic activity and associated unique tectonic processes. These TTG plutons vary in age, fabric, and emplacement history, providing valuable insights into Archean tectonic processes. Below is a detailed overview of the characteristics, fabrics, and U-Pb zircon emplacement ages of key TTG plutons in the Barberton region.

Table 2.1. *A summary of the key features of the BGGT plutons.*

Barberton TTGs	**Characteristics of plutons**	**Fabrics**	**U-Pb emplacement ages**
ca. 3.55-3.50 Ga plutons			
Steynsdorp pluton	Dome-shaped pluton enveloped by Sandspruit and Theespruit Formation supracrustal rocks in the north and east sections (Kroner *et al.*,1996). The Steynsdorp pluton has a tonalitic composition (Moyen *et al*., 2007).	Occur as foliated plutons and banded gneisses. (Moyen *et al.*, 2007). The foliations are attributed to high-grade metamorphism and the deformation to regional tectonism. Some areas of the pluton reveal signs of localized shearing (Kamo and Davis, 1994; Viljoen, 1969; Anhaeusser and Kisters, 1995).	ca. 3509 Ma (Kamo and Davis, 1994; Kroner *et al*., 1991; Schoene *et al*., 2008)

Table 2.1. *(cont).*

ca. 3.45 Ga plutons			
Stolzburg Complex (Stolzburg Pluton, Doornhoek Pluton, Theespruit Pluton)	The Stolzburg and Doornhoek Plutons predominantly consist of tonalite & trondhjemite with high sodium & silica content & low potassium content (de Wit *et al*., 1987). They exhibit typical TTG pluton signatures including high sodium & silica content & low potassium concentrations (Martin, 1986). The Theespruit Pluton is composed of tonalite and granodiorite with minor trondhjemite (Anhaeusser, 1973).	Generally preserve igneous & tectonic fabrics. Alignment of feldspars and mafic minerals (Kamo and Davis, 1994). Pluton displays secondary solid-state deformation fabrics that include weak foliations produced by post-emplacement regional compression (de Wit *et al.*, 1987; Anhaeusser, 1973). Foliations well-preserved in sections that were less affected by tectonics. Shear zones along margins of pluton (de Wit *et al*., 1987).	ca. 3437-3448 Ma (Kamo and Davis, 1994; Armstrong *et al*., 1990; Kroner *et al*., 1991; Muhlberg, 2022)
Eerstehoek, Honingklip, Theeboom etc.		These smaller plutons form complex gneisses.	No data for the Eerstehoek pluton.

Table 2.1*(cont.)*

ca. 3.23-3.21 Ga plutons			
Kaap Valley pluton	Made up of coarse-grained, melanocratic tonalite with amphibole and minor biotite free amphibole-bearing tonalite (Kamo and Davis, 1994).	Exibits prominent foliation with a steep dip and northeast-southwest trend indicative of high-grade metamorphism (Layer *et al*., 1992). A banded structure comprising alternating biotite-rich and quartz-rich layers indicative of metamorphic differentiation (Kamo and Davis, 1994).	ca. 3227 Ma (Kamo and Davis, 1994)
Nelshoogte pluton	Pluton intruded as a laccolith during regional folding. It is made up of coarse-grained leucocratic trondhjemite intruded by amphibole- bearing tonalites (Moyen *et al*., 2007). Pluton characterized by leucocratic and melanocratic banding (Moyen *et al*., 2007).	Displays lit-par-lit intrusive relationships as well as small-scale brecciation with the adjacent greenstone wall rocks (Belcher *et al*., 2005) It has a more heterogenous fabric as foliation intensity and orientation of foliation varying across the pluton (Robb and Anhaeusser., 1983). This irregularity reflects a complex deformation history that likely involves episodes of ductile shearing and folding (Belcher *et al*., 2005).	ca. 3236 Ma (de Ronde and Kamo, 2000; Kamo and Davis, 1994)
Badplaas gneisses	Made up of leucocratic coarse-grained trondhjemite and underwent solid-state deformation (Moyen *et al*., 2007).	Consist of two main suites: (1) an older, coarse-grained leuco-trondhjemitic component that experienced solid-state deformation, and (2) a younger, multiphase	ca. 3290-3230 Ma (Kamo and Davis, 1994; Kisters *et al*., 2010).

Table 2.1 *(cont.)*

		intrusive component composed of typically finer-grained trondhjemites (Kisters *et al.*, 2006). Near the Inyoni shear zone, intrusion is syn-tectonic, indicating that emplacement occurred during active deformation.	
ca. 3.1 Ga Plutons			
Mpuluzi Batholith, Heerenveen Batholith, Salisbury Kop Batholith, Boesmanskop Batholith, Piggs Peak & Nelspruit Batholith.	Comprise sheet-like laccoliths of granitic composition (quartz monzonite, monzonites, granodiorites, and syenites) that extend over a large area.	Characterized by variably deformed pegmatite veins indicating multiple intrusions.	ca. 3.11 Ga (Maphalala & Kröner, 1993; Kamo and Davis, 1994).

2.2 Metamorphic Constraints and Metamorphic History in the BGGT

The BGGT consists of two components, the greenstones in the north of the BGGT and TTGs high-grade terrain in the south of the BGGT which are separated by the highly tectonized Komati fault. It has been suggested that the greenstone sequence of the BGGT has been subjected to low-grade metamorphism which correspond to the greenschist facies with temperatures of 320 °C and pressures of ~3-5 kbar (Cloete, 1999; Tice *et al.*, 2004; Xie *et al.*, 1997). These pressure and temperature conditions are consistent with tectonic burial and thermal relaxation in a stable crustal setting.

In the upper Onverwacht Group greenstone supracrustal sequence, is the presence of an inverted metamorphic gradient observed in the Kromberg type-section (Grosch *et al.*, 2012). This phenomenon, recorded in the ~3.33 Ga Kromberg Formation, is attributed to thrust-related tectonics (Grosch *et al.*, 2012; Grosch, 2019). The Kromberg sequence exhibits retrograde metamorphism with increasing metamorphic grade from bottom to top, opposite to the expected geothermal gradient.

In the higher-grade terrain, slivers of greenstone around granitoid TTG plutons record high-grade regional metamorphic conditions of ~7.4-10 kbar which correspond to the amphibolite facies conditions (Diener and Dziggel, 2021). Modelling of garnet amphibolites has provided peak metamorphic conditions of 8-11 kbar on the margins where the greenstones are in contact with the TTGs (Dziggel *et al*., 2002). Studies by Cutts *et al*. (2021) and Peng *et al*. (2019) have documented peak metamorphic conditions of ~10-12 kbar and 600-650 °C in the Inyoni Shear Zone, consistent with mid- to upper amphibolite facies conditions. These high-pressure, intermediate to high temperature conditions are interpreted to reflect burial and thickening during Paleoarchean subduction-like processes or lateral tectonic accretion (Cutts *et al*., 2021; Kato *et al*., 2021).

The metamorphic evolution of the BGGT is associated with the 3.23 Ga and 3.45 Ga metamorphic episodes (Cutts *et al*., 2023). These ages correlate with two separate periods of crustal shortening. Mineral assemblages and garnet modelling indicate that metamorphism followed a near-isothermal compression P-T path, reaching peak pressures of ~8.5 kbar at 600 °C, followed by decompression and heating to ~640 °C at 6.5 kbar, and subsequent cooling and pressure decrease (Peng *et al*., 2019; Cutts *et al*., 2021).

Similar metamorphic conditions have been documented in other parts of the BGB, with Moyen *et al*. (2006) identifying P-T paths reaching pressures of 12–14 kbar at 600 °C and temperatures of ~700 °C at 9 kbar in shear zones. Additionally, mineral inclusions within the Stolzburg TTG pluton record syn-tectonic metamorphism at pressures of 8–11 kbar and temperatures of 650–700 °C, consistent with regional high-pressure conditions (Dziggel *et al*., 2002). The presence of shear zones and high-strain domains further supports an interpretation of crustal-scale deformation and exhumation most likely around 3.23 Ga (Moyen *et al*., 2006).

These findings align with the interpreted metamorphic history, suggesting a prolonged tectono-thermal evolution before the emplacement of the undeformed Dalmein pluton at 3.216 Ga.

Overall, the metamorphic history of the BGB reflects a complex interplay of subduction-like burial, crustal thickening, and exhumation processes during the early Archean (Cutts *et al*., 2014).

2.3 Structural Geology and Deformation Events in the BGGT

The BGGT has been extensively studied, with various researchers identifying different deformation phases within the BGGT. However, this thesis focuses on the deformation framework proposed by Anhaeusser (2019), Byerly *et al*. (2018) and Dziggel and Kisters (2019), as it represents the most recent interpretation of deformation in the BGGT.

The BGGT was assembled by four significant tectono-magmatic events, each contributing to the BGGTs complex structure observed today. According to Dziggel and Kisters, (2019); Anhaeusser (2019), de Ronde and de Wit, (1994) the first deformation event (D1) occurred between ca. 3.5 Ga and ca. 3.4 Ga and is associated with the deposition of volcanic, volcaniclastic rocks of the Onverwacht Group (e.g. Noisy Formation sediments) coupled with the intrusion of 3.45 Ga suite of TTG plutons, including the Stolzburg pluton. The mafic-ultramafic rocks of the Onverwacht Group are komatiites and komatiitic basalts (Anhaeusser, 2019). The D1 event is preserved in the upper Onverwacht Group formations which are the Komati, Hooggenoeg, and Kromberg Formations (Lowe, 1994, 1999; Lowe and Byerly, 1999; Byerly *et al*., 2018).

The D_2 event is a major deformation event in the BGGT. It corresponds to the tectonic merging of the four fault bounded blocks, with the Inyoni-Inyoka fault system being the main suture zone (Lowe, 1994, 1999; Lowe *et al*., 1999; de Ronde and de Wit, 1994; de Wit *et al*., 2011). The D_2a event occurred from 3.25-3.23 Ga, and it represents the deposition of clastic sediments and felsic volcanic rocks of the Fig Tree Group in deep-water conditions. These clastic sediments developed into the terrane that is to the west of the Inyoni-Inyoka suture zone (Lowe, 1999b; de Ronde and Kamo, 2000; Kisters *et al*., 2006). The ca. 3.23 Ga D_2b event corresponds to crustal collision and the accumulation of sediments that developed into the terranes along the Inyoni-Inyoka suture zone. This was followed by medium-temperature and high-pressure metamorphism of the eastern section of the Stolzburg terrane along the suture zone during transpressional deformation (Moyen *et al*., 2007).

The D_2 event was followed by the short-lived 3.1 Ga D_3 event which corresponds to the deposition of the lower Moodies Group in post-orogenic extensional basins (Byerly *et al.*, 2018). The D_3 event also corresponds to the exhumation of the Stolzburg terrane rocks and TTG emplacement that took place as a result of the collapse of the accreted pile along the Inyoni-Inyoka suture zone (Lowe, 1999). The D3 event is also characterized by refolding and tightening due to the diapiric rise of plutons, such as the Kaap Valley and Stentor plutons along the extensional margins of the BGGT causing NW-SE shortening (Anhaeusser, 2019; Dziggel and Kisters, 2019; Byerly 2018).

The D_4 deformation events followed, and they resulted in the folding and strike-slip faulting of the entire sequence (Belcher and Kisters, 2006a, 2006b). The last orogenic event took place at ca. 3.1 Ga, it led to intraplate compression in parts of the belt (Belcher and Kisters, 2006a, 2006b). Crustal melting occurred as a result of the compression (Belcher and Kisters, 2006a, 2006b). The melts were emplaced as leucogranitic batholiths, some of these batholiths are known as the Nelspruit batholith and the Piggs' Peak batholith (Yearron, 2003).

2.4 The Stolzburg TTG Intrusion

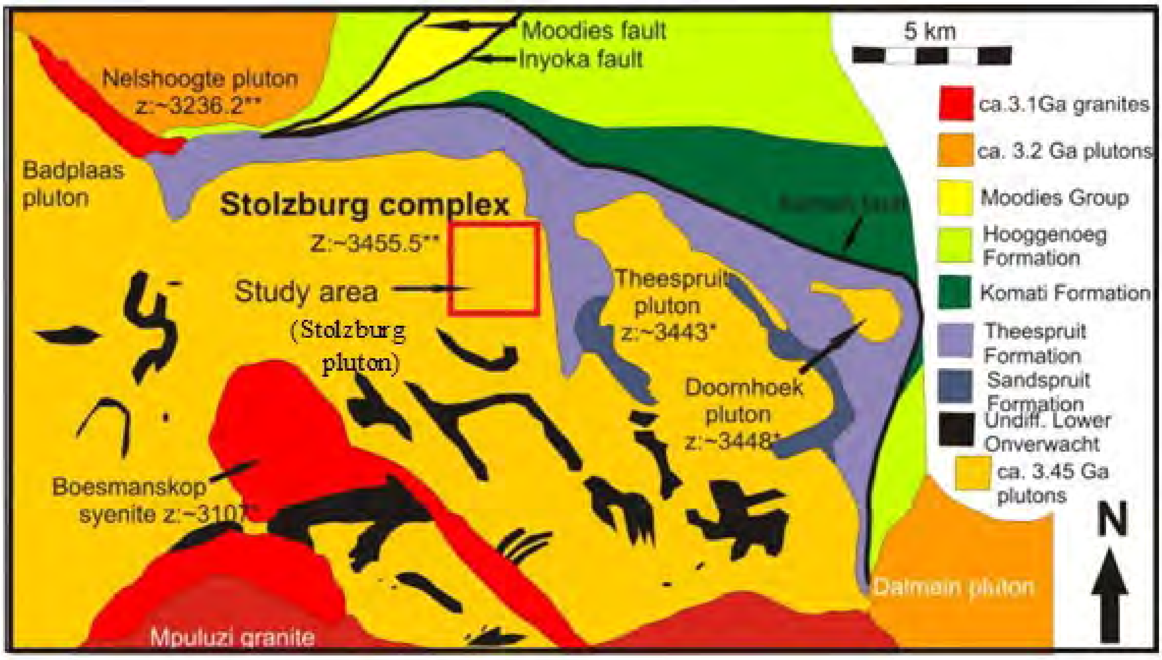

Figure 2.3. *A geologic map showing the Stolzburg Pluton, modified after Schoene et al., (2008). Z= Zircon U-Pb dates of plutons shown in Ma.* One asterisk, Kamo and Davis (1994); two asterisks, Diener *et al.* (2005).

Gold mineralization occurred through hydrothermal processes at ca. 3.1 Ga, the gold is found in association with BIFs, greywackes and shales (Anhaeusser, 2019; Dziggle and Kisters, 2019; Byerly *et al*., 2018).

The Stolzburg TTG pluton is the largest pluton of the Stolzburg Block. The Stolzburg pluton is mainly characterized by leucocratic coarse grained trondhjemite with other minor phases that are texturally different from the main trondhjemite and are darker than the main trondhjemite (Schoene *et al*., 2008; Muhlberg *et al*., 2021). The contacts between the different phases of the trondhjemites are usually sharp (Muhlberg, 2022). The main leucocratic trondhjemite of the Stolzburg has steeply dipping lineations (Muhlberg, 2022). Enclaves of the main leucocratic trondhjemite are found in the other darker phases. Xenoliths of the amphibolites are found in all the trondhjemite phases. The trondhjemite phases together with the amphibolites are crosscut by leucocratic veins (Schoene *et al.*, 2008; Muhlberg, 2022). The outcrop in the Theeboom gneisses is characterized by alternating bands of amphibolites and trondhjemite and has been referred to as the "zebra outcrop" (Muhlberg, 2022).

According to Kamo and Davis (1994); Armstrong *et al*. (1991); Dziggel *et al*. (2002; 2005); Schoene *et al*. (2008); Muhlberg, (2022), the trondhjemite from the Stolzburg Pluton has yielded zircon U-Pb ages of ca. 3437 to 3448 Ma and the trondhjemite from the Theeboom gneiss outcrop yields zircon U-Pb ages of ca. 3460 to 3455 Ma (Kamo and Davis, 1994).

The north-eastern margin of the Stolzburg pluton is made up of undeformed rocks whereas the central Stolzburg pluton is highly deformed. Samples collected from the north-eastern margin and the central Stolzburg pluton yield similar zircon U-Pb ages of around ca. 3455 Ma (Schoene *et al*., 2008). The two localities therefore responded differently to deformation due to a structural discontinuation that separates the NE Stolzburg and the central Stolzburg pluton (Schoene *et al*., 2008).

3 LOCAL GEOLOGY

3.1 Crushers' Quarry

Field work was conducted in a quarry named Crushers' Quarry where fresh TTG and amphibolite outcrops of the Stolzburg TTG Pluton are exposed. The quarry is located on the west of Elukwatini, Mpumalanga. It is situated to the southeast of the R541 Locheil road turn off, near where the road cuts across the Theespruit river. The GPS coordinates of the entrance of the quarry are -26.0236410, 30.7608671. Crushers' quarry has an irregular shape and is approximately 232 m long and 158 m wide.

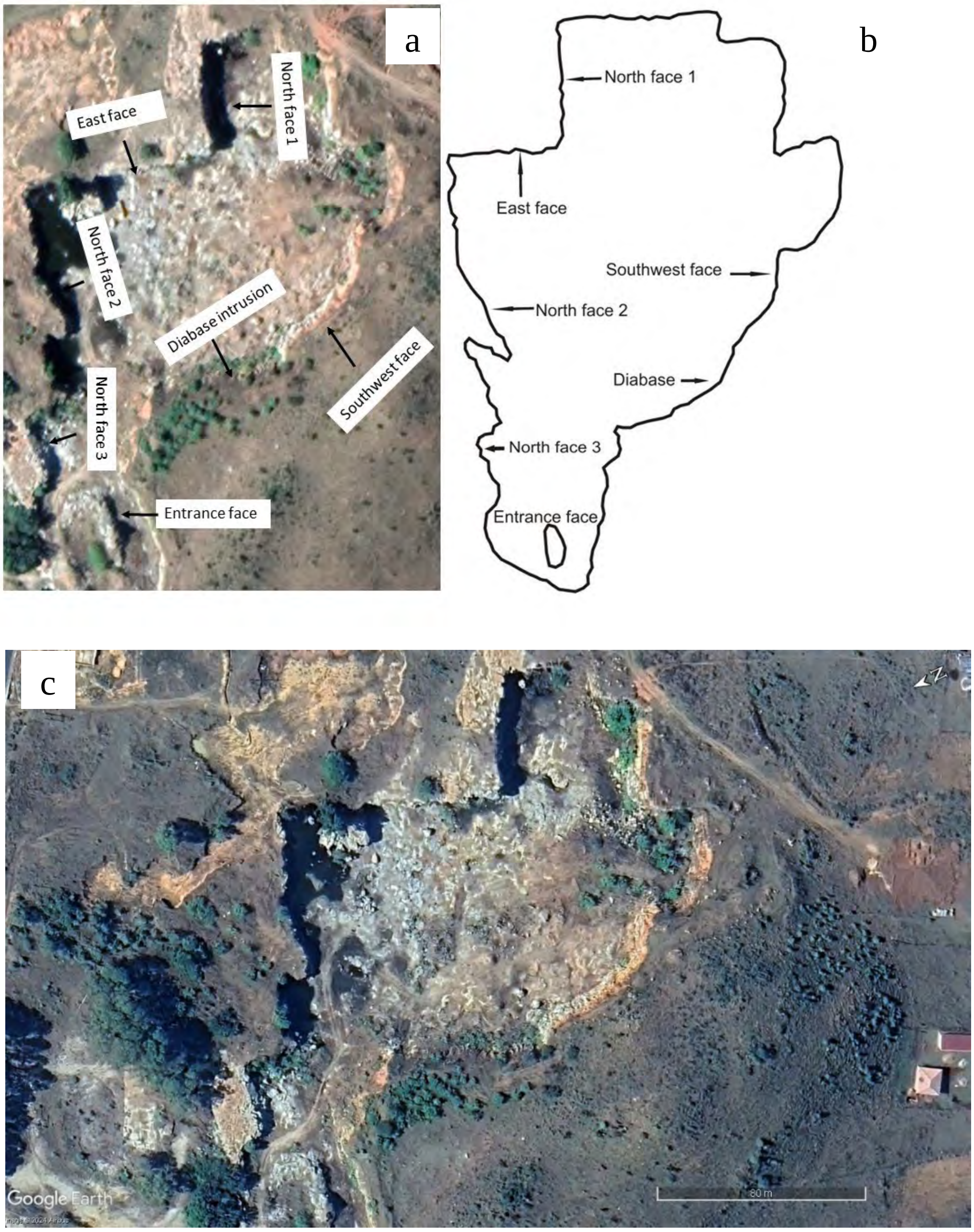

***Figure 3.1**: (a) A satellite image of Crushers' Quarry and (b) drawing showing the outline of the quarry with the location and names of the six faces mapped. (c) Overview of the Crusher's Quarry from Google Earth.*

In this study, the quarry has been investigated across 6 fresh faces: the entrance face, north face 1, north face 2, north face 3, east face and southwest face which were all carefully mapped (Figure 3.1). The rest of the quarry outcrops are heavily weathered therefore they were not mapped.

3.2 Field observations

The coarse-grained trondhjemite illustrated in Figure 3.2a is leucocratic and is made up of translucent quartz grains and whitish plagioclase feldspar minerals. It also consists of some shiny and platy biotite. The biotite in the coarse-grained trondhjemite has a preferred orientation, therefore the coarse-grained trondhjemite is weakly foliated. The medium-grained tonalite (Figure 3.2b) has a sugary texture. It is made up of quartz, plagioclase, and biotite and hornblende. The medium-grained tonalite is mesocratic, grey in colour, because there are a higher proportion of mafic minerals. The fine-grained tonalite (Figure 3.2c) is mostly dark grey in colour. The mineralogy of the fine-grained tonalite is similar to that of the medium-grained tonalite.

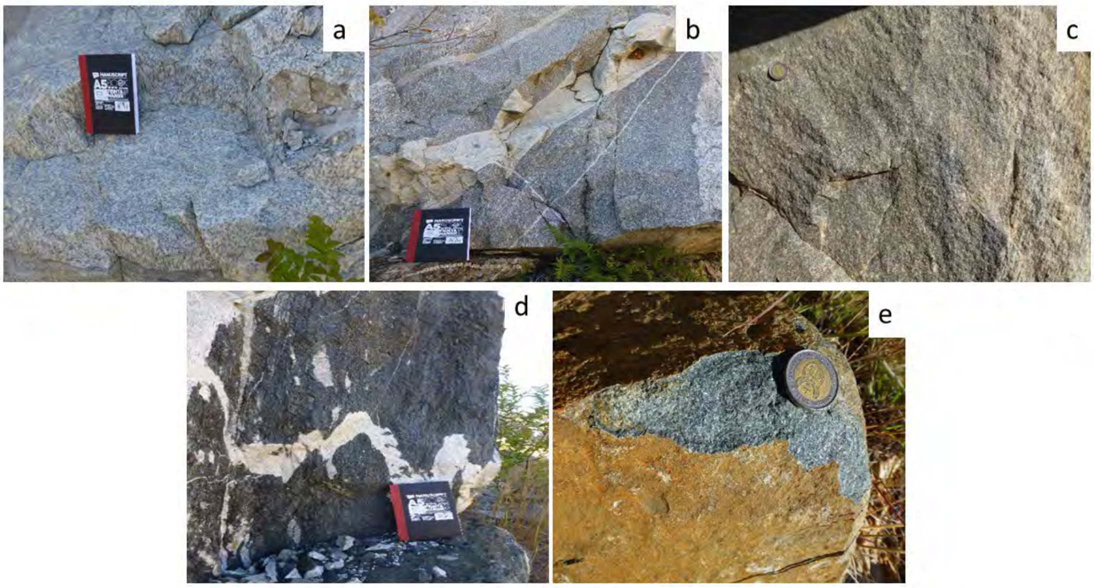

Figure 3.2: *Field photographs showing the different rock types found in Crushers' quarry. (a) Coarse grained trondhjemite, (b) medium grained tonalite with a granodiorite sheet cutting through it, (c) fine grained tonalite, (d) amphibolite with a felsic sheet cutting across, (e) weathered dolerite (A5 notebook and R5 coin for scale).*

The amphibolite (Figure 3.2d) is medium grained and is greenish black in colour. The visible minerals are green amphibole minerals which are likely to be hornblende and platy biotite. The amphibolites are highly foliated. The amphibolites appear as xenoliths and dismembered sheets/slivers in the TTG intrusion. The protolith to the amphibolite was likely the country rock into which the TTG intruded. A local diabase intrusion has a brownish colour because of weathering, and there are a few fresh areas which are exposed. It is melanocratic and is made up of plagioclase, pyroxene and needle like minerals that resemble actinolite (Figure 3.2e). This diabase intrusion is likely related to the 2.7 Ga Badplaas Dyke Swarm (Mare and Fourie, 2012) and is unrelated to the Stolzburg TTG intrusion.

3.3 Key field relationships

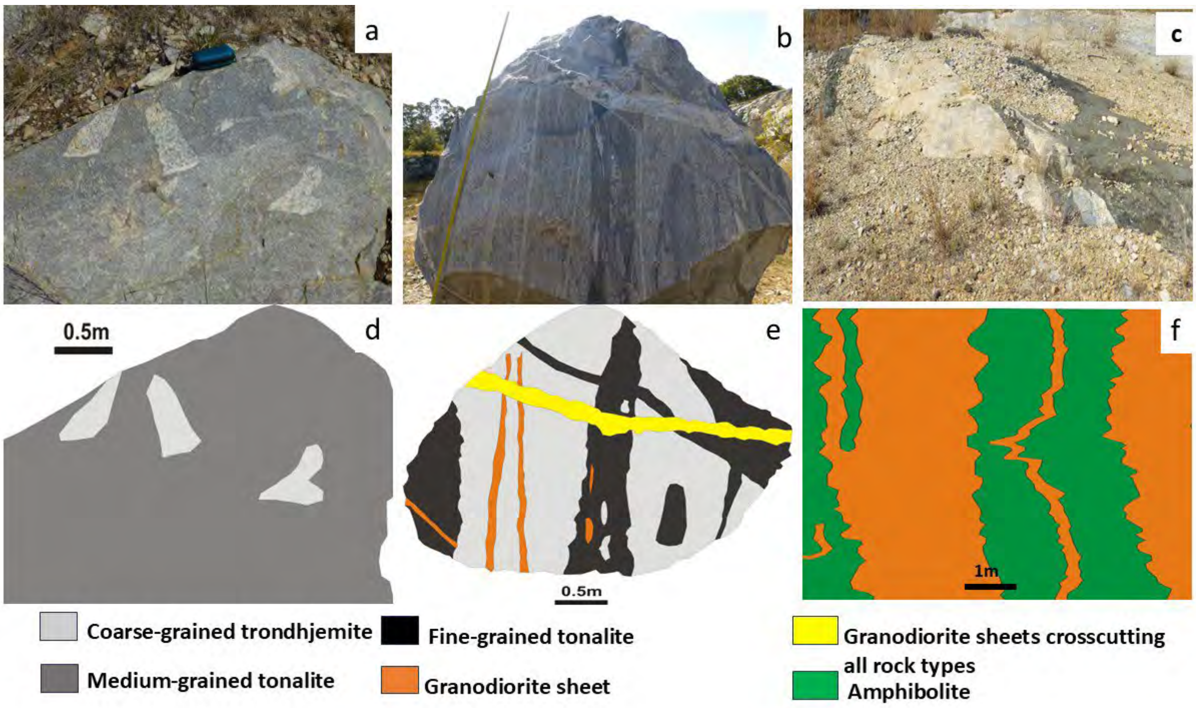

Figure 3.3: *Field photographs of TTG relationships in the top row and digitized drawings of the outcrops in the lower row. (a and d) Coarse-grained trondhjemite enclaves contained in medium-grained tonalite, (b and e) an outcrop with crosscutting relationships between fine-grained tonalite, coarse-grained trondhjemites, felsic veins and granodiorite sheets, (c and f) trondhjemite and amphibolite slivers.*

Figure 3.3a and 3.3d illustrate coarse-grained trondhjemite enclaves entrained by medium-grained tonalite during intrusion, thus indicating that the medium-grained tonalite intruded into the coarse-grained trondhjemite, making the coarse-grained trondhjemite the earliest magmatic phase.

The outcrop on Figure 3.3b and 3.3e illustrates a felsic vein running through the fine-grained tonalite (shown in orange) on the left and some felsic material in the fine-grained tonalite in the middle of the outcrop. There are two felsic veins running parallel to one another within the coarse-grained trondhjemite. The felsic veins in the fine-grained tonalite are second generation whereas the felsic veins in the coarse-grained trondhjemite are first generation. The granodiorite sheet crosscuts everything; therefore it is the latest phase.

Figure 3.3c and 3.3f illustrate slivers that mark the contact between country rocks and trondhjemites. As the trondhjemitic magma intruded, it exploited and interacted with the foliations in the amphibolites thus forming the alternating bands. The grain size of the trondhjemite is unclear due to weathering.

3.4 Mapping of Crushers' Quarry

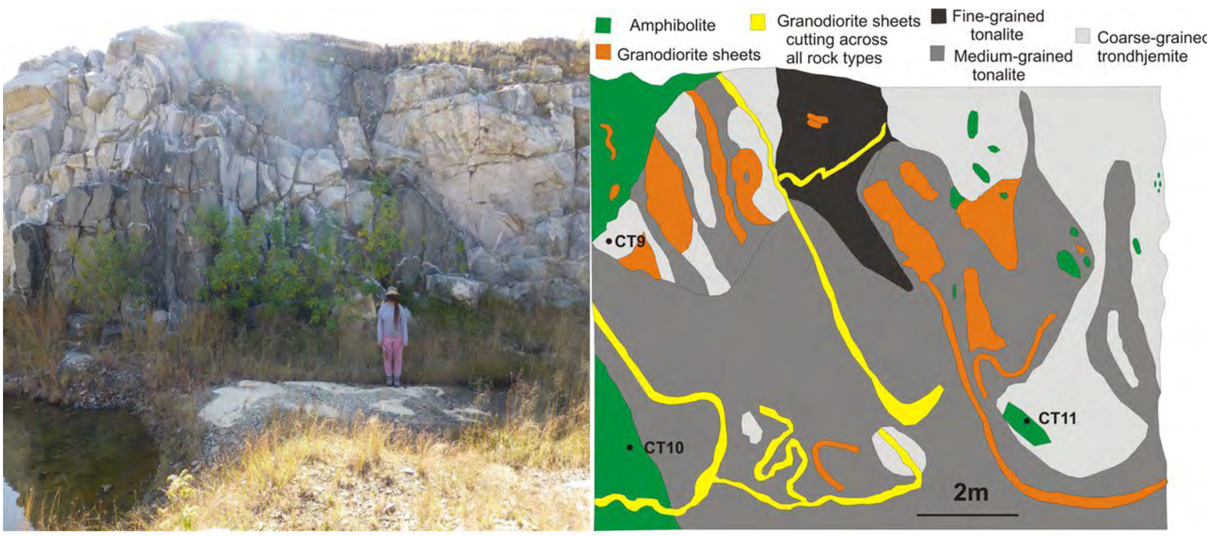

Figure 3.4: *A photograph of north face 1 and corresponding lithological map. The rock types identified, and colour schemes are shown in the legend.*

North face 1 shown in Figure 3.4 comprises mostly of medium-grained tonalite (dark grey on legend) that contains large amphibolite xenoliths (shown in green), which were entrapped during the ascent of the medium-grained tonalite (Figure 3.4). Coarse-grained trondhjemite (shown in light grey) is contained within the medium-grained tonalite. Fine-grained tonalite cuts across both coarse-grained trondhjemite and medium-grained tonalite. This suggests that the coarse-grained trondhjemite is the oldest TTG, followed by the intrusion of the medium-grained tonalite, which was then intruded by the fine-grained tonalite.

The coarse-grained trondhjemite is associated with felsic veins and bodies, which implies that the coarse-grained trondhjemite intruded together with the felsic material. There are also felsic veins found within medium-grained tonalite. The felsic veins in the coarse-grained trondhjemite are first generation felsic veins, whereas those in the medium-grained tonalites are second generation felsic veins. Granodiorite sheets cut across all rock types therefore they are the latest intrusive phase.

Small amphibolite xenoliths also occur in the coarse-grained trondhjemite as in the medium-grained tonalite. The amphibolite xenoliths could be of different mafic protolith generations, or from the same parent country rock but were entrapped into the coarse-grained trondhjemites and medium-grained tonalites at different times.

Figure 3.5: *A photograph of the east face and corresponding lithological map. The location of sample CT12 is shown.*

The eastern side of the east face (Figure 3.5) is made up of an amphibolite sliver (shown in green) which connects to the amphibolite xenolith on north face 1. The majority of the east face outcrop is medium-grained tonalite and fine-grained tonalite. The medium-grained tonalite is contained within fine-grained tonalite. There are some coarse-grained trondhjemite and amphibolite xenoliths within the fine-grained tonalite. Medium-grained tonalite also contains coarse-grained trondhjemite and amphibolite xenoliths. Felsic veins and pockets are contained in the fine-grained tonalite and coarse-grained trondhjemite suggesting different felsic vein generations. Granodiorite sheets (shown in yellow) cut across all rock types. Felsic veins in the coarse-grained trondhjemites are first generation, whereas the felsic veins in the fine-grained tonalite are third generation.

The amphibolite xenoliths were possibly derived from the same protolith country rock but were incorporated in the TTGs (coarse- and fine-grained) at different times.

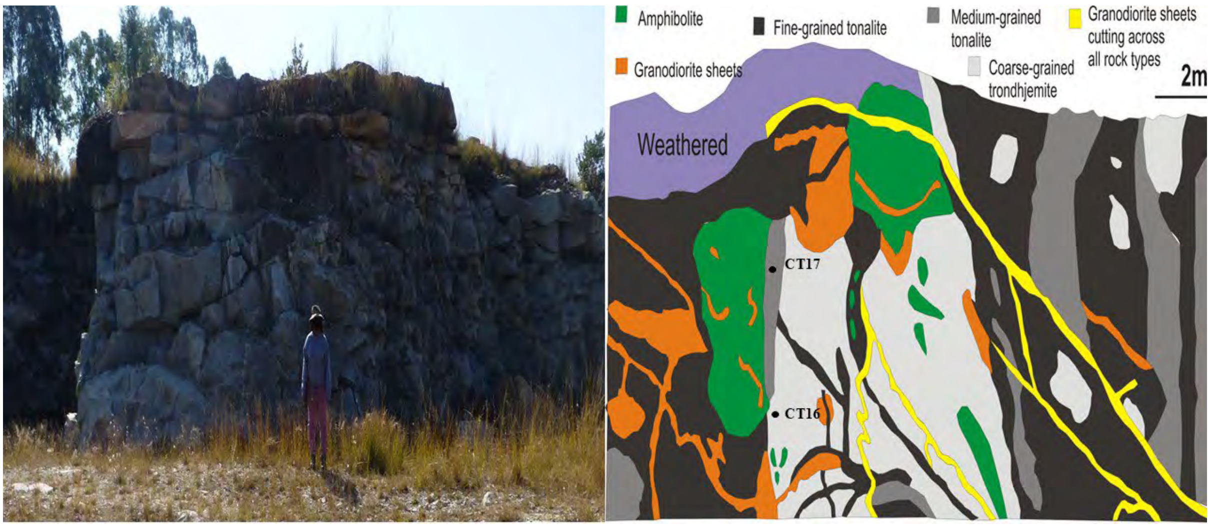

***Figure 3.6**: A photograph of north face 2 and corresponding map showing the relationships between the different rock types. The location of sample CT16 and CT17 is shown.*

On the east side of north face 2 shown in Figure 3.6, there are alternating bands of medium- and fine-grained tonalites. The fine-grained tonalite contains medium-grained tonalite and coarse-grained trondhjemite fragments. The coarse-grained trondhjemite in the middle of the outcrop contains several felsic veins, granodiorite sheets and fine-grained tonalite veins. There are smaller amphibolite xenoliths in the coarse-grained trondhjemite and fine-grained veins. On the west side of the face there is fine-grained tonalite containing medium-grained tonalite as is the east side, an amphibolite xenolith as well as felsic veins.

North face 2 (Figure 3.6) indicates that the earliest TTG phases are the medium-grained tonalites and coarse-grained trondhjemites because they are contained in the fine-grained tonalite. There are no visible crosscutting relationships between the medium-grained tonalite and coarse-grained trondhjemites on this face to help in determining which phase intruded earlier than the other. However, from earlier mentioned outcrops, it is clear that the coarse-grained trondhjemites occur within medium-grained tonalite magmatic phases.

There are granodiorite sheets that cut through the fine and medium-grained tonalites as well as the coarse-grained trondhjemites. These granodiorite sheets represent the latest phase. The large amphibolite xenoliths have some felsic veins within them.

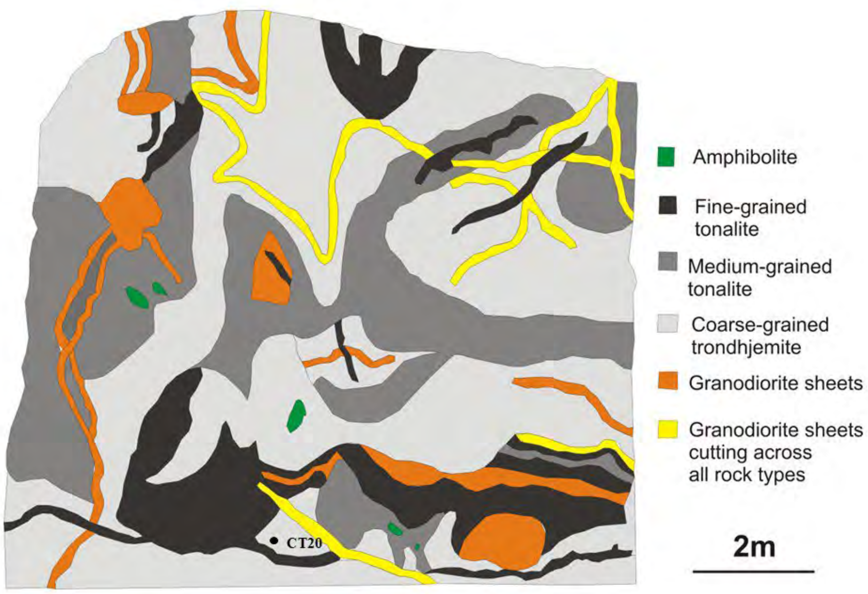

***Figure 3.7**: A digitized drawing of north face 3 with the location of sample CT20 shown.*

The rocks on north face 3 (Figure 3.7) are fractured, making interpretation difficult. There are amphibolite xenoliths (shown in green) contained in the medium-grained tonalite and coarse-grained trondhjemites. As in the faces described previously, there are felsic veins in the coarse-grained trondhjemite which were already contained within the coarse-grained trondhjemite when it intruded. There are granodiorite sheets (shown in yellow) that cut across everything which are the latest intrusion.

There are some fine-grained tonalite veins cutting across coarse-grained trondhjemite and medium-grained tonalite, suggesting the fine-grained tonalite is the last intrusive phase. There are fine-grained tonalite veins that also cut across the late granodiorite sheets therefore suggesting that there could be a second phase of fine-grained tonalite, but this relationship has not been observed on the other faces that are not fractured so this relationship could be attributed to the fracturing on north face 3.

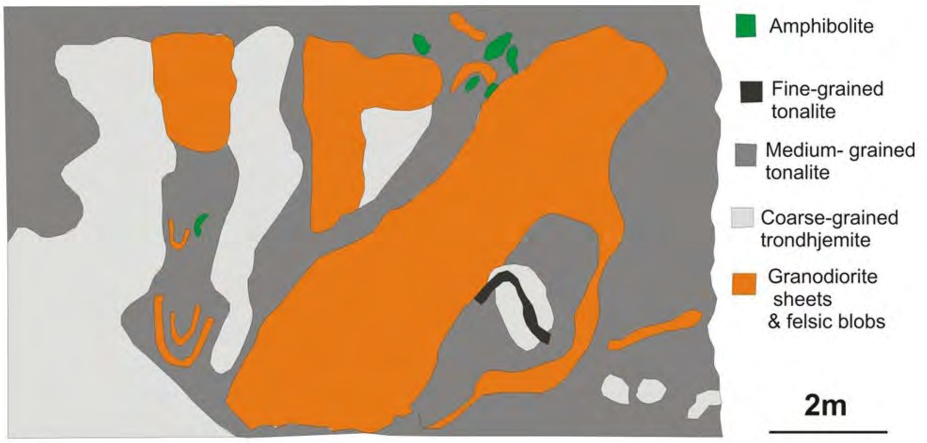

Figure 3.8*: A digitized drawing of the entrance face.*

The entrance face is on the floor near the entrance of the quarry (Figure 3.8). It is comprised of medium-grained tonalite which envelopes coarse-grained trondhjemite, suggesting that the coarse-grained trondhjemite intruded earlier than the medium-grained tonalite. There are felsic veins and bodies entrapped within the medium-grained tonalite. There are amphibolite xenoliths in the medium-grained tonalite. On the east side of the entrance face is a fine-grained tonalite vein cutting through coarse-grained trondhjemite and some of the medium-grained tonalite, therefore the fine-grained tonalite intruded last.

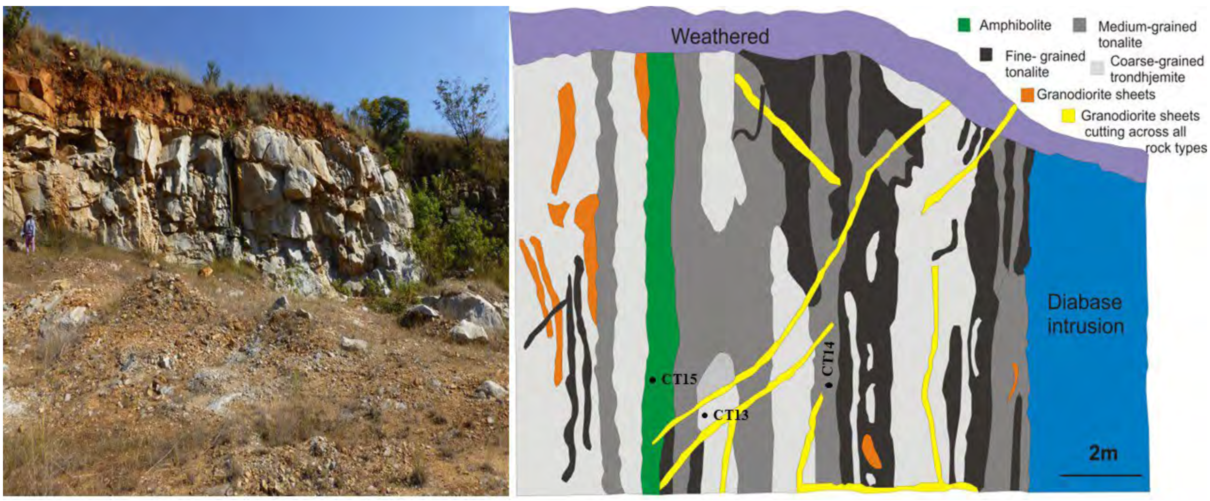

Figure 3.9*: A photograph of the southwest face and corresponding lithological drawing. Note the diabase intrusion in the back right, on the western side.*

The southwest face is made up of fine-grained tonalite, medium-grained tonalite, coarse-grained trondhjemite and amphibolite slivers of various widths (Figure 3.9). The coarse-grained trondhjemite (shown in light grey) on the west side of the face contains felsic veins (shown in orange) that do not cut across the other rock types therefore implying that the felsic veins were already incorporated in the coarse-grained trondhjemite when it intruded. There are also fine-grained tonalite veins (shown in darkest grey) that cut through some of the felsic veins within the coarse-grained trondhjemite.

In the middle of the outcrop is fine-grained tonalite which contains medium-grained tonalite and coarse-grained trondhjemites. There are granodiorite sheets (shown in yellow) cutting through all the TTG phases suggesting that they were emplaced after all other rock types.

Towards the east of the southwest face is fine-grained tonalites with some coarse-grained trondhjemite and a small felsic body. This implies that the coarse-grained trondhjemite intruded earlier than the fine-grained tonalite. Moving further to the east of the face there is medium-grained tonalite containing fine-grained tonalite and a felsic body.

In summary, the amphibolite xenoliths in the TTGs are pieces of the country rock which were broken up when the TTGs intruded. They form xenoliths and slivers that run sub-parallel to each other in the coarse-grained trondhjemites, medium-grained tonalites and fine-grained tonalites. The coarse-grained trondhjemite (T1) is the earliest occurring magmatic phase on most of the faces in the quarry. The medium-grained tonalite (T2) intrudes after the coarse-grained trondhjemite. Fine-grained tonalite (T3) intruded later than both the medium-grained tonalite and coarse-grained trondhjemite.

There appears to be multiple generations of felsic veins. First generation felsic veins are contained in the coarse-grained trondhjemites. Medium-grained tonalites contain second generation felsic veins. The third generation of felsic veins is in the fine-grained tonalite. Fourth generation felsic veins are in the amphibolites. Granodiorite sheets that are coarse-grained cut across all the rock types as the last phase.

4 PETROGRAPHY

4.1 Samples

A total of 22 rock samples were collected at Crusher's Quarry. Of these samples, 5 are amphibolites, 6 are coarse-grained trondhjemite, 6 are medium-grained tonalite, 2 are fine-grained tonalite and 3 are granodiorite sheet samples. This chapter will report and compare the petrographic characteristics of these rock types.

4.1.1 Amphibolites

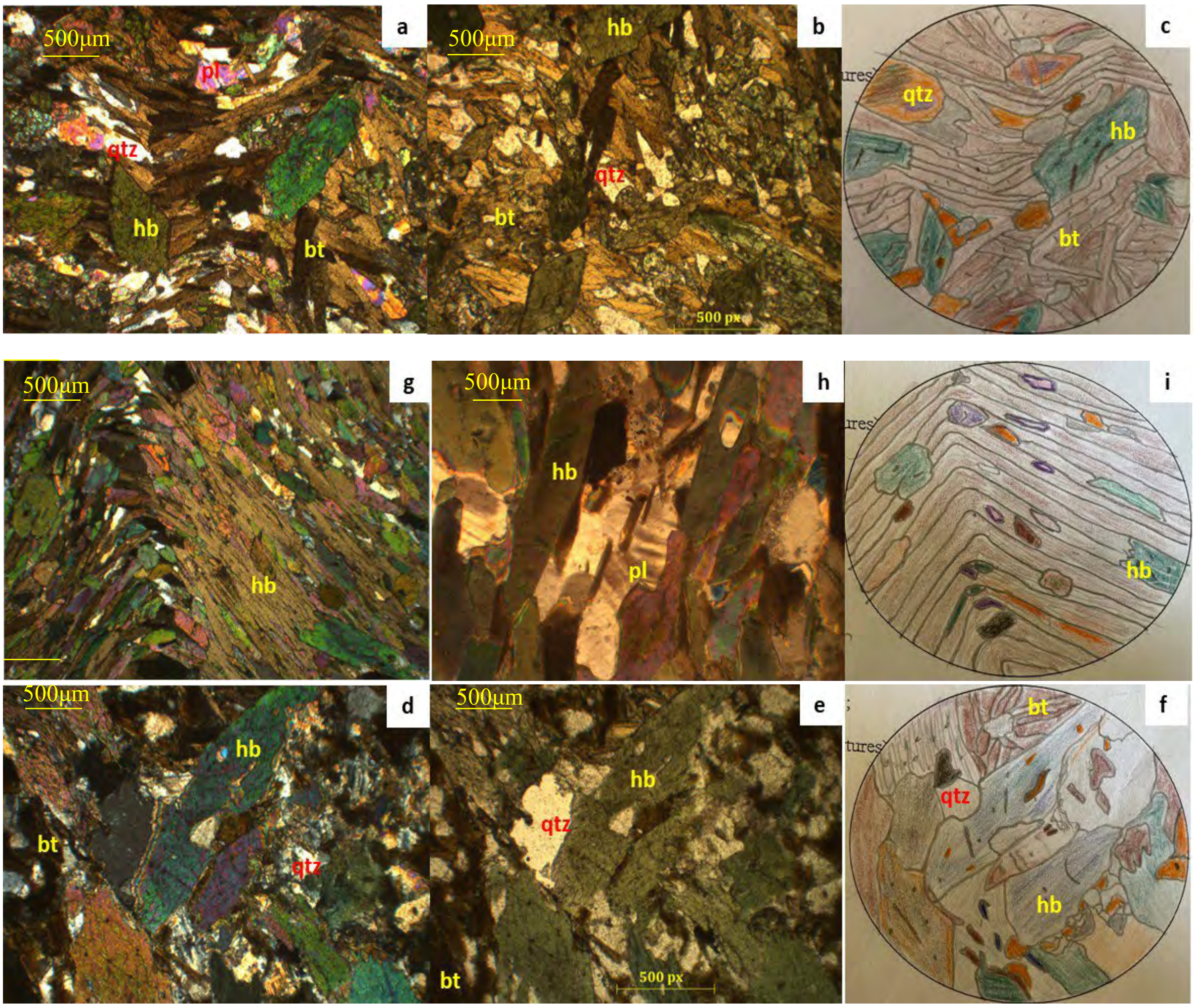

Figure 4.1: *Petrographic features of amphibolite xenoliths. (a, b) photomicrograph of samples CT4 under cross- and plane-polarized light. (c) sketch of sample CT4 under crossed polars. (d, e) photomicrograph of samples CT10 under cross- and plane-polarized light. (f) sketch of sample CT10 under crossed polars. (g, h) photomicrograph of samples CT11 under cross- and plane-polarized light. (i) sketch of sample CT11 under crossed polars. All photomicrographs at 2.5X magnification except for (h) which is at 20X magnification. Abbreviations: pl: plagioclase, bt: biotite, hb: hornblende qtz: quartz.*

Sample CT4 is composed of ~60 % hornblende, ~25 % biotite, ~10 % plagioclase and ~5 % quartz. The hornblende grains are second order green. Hornblende has strong green pleochroism under plane polarized and the grains have moderately high relief. Hornblende crystals have a prismatic habit and idiomorphic. They present symmetrical extinction. Biotite grains are second order brown. They are tabular and hypidiomorphic. The grains have a preferred orientation. In plane polarized light, biotite grains present strong brown pleochroism and they have moderate to high relief. The biotite exhibits bird's eye extinction. Sample CT4 has a lepidoblastic texture.

Sample CT10 was collected at the contact of the amphibolite and trondhjemite. The sample is made up of ~50 % hornblende, ~30 % biotite, ~10 % plagioclase and ~10 % quartz. The minerals occur randomly with no preferred orientation. The grain size in this sample is variable as the hornblende grains are coarse grained whereas the quartz and plagioclase grains are fine grained. Plagioclase grains show minor seritization on Figure 4.6h.

The hornblende grains in sample CT11 have a preferred orientation and the sample has crenulation cleavages. The modal proportions for sample CT11 are ~80 % hornblende, ~10 % biotite, ~5 % plagioclase and ~5 % quartz. The hornblende and biotite grains are prismatic. Quartz and plagioclase are allotriomorphic and they exist as interstitial minerals because they do not show any clear crystal faces. Quartz and plagioclase grains are visible at high magnification, in between the crenulation cleavages of the biotite and hornblende grains. Plagioclase grains are first order grey and present polysynthetic twining whereas the quartz grains are first order grey. Hornblende has quartz inclusions, and the hornblende grains are hypidiomorphic.

Hornblende grains are generally coarse grained in the amphibolite samples. Biotite is medium grained and quartz and plagioclase are fine grained.

Figure 4.2. *Photographs showing the crenulation cleavages of amphibolite samples.*

The hornblende and biotite crystals have preferred orientation giving the rocks a foliated texture. The foliations have kink bands and crenulation cleavages.

4.1.2 Coarse-grained trondjhemite

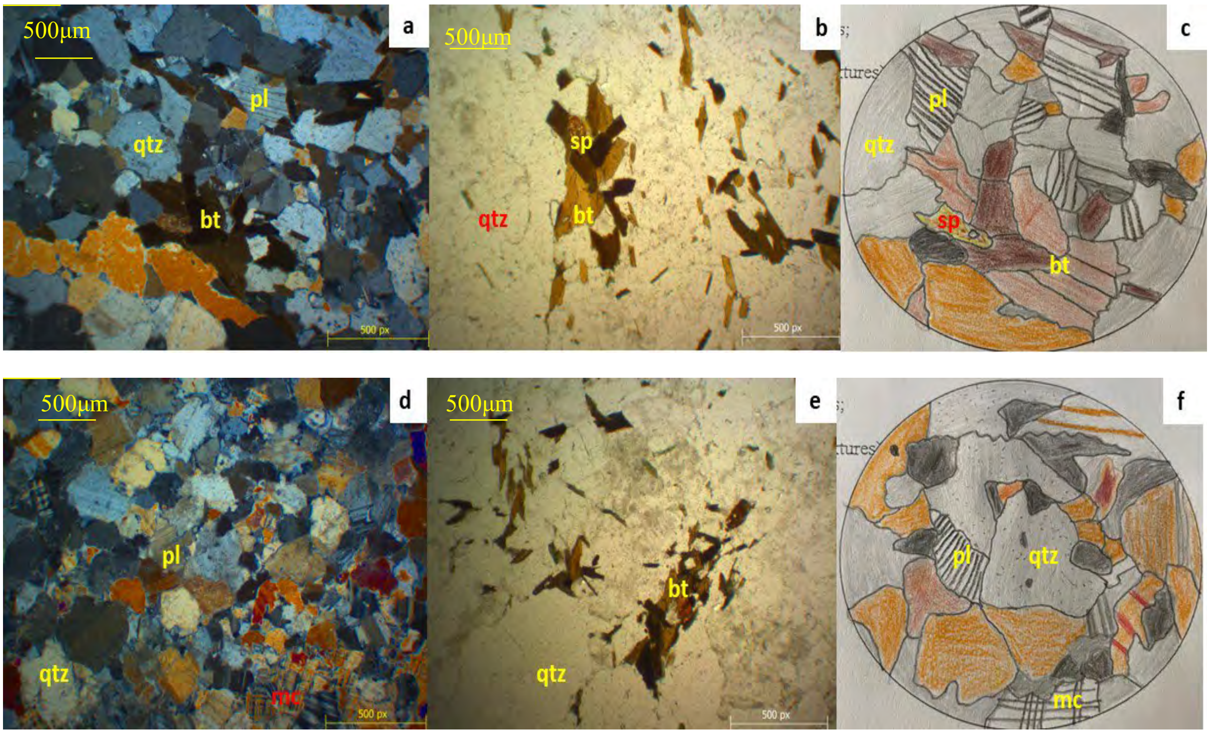

Figure 4.3: *Petrographic features of coarse-grained trondhjemite. (a, b) photomicrograph of sample CT16 under cross- and plane-polarized light. (c) sketch of sample CT16 under crossed polars. (d, e) photomicrograph of sample CT20 under cross- and plane-polarized light. (f) sketch of sample CT20 under crossed polars. Abbreviations: pl: plagioclase, sp: sphene, bt: biotite, qtz: quartz, mc: microcline. All photomicrographs at 2.5X magnification.*

The coarse-grained samples are mineralogically different from the fine- and medium-grained tonalite samples because they do not have amphibole (hornblende). CT16 is made up of ~80 % quartz, ~8 % plagioclase and ~10 % biotite. Sample CT20 is made up of ~60 % quartz, ~8 % microcline, ~8 % plagioclase and ~8 % biotite. The biotite crystals in the TTG samples have preferred orientation that creates weak foliations in the rocks. Quartz and plagioclase are coarse grained than the rest of the minerals. Biotite and microcline are medium grained.

Figure 4.4. *Photographs of thin sections showing foliations in the coarse-grained trondhjemite samples.*

4.1.3 Medium-grained tonalite

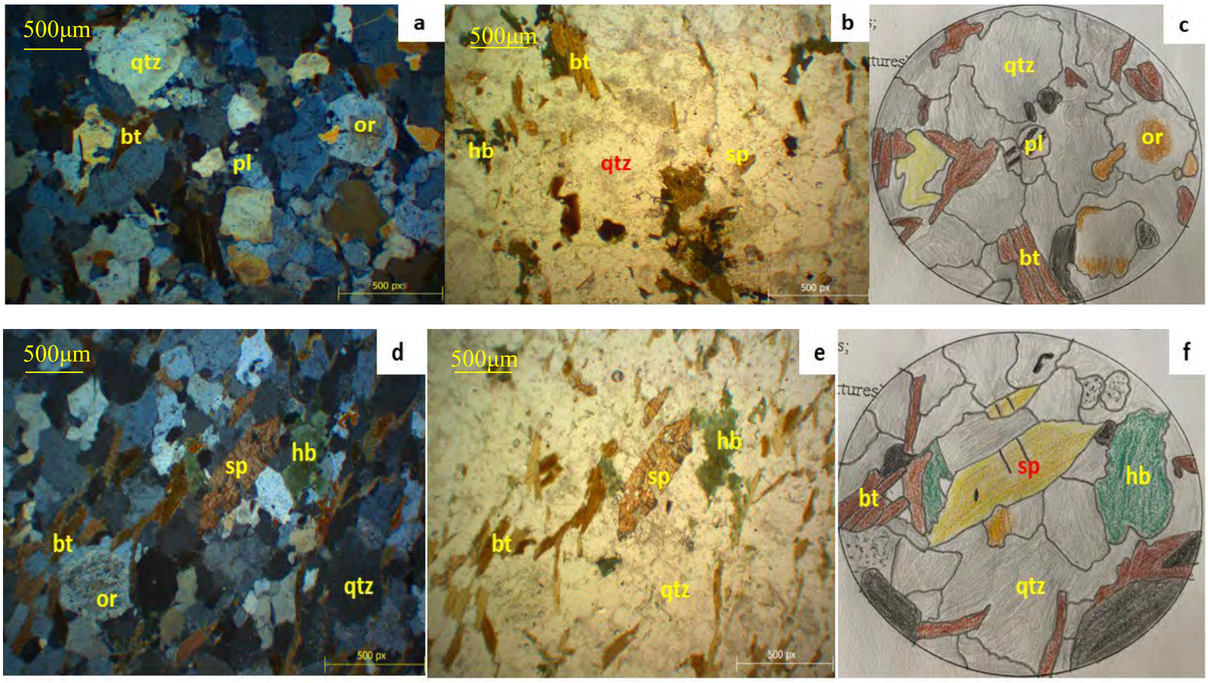

Figure 4.5: *Petrographic features of medium-grained tonalites. (a, b) photomicrograph of sample CT12 under cross- and plane-polarized light.(c) sketch of sample CT12 under crossed polars. (d, e) photomicrograph of sample CT14 under cross- and plane-polarized light. (f) sketch of sample CT14*

under crossed polars. Abbreviations: or: orthoclase, pl: plagioclase, sp: sphene, bt: biotite, qtz: quartz, hb: hornblende. All photomicrographs at 2.5X magnification.

The mineralogy of sample CT12 is ~70 % quartz, ~5 % orthoclase, ~5 % plagioclase, ~10 % biotite, ~5 % hornblende and minor sphene. The quartz grains have first order birefringence as they display greyish and orange interference colours. Orthoclase has low relief and first order birefringence. The orthoclase grains are non-pleochroic. Contrary to the observations made in the fine-grained samples, there is less plagioclase and little to no microcline in sample CT12.

Biotite is found in clusters. The biotite grains are brown under cross-polarized light and pale brown under plane-polarized light. Some of the biotite grains are partly chloritized. There is a higher proportion of hornblende in sample CT12, the grains are also larger in size than in the fine-grained samples. The hornblende grains have cleavages at 120° and display a dark green colour. Under plane-polarized light hornblende has strong green pleochroism. There is a higher proportion of sphene grains which are also larger in size than the grains observed in the fine-grained rocks. The sphene grains usually occur where the ferromagnesian minerals are clustered.

Quartz, orthoclase and spinel are coarser while plagioclase is medium grained in these samples.

4.1.4 Fine-grained tonalite

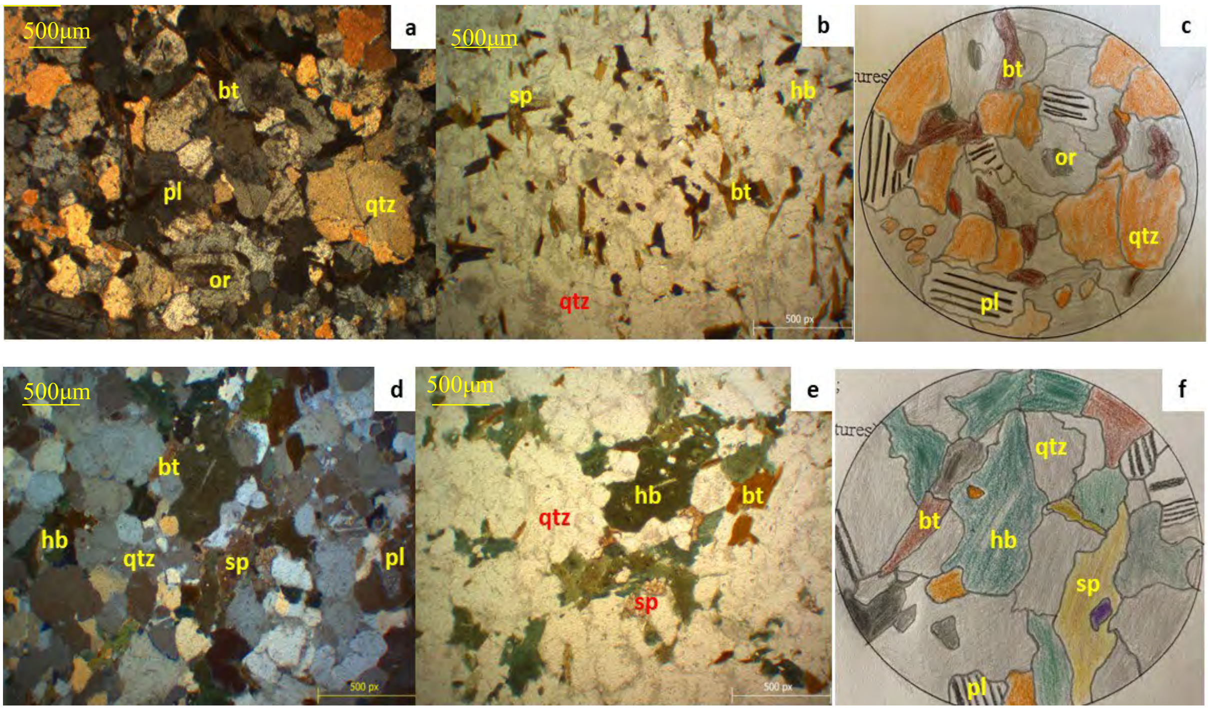

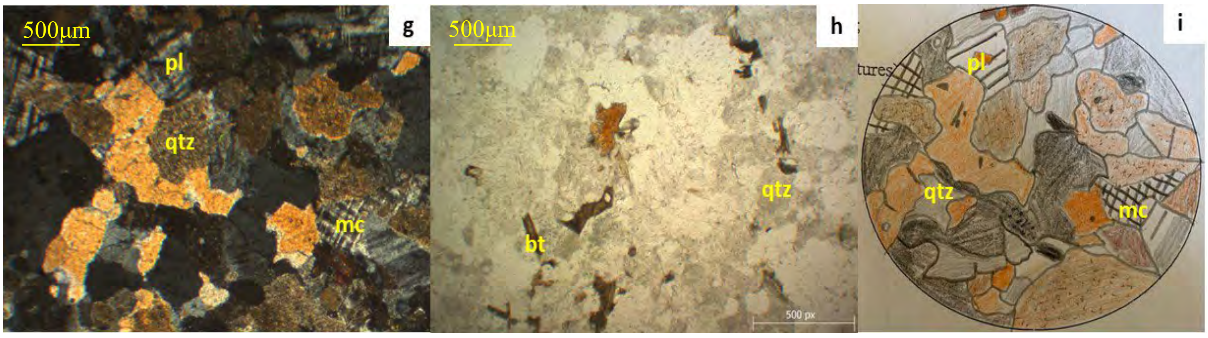

Figure 4.6: *Petrographic features of fine-grained tonalite. (a, b) photomicrograph of sample CT1 under cross- and plane-polarized light. (c) sketch of sample CT1 under crossed polars. (d, e) photomicrograph of sample CT5 under cross- and plane-polarized light. (f) sketch of sample CT5 under crossed polars. (g, h) photomicrograph of sample CT8 under cross- and plane-polarized light. (i) sketch of sample CT8 under crossed polars. Abbreviations: or: orthoclase, pl: plagioclase, sp: sphene, bt: biotite, qtz: quartz, hb:hornblende. All photomicrographs at 2.5X magnification.*

Sample CT1 is made up of ~65 % quartz, ~15 % plagioclase, ~10 % biotite, ~3 % orthoclase, minor hornblende and accessory sphene. The sample is holocrystalline as it is composed entirely of crystals. The plagioclase grains are subhedral. They have a greyish black interference colour and first order birefringence. The plagioclase shows no pleochroism under plane polarized light and has low to moderate relief. Plagioclase exhibits polysynthetic twining, and the grains have inclined extinction.

Orthoclase appears to be partly altered in the centre because the orthoclase grains have brown patches in the centre. The orthoclase grains are subhedral. They are colourless under plane polarized light therefore they do not show any pleochroism. Under cross polarized light the orthoclase grains are first order grey.

Quartz grains are first order yellow under cross polarized light but colourless under plane polarized light. The quartz shows no pleochroism and has low relief. The quartz grains exhibit undulose extinction and are subhedral. Biotite grains are euhedral and prismatic. The biotite is third order brown. The grains exhibit strong brown pleochroism under plane polarized light and have moderate relief. Biotite grains exhibit bird's eye extinction. Hornblende is present in minor amounts. The hornblende grains have strong green pleochroism in plane-polarized light and they exhibit a dark green interference colour with second order birefringence. Sphene is brownish under cross polarized light. The grains have high relief in plane polarized light but do not show any pleochroism.

Sample CT8 has ~70 % quartz, ~15 % microcline, ~10 % plagioclase and ~5 % biotite. The quartz grains interference colours range from grey to orange. The plagioclase grains are non-pleochroic under plane-polarized light; under cross-polarized light the plagioclase grains exhibit polysynthetic twinning.

4.1.5 Granodiorite sheets

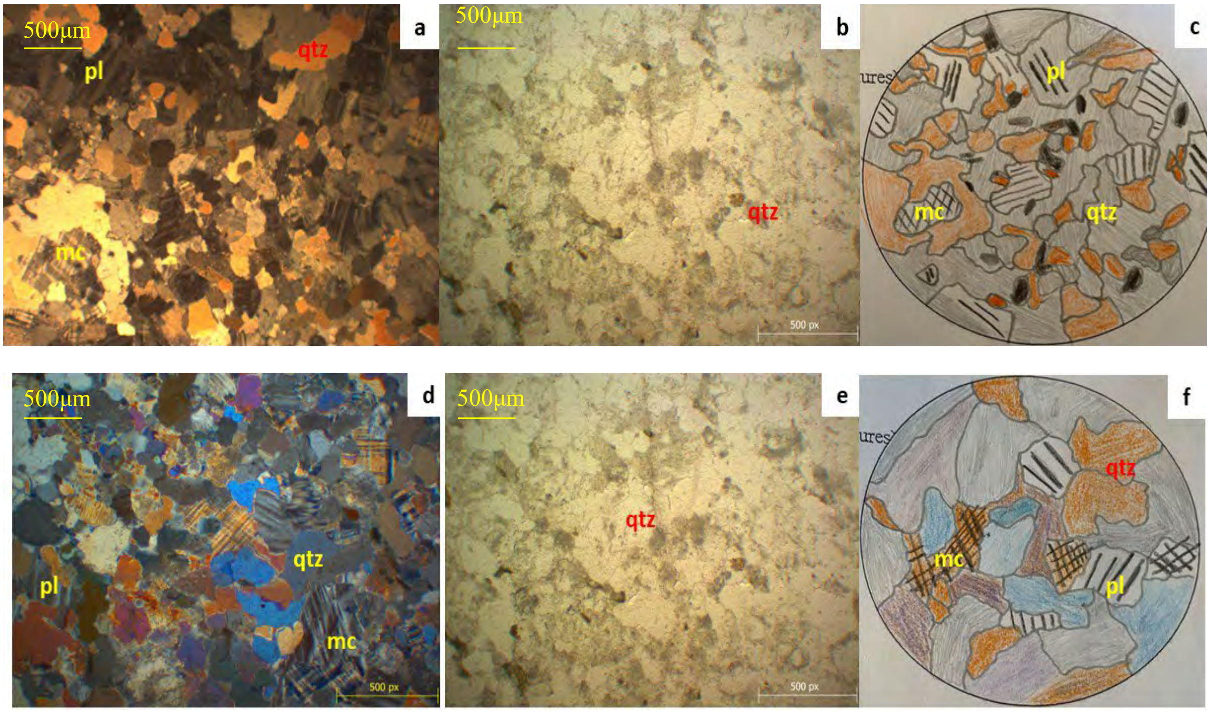

Figure 4.7: *Petrographic feature of granodiorite sheets (a, b) photomicrograph of samples CT2 under cross- and plane-polarized light. (c) sketch of sample CT2. (d, e) photomicrograph of samples CT3 under cross- and plane-polarized light. (f) sketch of sample CT3. Abbreviations: pl: plagioclase, mc: microcline, qtz: quartz. All photomicrographs at 2.5X magnification.*

The granodiorite sheet samples are holocrystalline. The samples are composed of ~60 % quartz, ~10 % microcline and ~30 % plagioclase. Some quartz grains are first order grey, and some are first order yellow. The difference in interference colours is influenced by the orientation of the grains when they were cut. When quartz grains are cut perpendicular to the c-axis they appear to be yellow under plane polarized light but when cut parallel to the c-axis they present grey interference colours. The quartz grains are anhedral and there is variability in the size of the grains. The grains are colourless under plane polarized light therefore they are not pleochroic. Quartz grains do not have any cleavages or twins, but they display undulose extinction.

Microcline is identified by cross hatched twinning. Microcline grains are first order grey and colourless under plane polarized light, therefore they do not exhibit any pleochroism. Microcline grains are subhedral and have inclined extinction. The plagioclase grains exhibit polysynthetic twinning under crossed polars.

Sample CT3 is made up of ~50 % quartz, ~40 % plagioclase, and ~10 % microcline with high order birefringence colours. The minerals display the same optic properties and in sample CT2. All minerals seem to be medium grained except for quartz which is more coarse-grained.

Table 4.1. *Summary of petrographic characteristics of Stolzburg Pluton rock samples.*

Rock type	Minerals present	Modal abundance (%)	Textures	Degree of alteration
Fine-grained tonalites	Quartz, Plagioclase, Orthoclase, Biotite, Hornblende, Sphene	Qtz (65), Pl (15), Or (3), Bt (10), Hb (5), Sp (1)	Hypidiomorphic, interlocking, no foliations	Low alteration: Orthoclase sericitized in the centre.
Medium-grained tonalites	Quartz, Plagioclase, Orthoclase, Biotite, Hornblende, Sphene	Qtz (70), Pl (5), Or (5), Bt (10), Hb (5), Sp (5).	Weak foliation	Low alteration: Orthoclase grains are sericitized. Some biotite grains partly chloritized.
Coarse-grained trondhjemites	Quartz, Plagioclase, Microcline, Biotite, Sphene	Qtz (73), Pl (8), Mc (8), Bt (8), Sp (2).	Hypidiomorphic, interlocking, slightly foliated	Low to no alteration: no sericitization in feldspars
Granodiorite sheets	Quartz, Plagioclase, Microcline	Qtz (60), Pl (10), Mc (30)	No foliation	Low alteration
Amphibolites	Quartz, Plagioclase, Biotite, Hornblende	Qtz (5), Pl (10), Bt (24), Hb (62)	Lepidoblastic	Moderate alteration: seriticized plagioclase grains

Mineral abbreviations: Qtz = Quartz, Pl = Plagioclase, Or = Orthoclase, Mc = Microcline, Bt = Biotite, Hb = Hornblende, Sp = Spinel.

5 GEOCHEMISTRY

5.1 Samples

This chapter presents the bulk geochemistry of the 22 TTG rock samples of the Stolzburg pluton. Field and petrographic observations indicate that there are a range of rock types: fine-grained to medium-grained tonalites, coarse-grained trondhjemites, granodiorite sheets and amphibolite xenoliths. The major and trace element data from the felsic rocks are reported in **Table 5.1** and the amphibolites in **Table 5.2** with corresponding sample numbers.

5.2 Analytical Methods

Major and trace element whole-rock data were collected by Mrs Riana Rossouw and Mrs Mareli Grobbelaar at the Central Analytical Facility, University of Stellenbosch.

- **X-ray Fluorescence (XRF)**

Samples were crushed into a fine powder (particle size < 70 µm) with a jaw crusher and milled in a tungsten-carbide Zibb mill prior to the preparation of a fused disc for major and trace elements analysis. The jaw crusher and mill are cleaned with clean uncontaminated quartz between each sample to avoid cross contamination. Glass disks were prepared for XRF analysis using 7 g of high purity trace element and Rare Earth Element-free flux ($LiBO_2$ = 32.83 %, $Li_2B_4O_7$ = 66.67 %, LiI = 0.50 %) mixed with 0.7 g of the powder sample. Whole-rock major element compositions were determined by XRF spectrometry on a PANalytical Axios Wavelength Dispersive spectrometer at the Central Analytical Facilities, Stellenbosch University, South Africa. The spectrometer is fitted with an Rh tube and with the following analyzing crystals: LIF200, LIF220, PE 002, Ge 111 and PX1. The instrument is fitted with a gas-flow proportional counter and a scintillation detector. The gas-flow proportional counter uses a 90 % Argon-10 % methane mixture of gas. Major elements were analyzed on a fused glass disk using a 2.4 kW Rhodium tube. Matrix effects in the samples were corrected for by applying theoretical alpha factors and measured line overlap factors to the raw intensities measured with the SuperQ PANalytical software. The concentration of the control standards that were used in the calibration procedures for major element analyses fit the range of concentration of the samples. Amongst these standards were NIM-G (Granite from the Council for Mineral Technology, South Africa) and BE-N (Basalt from the International Working Group).

Regarding precision and accuracy of the XRF whole-rock sample data, all major element oxide compositions for all analytical standards (BE-N, JB-1, BHVO-1, HUSG-1) are provided in Appendix D

Table 5.1: *Major element (wt.%) and trace element (ppm) data of TTGs from Crusher's Quarry, Barberton. Abbreviations: bdl = below detection limit, L.O.I= loss on ignition.*

Lithology	Coarse-grained trondhjemites						Medium-grained tonalites						Fine-grained tonalites		Granodiorite sheets		
Sample name	CT6	CT9	CT13	CT16	CT20	CT21	CT7	CT12	CT14	CT17	CT22	CT23	CT1	CT5	CT2	CT3	CT8
SiO_2	72,78	72,43	71,13	73,17	72,72	74,01	64,22	64,15	60,10	69,63	68,41	68,16	64,51	64,07	76,40	77,21	76,41
TiO_2	0,18	0,15	0,25	0,22	0,22	0,15	0,63	0,57	1,06	0,36	0,39	0,40	0,56	0,62	0,05	0,05	0,06
Al_2O_3	15,66	15,41	15,87	15,08	15,14	14,80	17,81	17,38	17,26	16,24	16,89	16,87	17,25	17,83	13,06	13,17	13,30
Fe_2O_3	1,29	1,29	1,93	1,57	1,68	1,31	3,41	4,67	5,05	2,63	3,03	3,02	3,92	3,56	0,71	0,64	0,64
FeO^T	1,16	1,16	1,74	1,41	1,51	1,18	3,07	4,20	4,54	2,37	2,73	2,72	3,53	3,20	0,64	0,57	0,57
MnO	0,03	0,02	0,05	0,02	0,03	0,02	0,06	0,06	0,09	0,05	0,05	0,05	0,05	0,05	0,01	0,01	0,01
MgO	0,34	0,31	0,38	0,30	0,33	0,25	1,25	0,91	2,60	0,45	0,56	0,54	0,80	1,75	bdl	Bdl	bdl
CaO	1,98	1,67	1,97	1,89	1,81	1,59	3,83	4,07	4,83	2,51	3,06	3,05	3,68	4,22	1,29	0,81	1,10
Na_2O	6,21	5,01	5,92	5,44	5,75	5,30	5,93	5,69	5,62	5,71	5,50	5,55	5,66	6,27	3,66	3,37	3,73
K_2O	1,40	3,34	2,06	2,12	1,85	2,49	1,71	1,97	1,91	1,96	1,95	1,95	1,82	1,42	3,74	5,28	4,41
P_2O_5	0,04	0,04	0,05	0,04	0,04	0,03	0,20	0,32	0,32	0,13	0,18	0,17	0,24	0,18	0,00	0,00	0,00
Cr_2O_3	Bdl	Bdl	Bdl	Bdl	Bdl	bdl	Bdl	Bdl	Bdl	bdl	bdl	bdl	bdl	Bdl	bdl	Bdl	bdl
L.O.I.	0,97	0,35	0,54	0,22	0,44	0,17	0,93	0,77	0,79	0,57	0,26	0,66	1,49	0,66	1,09	0,45	0,55
Sum Of Conc.	**100,86**	**100,02**	**101,88**	**101,49**	**101,52**	**100,12**	**99,99**	**104,76**	**104,17**	**102,61**	**100,28**	**100,41**	**99,99**	**100,63**	**100,00**	**100,99**	**100,20**
Sc	4,95	4,39	9,40	8,18	8,48	4,74	7,60	9,62	14,16	11,02	5,73	5,55	5,77	8,00	4,49	4,47	4,79

Table 5.1 *(cont).*

V	15,46	14,47	14,25	11,93	13,00	13,03	46,96	45,21	91,01	23,82	28,63	29,93	36,09	61,98	11,21	9,96	10,54
Cr	12,58	70,48	17,37	16,50	18,73	10,62	78,71	10,20	50,89	16,34	11,64	14,09	11,52	25,86	13,55	15,74	20,43
Co	2,83	2,93	4,01	3,10	3,13	2,57	9,22	8,65	19,40	4,36	5,12	4,96	6,70	11,34	1,21	1,08	1,02
Ni	8,17	8,88	9,63	8,40	9,53	6,25	11,04	6,73	25,71	7,80	6,92	7,10	22,15	15,92	10,18	11,19	4,27
Cu	45,13	31,05	6,64	5,56	7,41	7,66	23,61	47,28	9,26	10,20	20,18	35,05	1117,98	17,37	377,54	549,71	3,92
Zn	40,93	40,90	76,81	48,50	53,59	45,13	116,85	183,93	110,88	91,53	87,53	91,60	146,74	79,05	30,46	26,82	23,20
Rb	28,85	75,83	67,59	42,24	45,14	49,21	76,87	71,00	72,22	52,34	56,07	55,93	55,82	49,12	60,18	94,00	104,09
Sr	389,62	545,80	532,22	518,46	471,23	373,02	823,26	915,43	902,61	703,61	764,76	766,32	906,71	845,46	521,62	326,14	219,34
Y	4,06	2,21	5,21	2,04	2,94	3,03	9,34	9,82	14,99	5,85	7,44	7,10	6,82	7,16	0,90	1,23	8,64
Zr	71,94	62,62	94,60	78,30	85,29	71,53	201,93	204,94	212,16	146,63	184,31	189,42	241,62	113,94	60,02	51,18	50,53
Nb	4,86	2,78	8,80	2,34	4,33	3,84	9,48	11,05	11,60	9,59	12,16	12,30	13,03	6,87	1,16	2,52	6,80
Mo	0,67	0,93	0,89	0,78	0,81	0,80	1,24	0,84	1,00	0,93	0,79	0,99	0,89	1,05	1,33	1,11	0,96
Cs	1,68	5,23	2,30	1,86	2,23	1,53	9,64	6,76	5,07	2,67	2,78	2,82	4,12	9,04	1,01	1,48	2,45
Ba	337,89	909,73	411,77	595,64	369,20	564,91	390,35	972,76	409,93	823,39	1016,77	1041,83	1028,73	399,44	1841,91	1177,25	460,44
La	9,03	8,28	16,01	12,77	11,25	10,67	18,08	46,08	16,47	27,77	38,37	39,12	52,20	16,92	8,23	5,52	6,98
Ce	20,15	17,62	32,60	23,92	23,28	22,50	36,81	95,44	43,40	53,70	75,81	76,75	102,35	34,86	17,61	10,93	15,41
Pr	2,24	1,92	3,28	2,55	2,39	2,52	4,40	11,44	5,99	6,19	8,99	8,73	12,19	4,25	1,72	1,04	1,74
Nd	9,93	7,06	12,22	8,71	8,26	8,21	18,01	45,85	26,30	23,35	34,45	33,15	44,58	18,58	6,08	3,09	6,02
Sm	2,36	1,48	2,18	1,20	1,30	1,57	3,29	8,49	5,90	4,00	5,42	5,83	8,07	3,60	0,95	0,47	1,71
Eu	0,58	0,42	0,52	0,35	0,39	0,39	1,09	2,24	1,59	0,99	1,35	1,42	2,11	1,22	0,28	0,14	0,41

Table 5.1 *(cont)*.

Gd	1,49	0,83	1,39	0,87	0,78	1,07	2,94	5,53	4,95	2,61	3,68	3,50	4,82	3,00	0,55	0,35	1,60
Tb	0,23	0,12	0,19	0,09	0,11	0,12	0,37	0,60	0,59	0,26	0,41	0,37	0,50	0,33	0,07	0,04	0,30
Dy	1,00	0,61	0,99	0,45	0,63	0,75	1,72	2,60	2,88	1,30	1,91	1,73	1,80	1,60	0,25	0,25	1,39
Ho	0,17	0,09	0,19	0,08	0,11	0,10	0,32	0,36	0,51	0,23	0,28	0,26	0,22	0,26	0,05	0,05	0,28
Er	0,43	0,19	0,54	0,17	0,32	0,28	0,82	0,63	1,20	0,48	0,56	0,63	0,43	0,66	0,27	0,12	0,91
Tm	0,04	0,03	0,07	0,04	0,04	0,05	0,10	0,08	0,19	0,08	0,09	0,07	0,09	0,08	0,05	0,03	0,14
Yb	0,31	0,20	0,51	0,18	0,31	0,25	0,70	0,40	1,18	0,50	0,44	0,39	0,34	0,44	0,16	0,15	0,97
Lu	0,04	0,03	0,08	0,03	0,04	0,03	0,13	0,06	0,16	0,05	0,08	0,06	0,06	0,09	0,04	0,03	0,15
Hf	1,91	1,87	2,97	2,41	2,59	2,15	4,62	5,66	5,13	4,15	4,80	4,60	5,75	3,14	2,84	2,42	2,20
Ta	0,43	0,20	0,58	0,20	0,33	0,33	0,61	0,72	1,02	0,72	0,90	0,81	0,71	0,56	0,07	0,18	0,70
Pb	10,32	18,40	12,52	10,08	11,19	16,05	11,68	15,93	9,70	12,57	15,35	15,72	14,51	10,56	15,49	19,02	22,26
Th	1,73	1,69	3,65	1,75	3,74	2,81	3,48	7,52	3,94	6,80	6,43	6,47	8,73	2,96	5,55	5,01	5,53
U	0,93	0,77	1,56	0,59	1,02	0,97	2,35	2,56	3,78	1,60	1,67	1,66	2,08	1,61	1,56	2,03	4,50

FeO^T was calculated using the formula:

$FeO^T = Fe_2O_3 \times 0.8998$

- **ICP-MS Laser Ablation**

A Resolution 193nm Excimer laser from ASI connected to an Agilent 7700 ICP-MS is used in the analysis of trace elements in bulk rock samples as well as on single mineral grains. Ablation is performed in He gas at a flow rate of 0.35L/min, then mixed with argon (0.9L/min) and Nitrogen (0.004L/min) just before introduction into the ICP plasma. For traces in fusions, 2 spots of 100µm is ablated on each sample using a frequency of 10Hz and fluence of ~5J/cm^2. Fusion disks prepared for XRF analysis by an automatic Claisse M4 Gas Fusion instrument and ultrapure Claisse Flux, using a ratio of 1:10 sample:flux, were coarsely crushed and a chip of sample mounted along with up to 12 other samples in a 2.4cm round resin disk. The mount was mapped, and then polished for analysis. Trace elements are quantified using NIST 612 for calibration and the % SiO_2 from XRF measurement as internal standard, using standard – sample bracketing. Two replicate measurements are made on each sample. The calibration standard was run every 12 samples. A quality control standard is run in the beginning of the sequence as well as with the calibration standards throughout. BCR-2 or BHVO 2G, both basaltic glass certified reference standards produced by USGS (Dr Steve Wilson, Denver, CO 80225), is used for this purpose. A fusion control standard from certified basaltic reference material (BCR-2, also from USGS) is also analysed in the beginning of a sequence to verify the effective ablation of fused material. Data processing was done using the LA-ICP-MS data reduction software package Iolite v.3.2 (Paton *et al*., 2011).

Regarding precision and accuracy of the trace element whole-rock sample data, selected trace element compositions for all analytical standards (i.e BCR-2G glass, BHVO-2G glass, BHVO powder, BCR powder) are provided in appendix C.

5.3 Geochemical characterization and classification of TTGs

The major element Harker diagrams in Figure 5.1 below are plotted to assess geochemical trends. The major elements are plotted against SiO_2. The fine to medium-grained tonalites (CT1, CT5, CT7, CT12, CT14, CT17, CT22, and CT23) SiO_2 contents ranging from 64.07 wt.% to around 68.0 wt.%. The coarse-grained trondhjemite samples (CT6, CT9, CT13, CT16, CT20 and CT21) have SiO_2 contents around 72 wt.%. The granodiorite sheets CT2, CT3 and CT8 have the highest SiO_2 contents of around 77 wt.%. The fine to medium-grained tonalites seem to form two groups due to overlapping SiO_2 contents of these two groups.

The fine to medium-grained tonalites have K_2O contents ranging from 1.4-2.1 wt.%. The K_2O content of the coarse-grained trondhjemite samples ranges from 1.4-3.5 wt.%. There is not a large difference in the Na_2O content across all the rock types. The tonalites have Na_2O contents between 5.4 and 6.3 wt.%. The TiO_2-SiO_2 Harker plot shows the fine to medium-grained tonalite samples to have TiO_2 contents between 0.4 and 1.3 wt.%. The TiO_2 content of the coarse-grained trondhjemite samples falls between 0.1-0.3 wt.%.

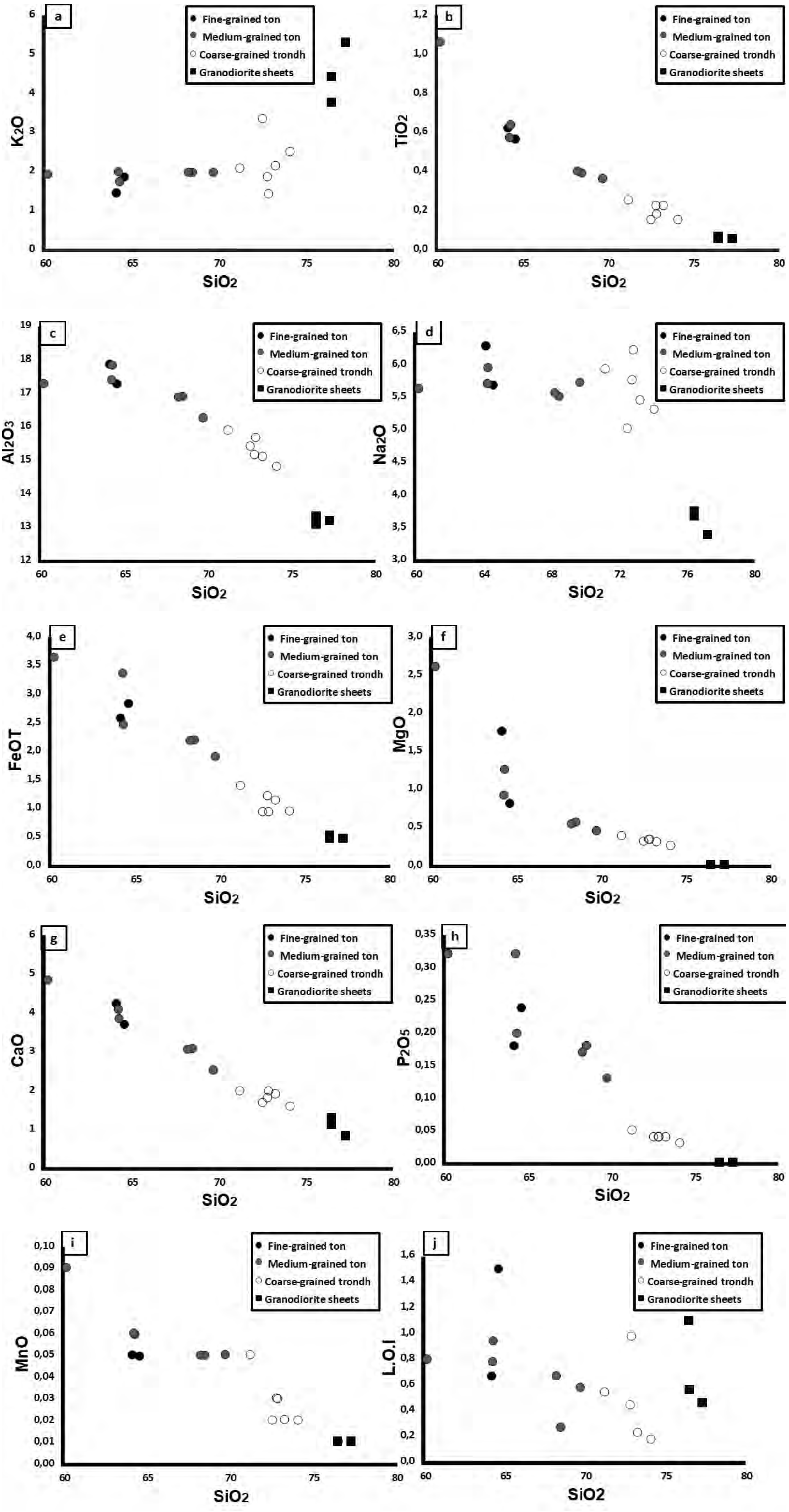
a
K2O
SiO2
Fine-grained ton
Medium-grained ton
Coarse-grained trondh
Granodiorite sheets
b
TiO2
SiO2
c
Al2O3
SiO2
d
Na2O
SiO2
e
FeOT
SiO2
f
MgO
SiO2
g
CaO
SiO2
h
P2O5
SiO2
i
MnO
SiO2
j
L.O.I
SiO2

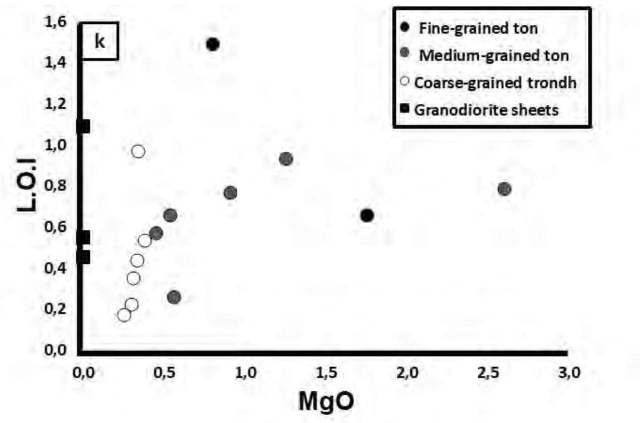

***Figure 5.1**: Major element Harker plots for the Stolzburg pluton TTGs using SiO_2 as the index of differentiation. Major elements are recorded in weight percentage (wt. %).*

The Al_2O_3-SiO_2 plot shows the tonalites to have Al_2O_3 contents between 16 and 18 wt.%. The coarse-grained trondhjemites have Al_2O_3 compositions between 14.5-16 wt.%. The tonalites show FeO^T contents between 1.7 and 3.6 wt.%. The coarse-grained trondhjemites show FeO^T contents between 0.7 and 1.5 wt.%. The MgO-SiO_2 plot on figure 5.1 (f) shows that tonalites have MgO contents from 0.5-2.6 wt.%. The coarse-grained trondhjemitic rocks have MgO contents between 0.2 and 0.4 wt.%. The CaO-SiO_2 Harker plot (Figure 5.1g) shows that the tonalites have CaO contents between 2.5 and 4.9 wt.%. The coarse-grained trondhjemites have CaO compositions between 1.5 and 2 wt.%. On the P_2O_5-SiO_2 plot the tonalites have a P_2O_5 composition ranging between 0.13 and 0.3 wt.%. The coarse-grained trondhjemites have P_2O_5 contents ranging between 0.03 and 0.49 wt.%. The MnO-SiO2 plot (Figure 5.1i) shows fine- to medium-grained tonalites with SiO2 values ranging from 60-70 wt.% and MnO values ranging from 0.4-0.9 wt.%. Coarse-grained tonalites have MnO contents ranging from 0.2-0.5 wt.%. Granodiorite sheets have a MnO content of 0.01 wt.%.

The L.O.I-SiO_2 plot (Figure 5.1j) shows fine- and medium-grained tonalites plotting between 60-70 wt.% SiO_2 contents and 0.2-1.5 wt.% L.O.I contents. The coarse-grained trondhjemites have SiO_2 contents between 70-75 wt.% and their L.O.I content ranges between 0.2-1 wt.%. Granodiorite sheets plot between SiO2 contents of 75-78 wt.% and L.O.I contents of 0.4-1.2 wt.%. Figure 5.1k plots L.O.I against MgO where the MgO content of the granodiorite sheets is below detection and their L.O.I ranges from 0.4-1.1 wt.%. Coarse-grained trondhjemites display MgO between 0-0.5 wt.% and a L.O.I range of 0.1 to 1 wt.%. Fine- and medium-grained tonalites display MgO contents ranging between 0.5-2.6 wt.% and a L.O.I range of 0.2-1.5 wt.%.

Based on the Harker plots on Figure 5.1 a-k above, the following groups and trends are observed. Medium-grained tonalites overlap with fine-grained tonalites but extend to slightly higher SiO_2 (65-70 wt.%) values. Coarse-grained trondhjemites plot at higher SiO_2 values (70-75 wt.%). TiO_2, Al_2O_3, FeO^T, MgO, CaO and P_2O_5 all exhibit negative correlations with SiO_2, as they decrease from fine- and medium-grained tonalites to granodiorite sheets. Na_2O shows a scattered distribution but generally displays a slight decrease from fine-grained tonalites to granodiorite sheets with increasing SiO_2. K_2O exhibits a positive trend across all rock types with increasing SiO_2; granodiorite sheets having the highest K_2O content. L.O.I values on Figure 5.1j display a scattered distribution, where there is no trend between L.O.I values and SiO_2 whereas L.O.I values on Figure 5.1k show a positive correlation with MgO

Trace element Harker plots are plotted in Figure 5.2. The elements included in these plots are rare earth elements (REE) La, Lu, P and Eu, large-ion lithophile elements (LILE) Rb, Ba and

Cs, high-field strength element (HFSE) Zr and a siderophile element Ni. Some of the Harker plots display linear trends, whereas some plots do not display clear patterns between the rock types. Generally, the coarse-grained trondhjemite samples are less enriched in trace elements than the fine and medium-grained tonalite samples. In general, the coarse-grained trondhjemite sample data cluster in a group on the trace element plots, whereas the tonalites display a wider scatter. The coarse-grained trondhjemites have Sc concentrations ranging from 4.5-10 ppm. The fine to medium-grained tonalites have Sc concentrations ranging from 5 to 15 ppm. The V-Zr plot shows that the tonalites have V contents ranging between 20 and 95 ppm. The coarse-grained trondhjemites have V compositions ranging between 10 and 18 ppm. On the Cr-Zr plot, the tonalites display Cr compositions between 10 and 80 ppm. The Cr content in the coarse-grained trondhjemitic rocks ranges between 9 and 20 ppm. The Co-Zr plot displays tonalites with Co concentrations that fall between 4 and 19 ppm. The coarse-grained trondhjemites have Co concentrations of approximately 3 ppm. The Cu-Zr plot does not show clear patterns and all the rock samples have Cu contents which are below and approximately 50 ppm. One fine-grained sample (CT1) is the only exception with a Cu concentration of 1118 ppm. The Mo-Zr Harker plot shows that the tonalite samples have Mo contents between 0.8 and 1.25 ppm. The coarse-grained trondhjemites have Mo contents between 0.65 and 0.91 ppm. The Ba-Zr plot displays tonalites with Ba contents ranging between 390 and 1000 ppm. The plot shows that the coarse-grained trondhjemites have concentrations between 300 and 900 ppm. The Cs-Zr plot shows Cs concentrations between 3 and 10 ppm in fine to medium-grained tonalites. The coarse-grained trondhjemites have Cs concentrations ranging between 1 and 5 ppm.

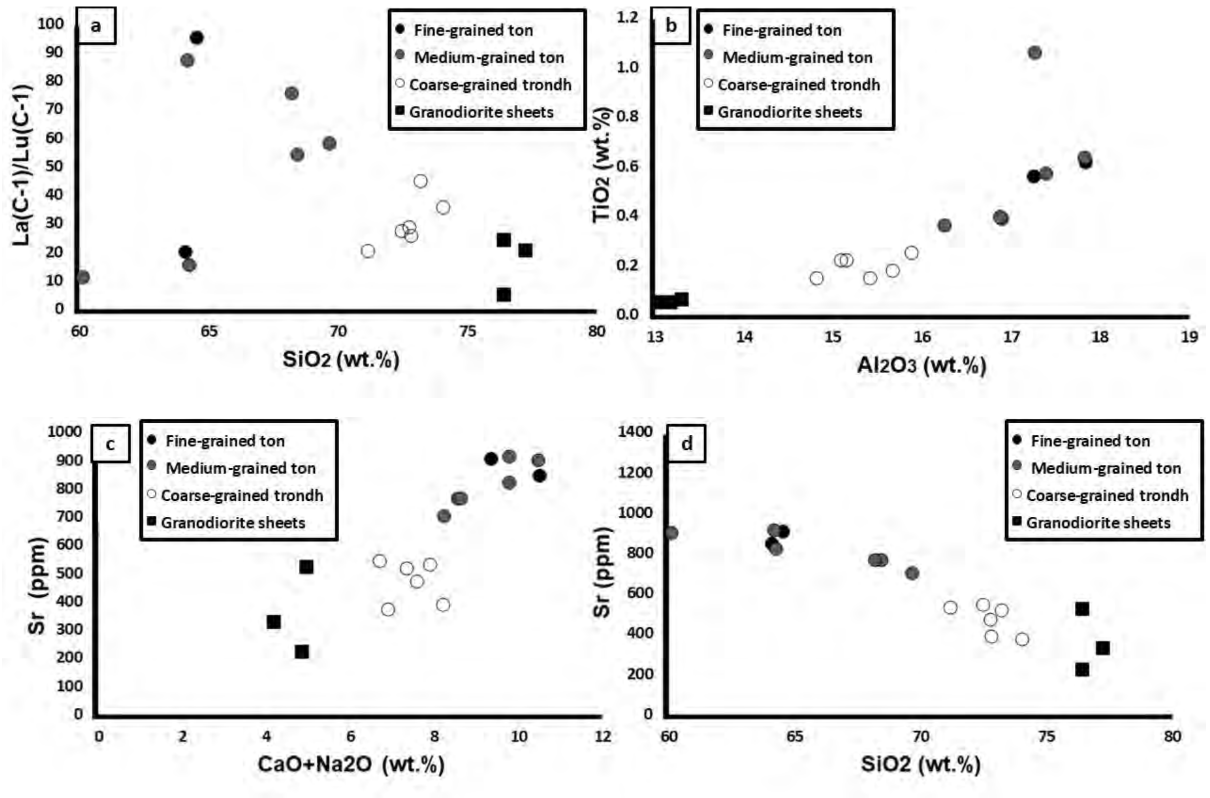

Figure 5.2: *Major element vs trace element Harker plots (a) SiO_2 vs $La(C_1)/Lu(C_1)$, (b) Al_2O_3 vs TiO_2, (c) $CaO+Na_2O$ vs Sr and (d) SiO_2 vs Sr. Abbreviations: C1- normalized to C1-Chondrite.*

Figure 5.2 (a) above shows a negative trend where $La(C_1)/Lu(C_1)$ ratios for coarse-grained trondhjemites ranges from 20 to 48 ppm (C1 = C1 Chondrite). The $La(C_1)/Lu(C_1)$ ratio for fine to medium-grained tonalites is between 10 and 100 ppm and that of the felsic granodiorite sheets is between 5 and 25 ppm.

Figure 5.2 (b) shows a positive trend with granodiorite sheets and coarse-grained trondhjemites with the lowest concentrations of TiO_2 and Al_2O_3. Granodiorite sheets have TiO_2 concentrations ranging between 0 and 1 wt.% as well as Al_2O_3 concentrations of ~13 wt.%. The coarse-grained trondhjemites have TiO_2 concentrations ranging between 0.1 and 0.3 wt.% as well as Al_2O_3 contents falling between 14.7 and 16 wt.%. The TiO_2 contents of the fine to medium-grained tonalites falls between 0.4 and 1.1 wt.% and the Al_2O_3 content of fine to medium-grained tonalites ranges between 16.2 and 18 wt.%. The coarse-grained samples are seen to form a cluster unlike the slightly scattered fine to medium-grained samples. This clustering suggests that the compositions of the coarse-grained trondhjemites are almost identical to one another. Figure 5.2 (c) shows a positive linear trend where Sr concentrations of granodiorite sheets fall between 200 and 550 ppm and CaO+Na_2O concentration ratios are between 4 and 5 wt.%. The coarse-grained trondhjemites show Sr contents ranging between 350 and 600 ppm as well as CaO+Na_2O contents ranging between 6.2 and 8.2 wt.%. The Sr contents in fine to medium-grained tonalites falls between 700 and 950 ppm whereas the CaO+Na_2O contents fall between 8 and 11 wt.%. Figure 5.2 (d) shows a negative linear trend with the same Sr contents as figure 5.2 (c). The SiO_2 contents of granodiorite sheets falls between 76 and 78 wt.% whereas that of coarse-grained trondhjemites falls between 71 and 74.5 wt.%. Fine to medium-grained tonalites have SiO_2 concentrations ranging between 60 and 70 wt.%.

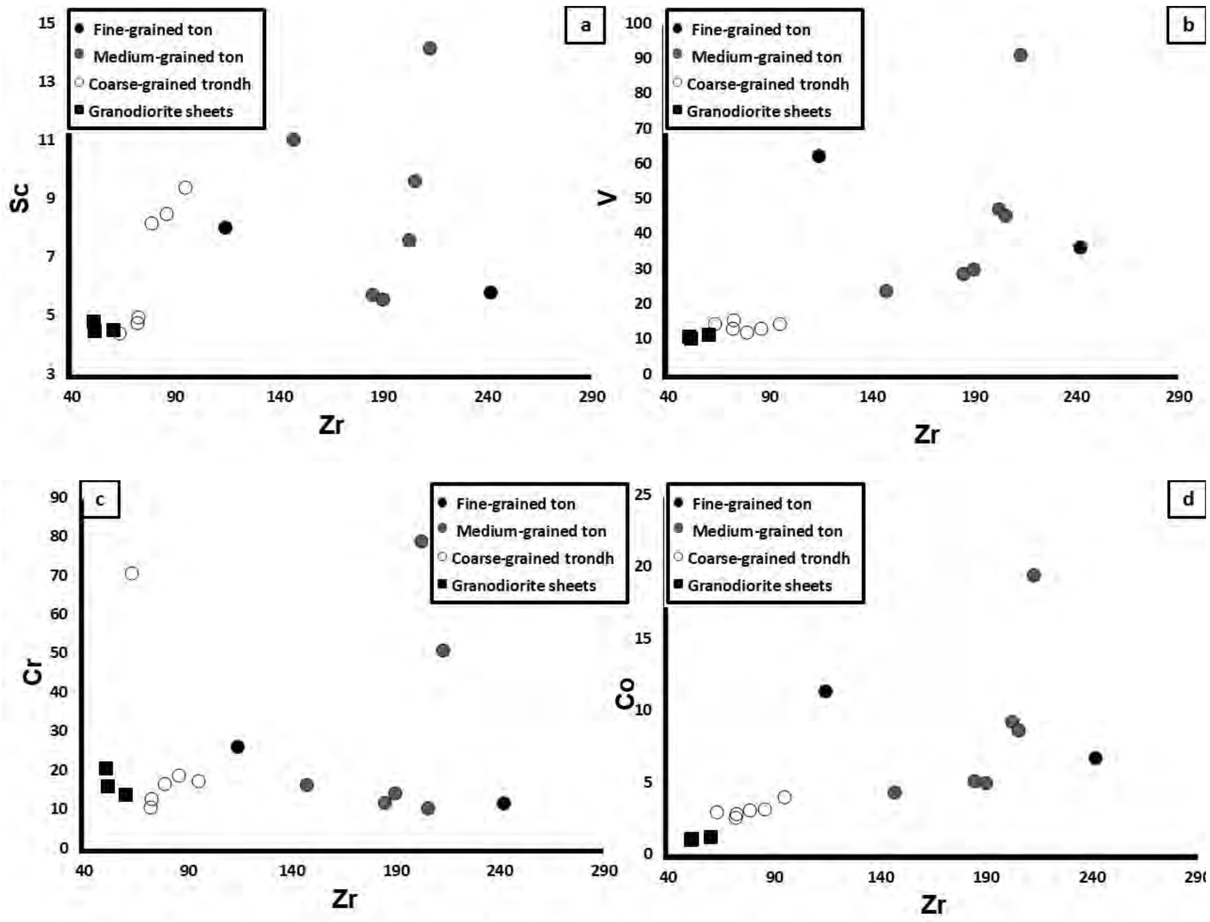

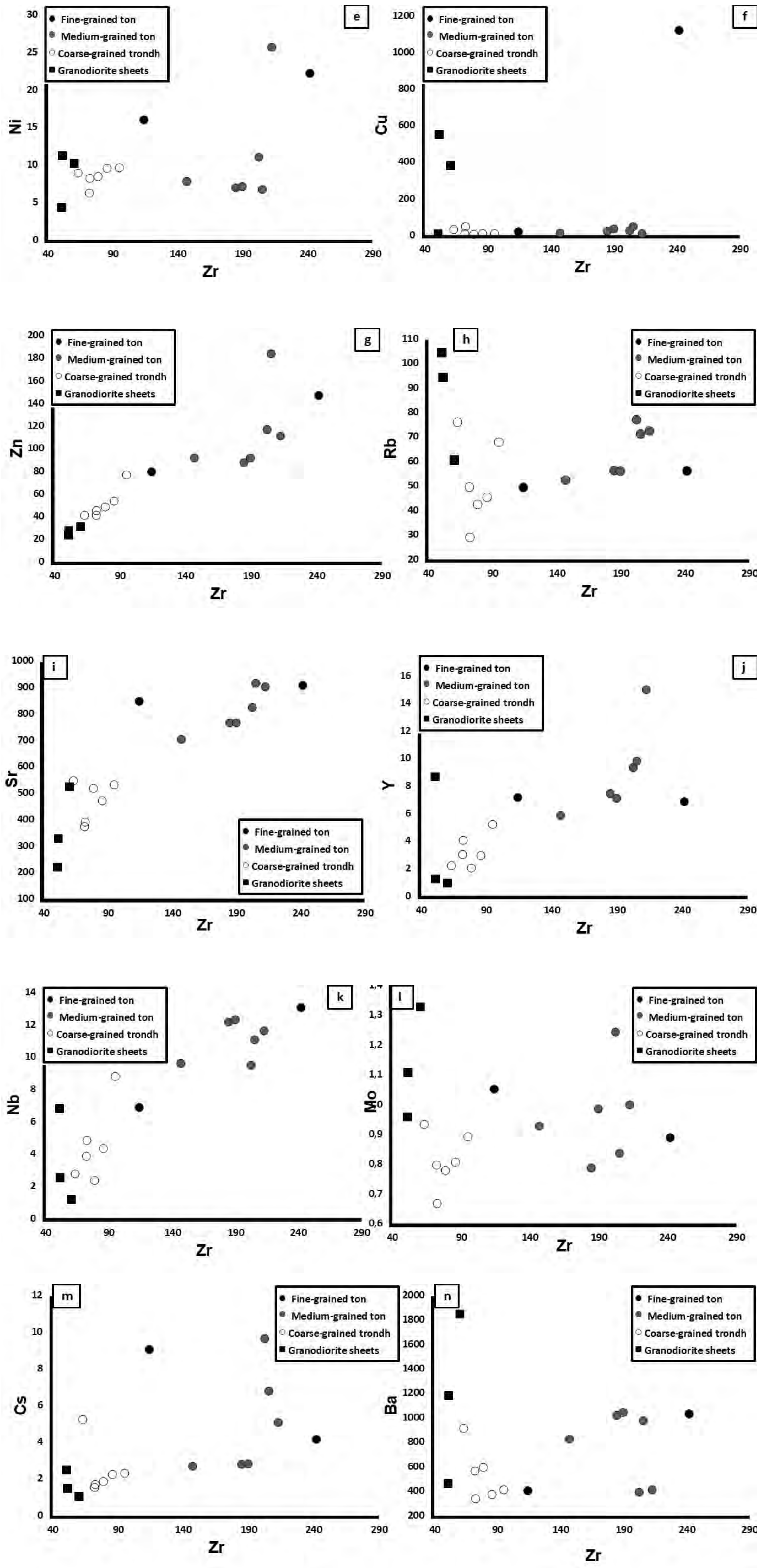
e
Ni
Zr
f
Cu
Zr
g
Zn
Zr
h
Rb
Zr
i
Sr
Zr
j
Y
Zr
k
Nb
Zr
l
Mo
Zr
m
Cs
Zr
n
Ba
Zr
Fine-grained ton
Medium-grained ton
Coarse-grained trondh
Granodiorite sheets

__Figure 5.3__: Trace element Harker plots for the Stolzburg pluton TTGs using Zr as the index of differentiation. Trace elements are recorded in parts per million (ppm).

On the trace element Harker diagrams on Figure 5.3 g, j, k, and l, there is a positive linear trend between Zr and the trace elements Zn, Y, Sr, and Nb. The coarse-grained samples are less clustered and the medium grained samples are less dispersed than on the previously discussed Harker plots. The tonalites on the Zn-Zr plot show Zn concentrations between 80 and 190 ppm. The coarse-grained rocks show Zn concentrations ranging between 40 and 80 ppm. The Sr-Zr Harker plot shows that the tonalites have Sr contents that fall between 700 and 910 ppm. The coarse-grained trondhjemites record Sr contents between 360 to 550 ppm. The Y-Zr plot shows that the Y concentration in the tonalites ranges 6 and 15 ppm, whereas the coarse-grained trondhjemites show Y concentrations ranging between 2 and 5.8 ppm. The Nb-Zr Harker plot displays fine to medium-grained tonalites with Nb concentrations ranging from 7 to 13 ppm. The coarse-grained trondhjemite samples have Nb contents between 2 and 9 ppm. Generally, the coarse-grained samples are less enriched in trace elements than the fine and medium grained samples.

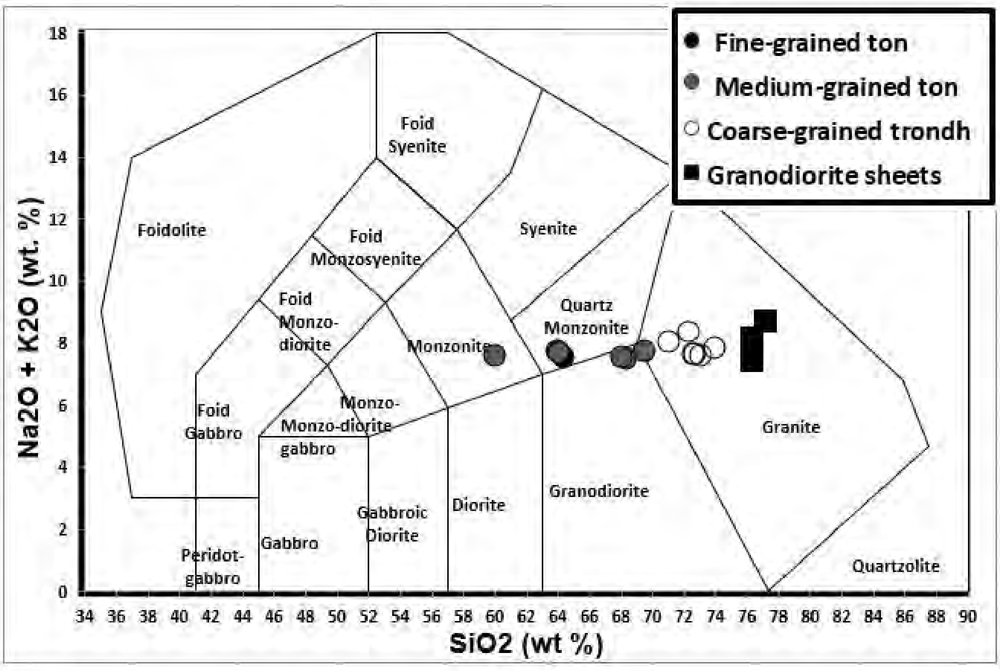

__Figure 5.4__: TAS (total alkali vs SiO_2) diagram (after Cox et al., 1979) showing the major elements features of the Stolzburg pluton TTG samples.

The granodiorite sheets and the coarse-grained TTGs plot in the granite field of the TAS diagram whereas the fine to medium-grained tonalites plot in the quartz monzonite field and granodiorite fields due to low SiO_2 concentrations, indicating an intermediate composition.

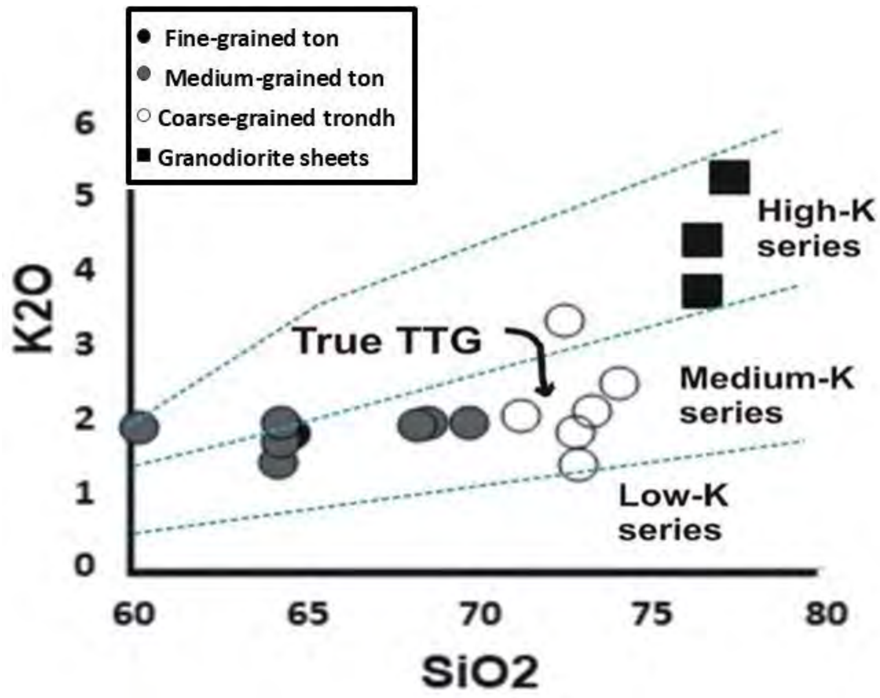

***Figure 5.5**: Discriminant diagram showing the relationship between coarse, medium and fine grained TTGs (Peccerillo and Taylor, 1976).*

The K_2O vs SiO_2 diagram (Figure 5.5) is typically used for granitoid classification with high to low K series. It shows most of the TTG samples plotting on the true TTG domain series except for two samples (one medium grained and one coarse grained) plotting in the high-K series. All the granodiorite sheets plot in the high-K series.

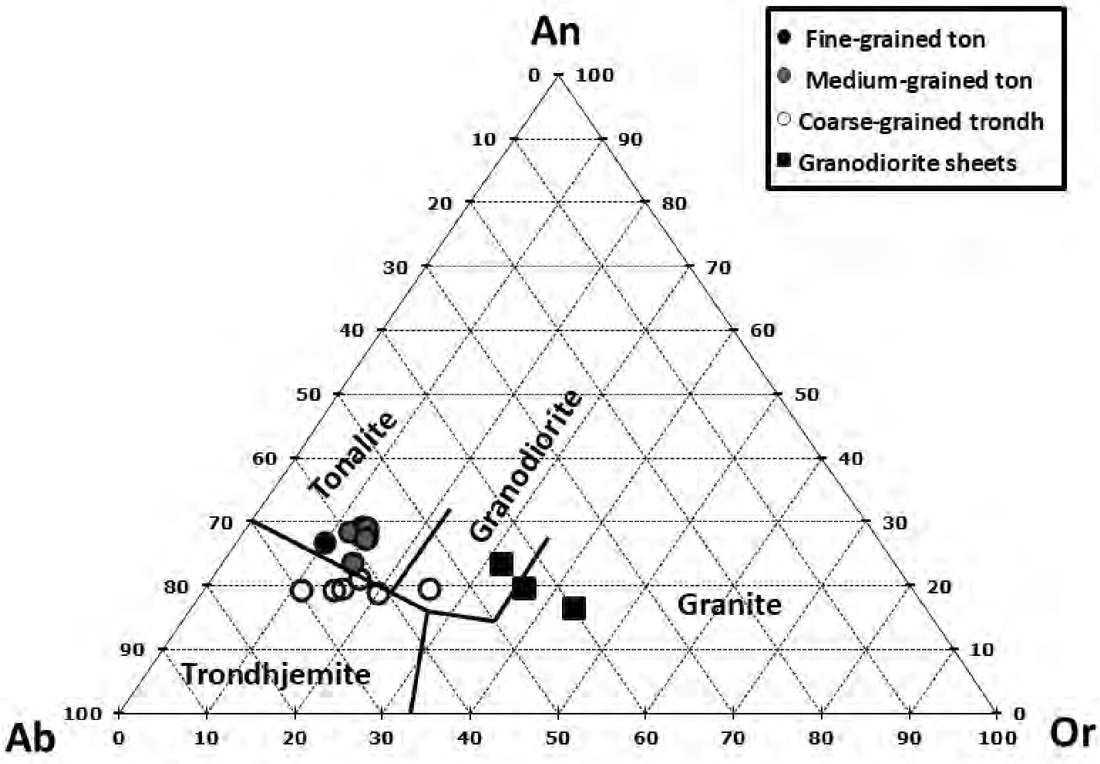

Figure 5.6. *Normative ternary diagram (after Barker, 1979) that classifies TTGs into tonalites, trondhjemites and granodiorites using calculated model abundance of feldspar end-members [Anorthite ($CaAl_2Si_2O_8$) Albite ($NaAlSi_3O_8$) Orthoclase ($KAlSi_3O_8$)].*

Figure 5.6 is a normative ternary diagram that classifies the TTGs and the calculated modal abundances of anorthite, albite and orthoclase are presented in Appendix B. On the An-Ab-Or ternary diagram shown above (Figure 5.5), the Archean TTGs appear to have high Na_2O contents and low K_2O contents as they plot closer to the albite (Ab) domain. The fine-grained tonalites cluster within the tonalite field, the medium-grained tonalites similarly plot in the tonalite field while some samples plot closer and on the granodiorite boundary, indicating a subtle increase in the orthoclase (Or) content. The coarse-grained trondhjemites plot largely in the trondhjemite field; one sample plots in the tonalite field and another sample plots in the granodiorite field. The felsic sheets plot in the granodiorite field reflecting increased modal abundance.

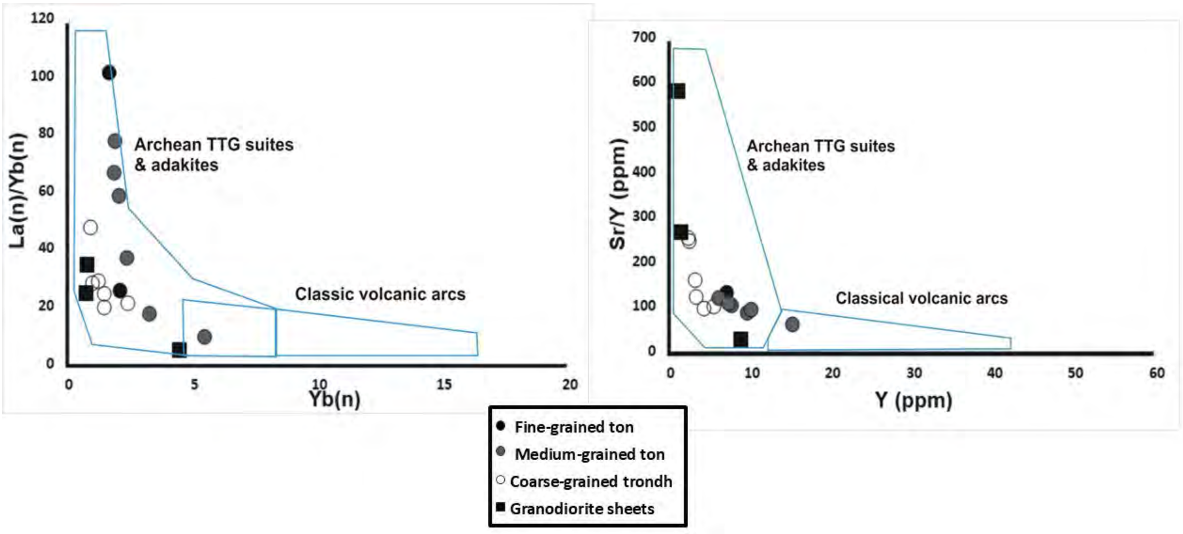

Figure 5.7: *Discriminant diagrams that differentiate between Archean TTGs and modern arc related magmas (*Martin, *1986).*

TTG samples have high contents of LREEs (La average = 20.22 ppm) but quite low HREE contents (Yb average =0.44 ppm) which results in high La/Yb ratios ((La/Yb) average = 45.95 ppm; Moyen *et al*., 2007; Liou and Guo, 2019). Archean TTGs also have high Sr contents (Sr average = 619.15 ppm) and low Y contents (Y average = 5.81 ppm) resulting in high Sr/Y ratios ((Sr/Y) average = 106.57 ppm; Moyen *et al*., 2007; Liou and Guo, 2019). Figures 5.6 (a and b) indicate that the Stolzburg pluton TTGs define a sub-vertical trend. On Figure 5.7 (a), the coarse-grained samples cluster together at the bottom of the diagram. The medium-grained and fine-grained samples are scattered but within the Archean TTG suite portion. In Figure 5.7 (b), all the samples cluster at the bottom of the diagram, except for one felsic granodiorite sheet sample.

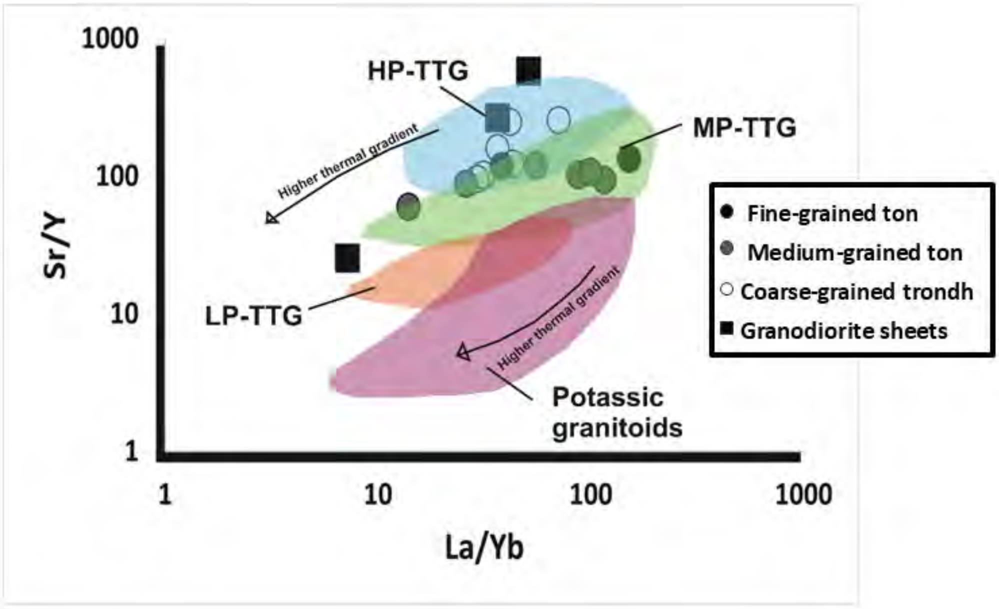

Figure 5.8: *A trace element ratio diagram (after Moyen, 2011) showing pressure classification systems for TTGs. Abbreviations: HP-TTG: High pressure TTG. MP-TTG: Medium pressure TTG. LP-TTG: Low pressure TTG.*

In a Sr/Y versus La/Yb diagram (Figure 5.8), there are no TTG samples on the Low Pressure-TTG and potassic granitoids fields. Most TTG samples fall on the Medium Pressure-TTG and High P-TTG intersection area. All the fine to medium-grained tonalite fall on the Medium

Pressure- TTG area. Some coarse-grained trondhjemites fall on the High Pressure-TTG space and some coarse-grained trondhjemites intersect the Medium Pressure and High Pressure TTG areas. One felsic sheet sample falls on neither of the areas highlighted on the diagram.

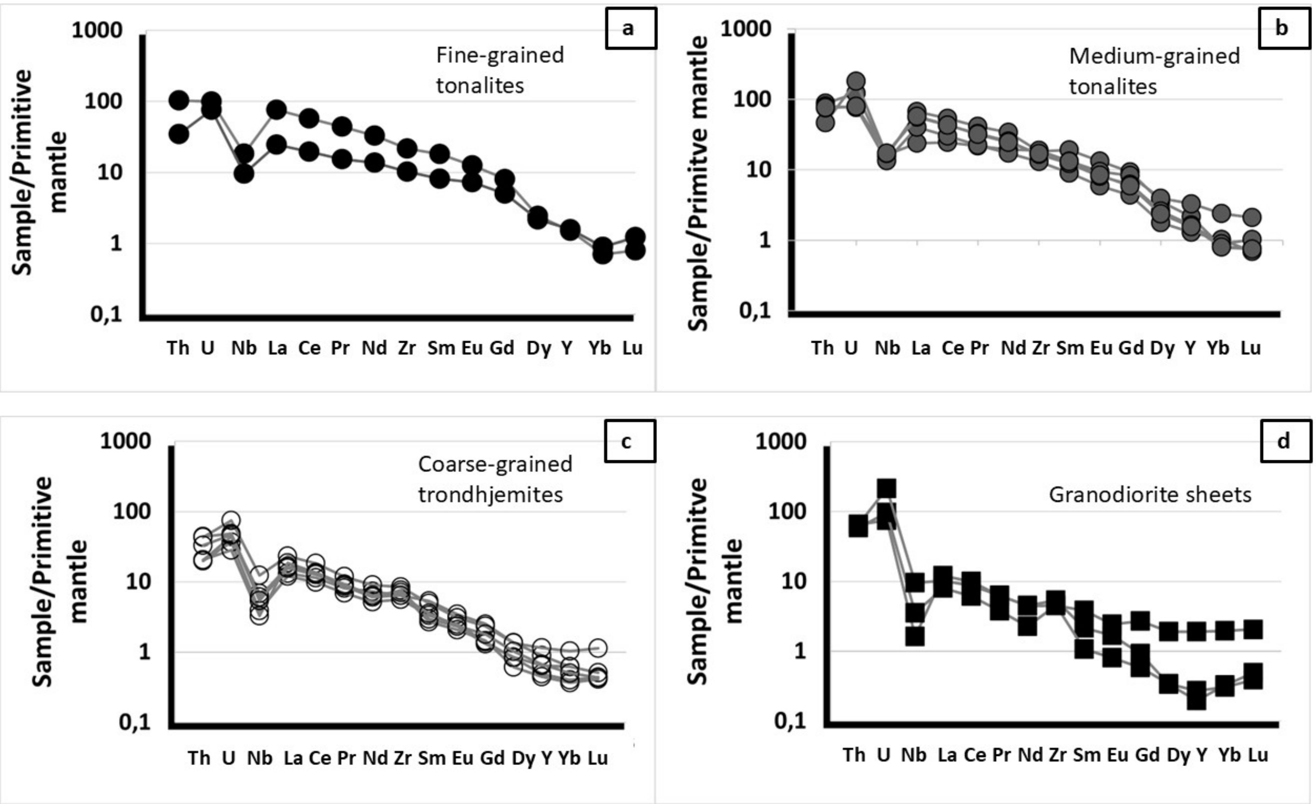

Figure 5.9*: (a) Primitive mantle normalized (Sun and McDonough, 1989) plot of fine-grained tonalites, (b) primitive normalized mantle plot of medium-grained tonalites (Sun and McDonough, 1989), (c) primitive mantle plot for coarse-grained trondhjemites (d) primitive mantle plot of granodiorite sheets (Sun and McDonough, 1989).*

Cs, Rb, Ba are not included on the primitive mantle normalized plots (Figure 5.9) because they tend to be mobile during metamorphism (Huang *et al*., 2010). The fine- and medium-grained tonalite and trondhjemite samples in Figure 5.9 (a, b and c) all record primitive mantle normalized plots that have negative slopes, they are enriched in LREEs and depleted in HREEs. All the plots display a significant negative Nb anomaly. Figure 5.9 (a, b and c) shows that the fine-, medium- and coarse-grained samples are depleted in HREEs uniformly whereas there is a fluctuating pattern in Figure 5.9 (c). Figure 5.9 (b) shows a weak negative Yb anomaly in fine- and medium-grained tonalite samples. Figure 5.9 (c) shows an enrichment in the Zr contents of felsic granodiorite sheets and a negative Y anomaly in two of the felsic granodiorite sheet samples.

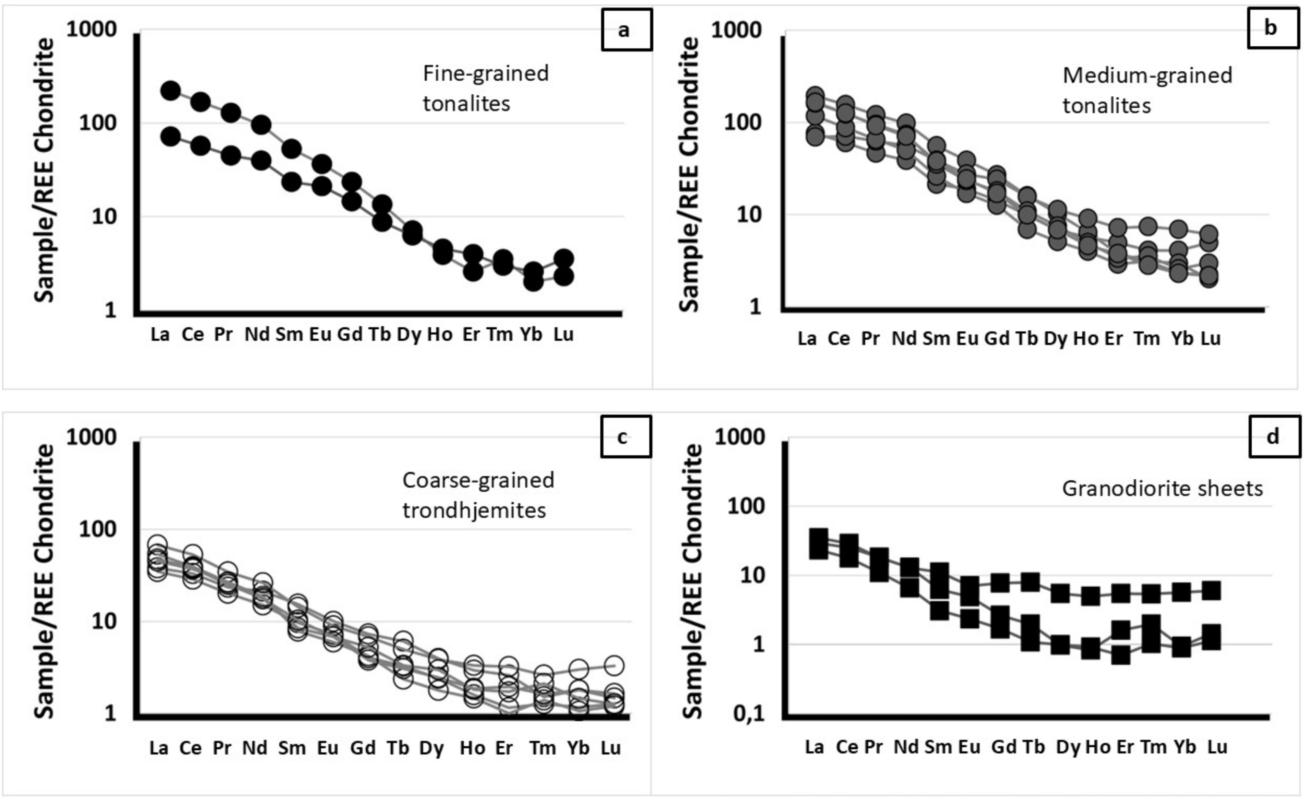

***Figure 5.10**: C1-Chondrite normalized (Sun and McDonough, 1989) Rare Earth Element (REE) plots of (a) fine-grained tonalites, (b) medium-grained tonalites, (c) coarse-grained trondhjemites (d) felsic sheets.*

C1-chondrite normalized plots have been plotted in Figure 5.10 to provide REE patterns for the rock types. All the plots show enriched LREE and depleted in HREE. There are no anomalies observed in both Figures 5.10a and 5.10b but a minor negative Tm anomaly is seen in Figure 5.10c. Weak Eu anomalies are also present, particularly in the granodiorite sheets.

5.4 Comparison of Stolzburg Pluton Crushers' quarry data with published Stolzburg Pluton data.

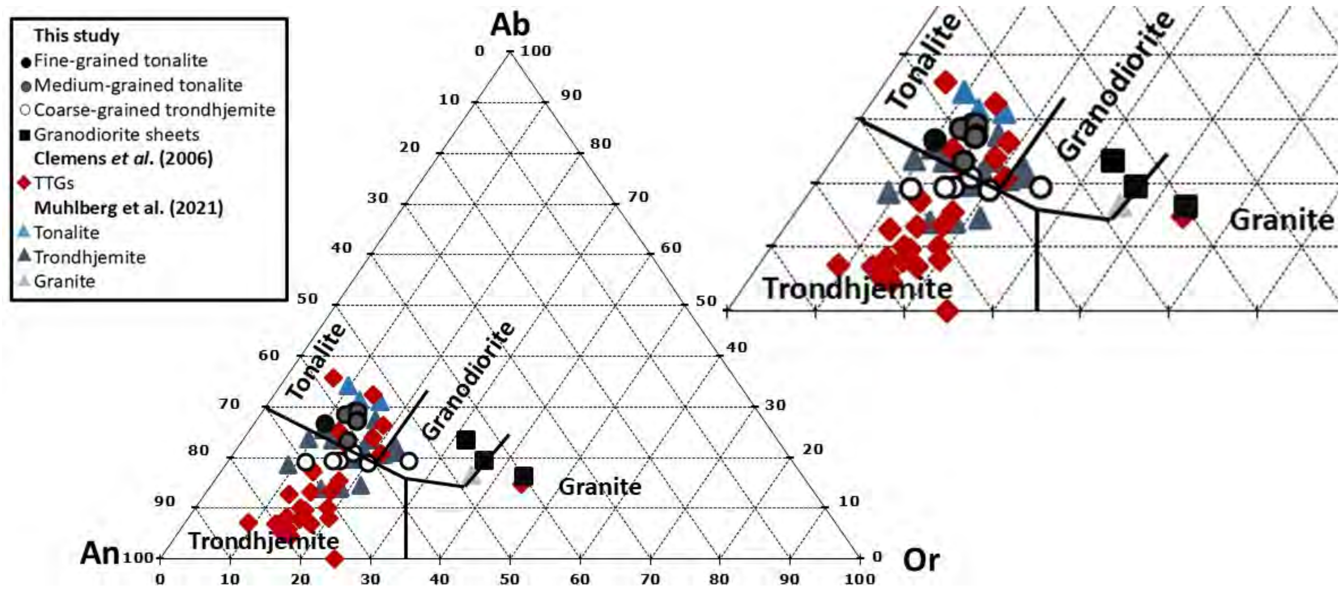

***Figure 5.11**. A ternary diagram (modified after Barker, 1979) classifying samples from this study, Muhlberg et al. (2021) and Clemens et al. (2006).*

Fine-grained tonalite and medium-grained tonalite generally plot in the tonalite region. Coarse-grained trondhjemite samples are concentrated toward the trondhjemite region, indicating distinct compositional variation. The granodiorite samples are clearly distinguished from the other types and plot between tonalite and granite, consistent with their classification. TTGs from Clemens *et al*. (2006) cluster near the trondhjemite and tonalite regions with one sample falling on the granite field. Muhlberg *et al*. (2021) samples show a broad range of compositions across tonalite, trondhjemite, granodiorite and granite fields.

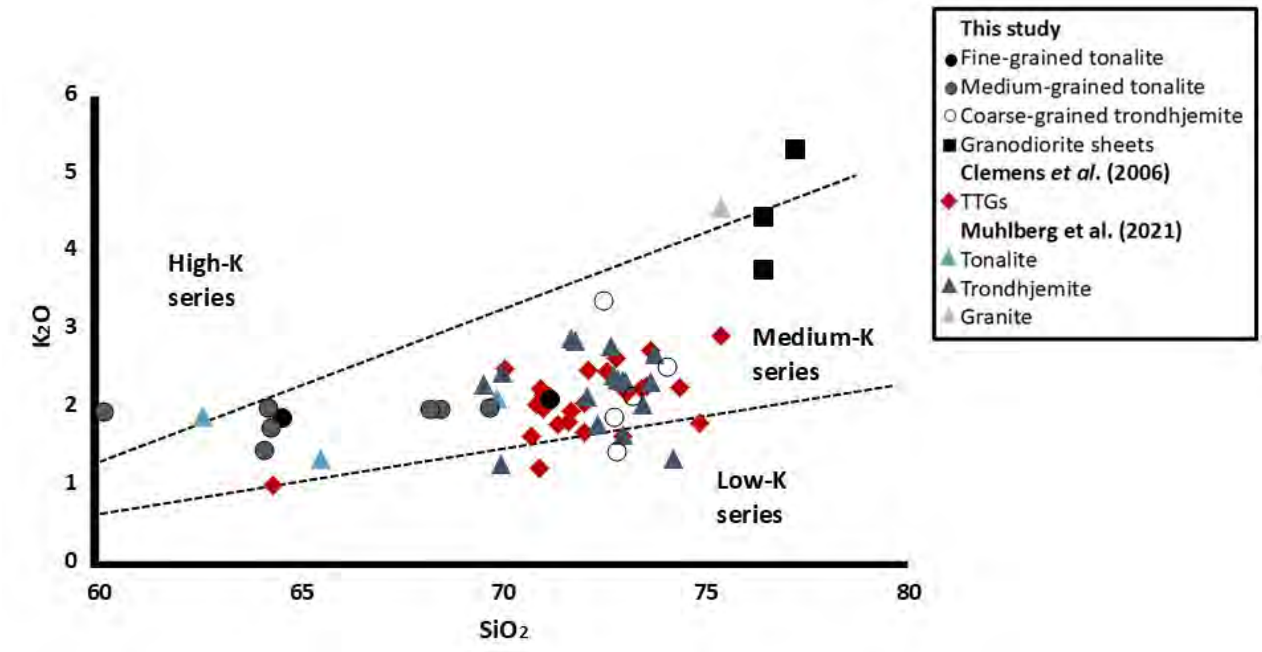

Figure 5.12. *K_2O–SiO_2 (wt.%) plot showing the fields defined by Le Maitre et al. (1989) for this study, including Muhlberg et al. (2021) and Clemens et al. (2006) data.*

Fine-grained and medium-grained tonalites from this study are primarily distributed in the low-K series field, with a few samples trending into the medium-K series field as SiO_2 increases. Coarse-grained trondhjemites from this study largely fall within the low-K series, with minimal scatter. TTG samples from Clemens *et al*. (2006) primarily plot in the medium-K series, showing a broad distribution across the SiO_2 range. Muhlberg *et al*. (2021) tonalites and trondhjemites cluster around the low- to medium-K boundary and shift to higher K_2O as SiO_2 increases. Granodiorites from this study show elevated K_2O, consistently plotting in the high-K series, highlighting their more evolved nature. Overall, the data show a general trend of increasing K_2O with SiO_2 for all rock types, particularly in the granodiorite and Clemens *et al*. (2006) TTG samples.

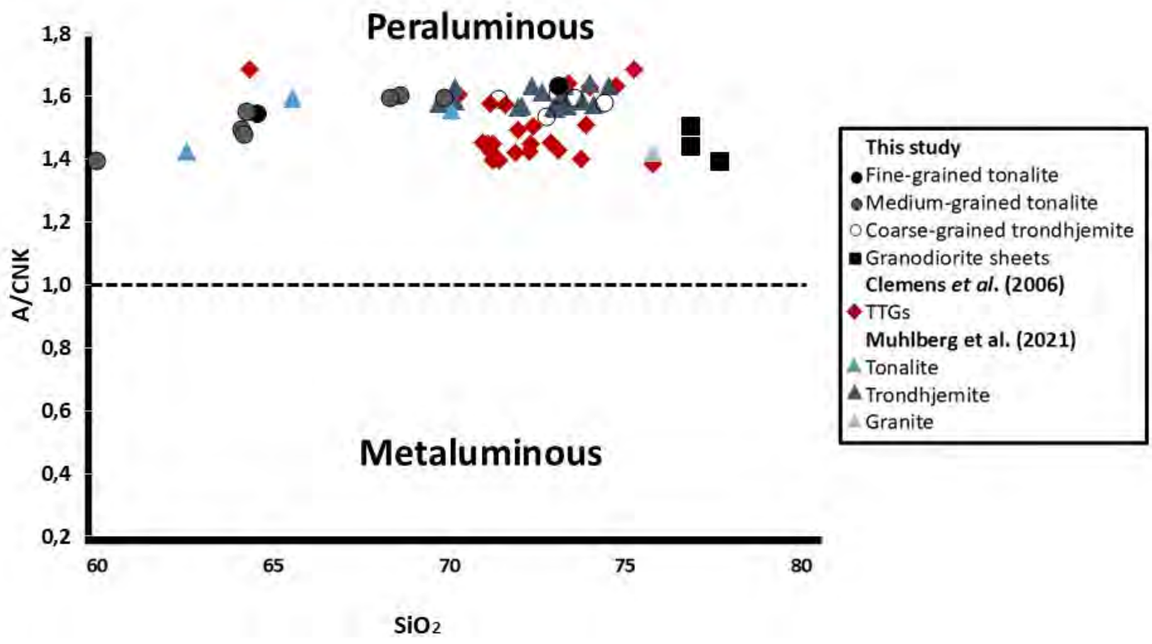

Figure 5.13. *A/CNK–SiO_2 (wt.%) plot for the TTG rocks from this study, Muhlberg et al. (2021) and Clemens et al. (2006). A/CNK=mol Al_2O_3/(CaO+Na_2O+K_2O).*

Fine-grained and medium-grained tonalites from this study predominantly plot in the peraluminous field, indicating alumina saturation with values well above 1. Coarse-grained trondhjemites (open circles) are also in the peraluminous field, with some clustering toward the lower boundary. TTG samples from Clemens *et al*. (2006) also fall in the peraluminous field. Muhlberg *et al*. (2021) tonalites and trondhjemites entirely plot in the peraluminous field, showing limited variability. Granodiorites from this study remain solidly within the peraluminous field, highlighting their highly evolved geochemical signature.

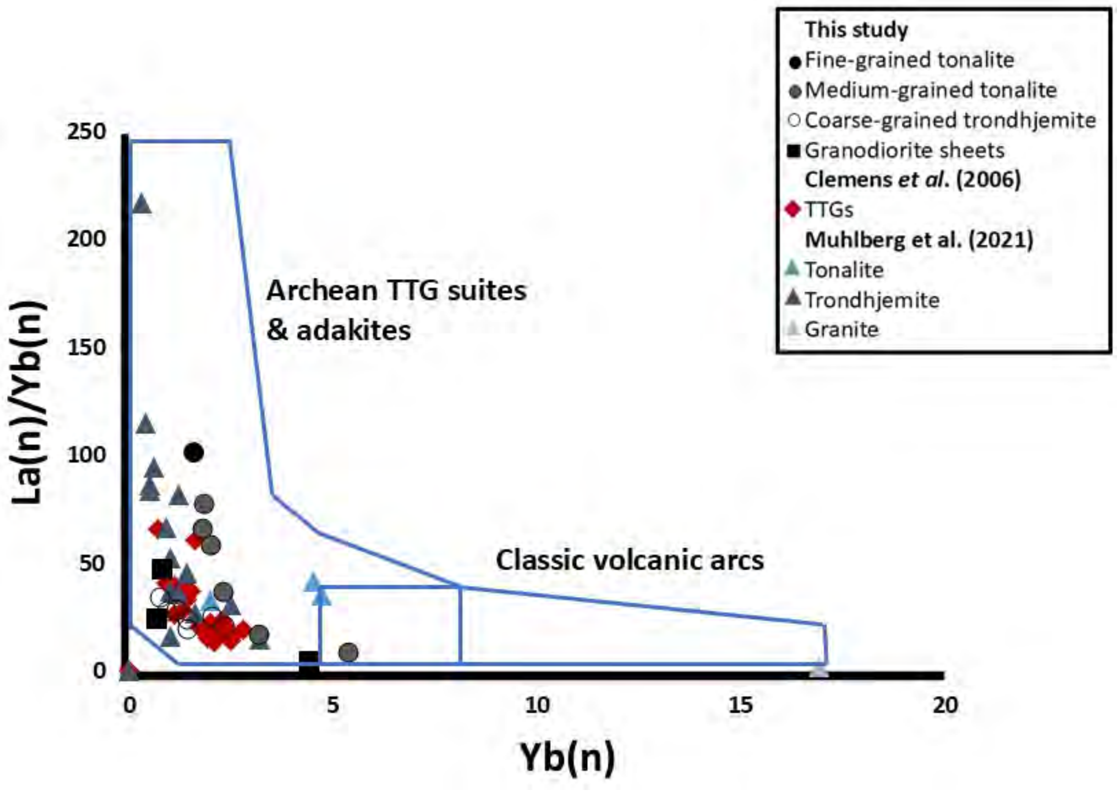

Figure 5.14. *La(n)/Yb(n) vs Yb(n) diagram that differentiates between Archean TTGs and modern arc related magmas (*Martin*, 1986).*

The La(n)/Yb(n) versus Yb(n) diagram, compares geochemical data from this study, Clemens *et al*. (2006), and Muhlberg *et al*. (2021). The plot differentiates between Archean TTG suites & adakites and classic volcanic arcs based on a blue boundary trend. Fine-grained tonalites from this study and medium-grained tonalites are mostly clustered within the Archean TTG suites & adakites field. They exhibit high La(n)/Yb(n) values at low Yb(n). Coarse-grained trondhjemites and granodiorite sheets also plot in the TTG-adakite field, reinforcing a trend toward high La(n)/Yb(n) ratios. Clemens *et al*. (2006) TTGs are tightly clustered within the Archean TTG suites & adakites field. Their distribution aligns with the expected geochemical characteristics of TTGs, with high La(n)/Yb(n) values. Most Muhlberg *et al*. (2021) tonalites and trondhjemites fall within the Archean TTG suites & adakites field. Some samples extend towards the classic volcanic arcs field at higher Yb(n) and lower La(n)/Yb(n).

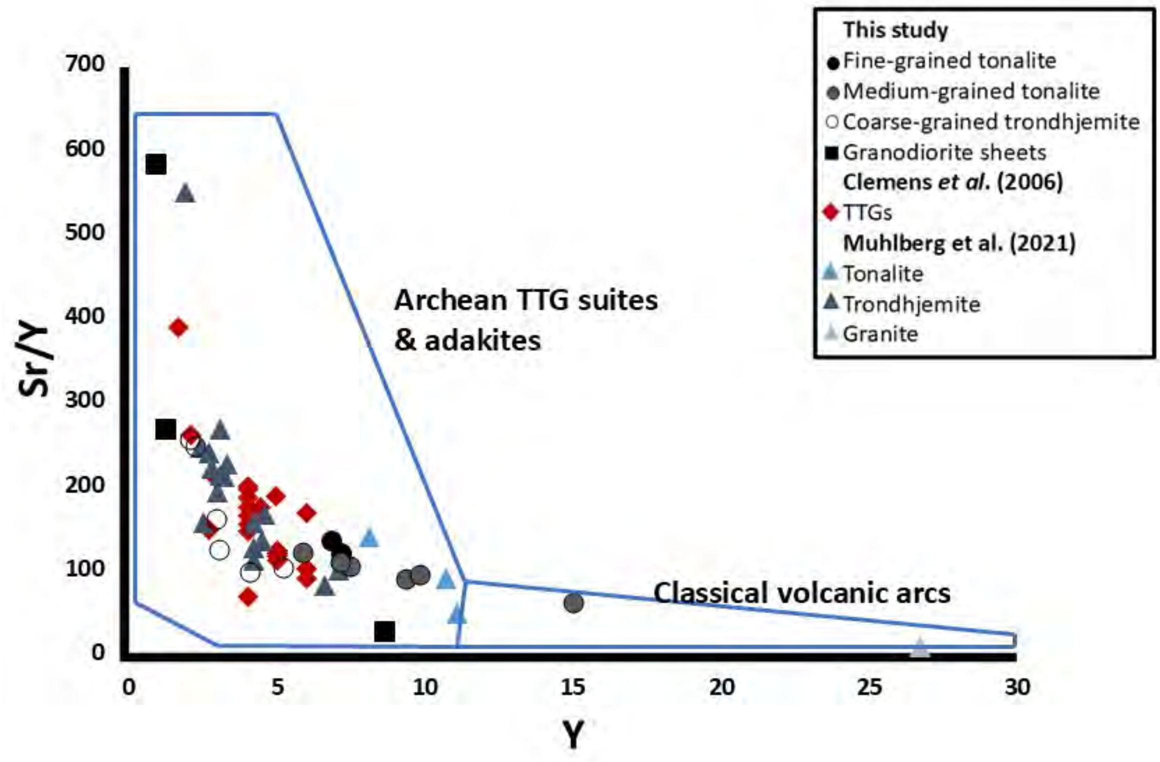

Figure 5.15. *Sr/Y vs Y diagram that differentiates between Archean TTGs and modern arc related magmas (Martin, 1986).*

The Sr/Y versus Y diagram (Figure 5.15), compares geochemical data from this study, Clemens *et al*. (2006), and Muhlberg *et al*. (2021). As in Figure 5.14, the data is classified into Archean TTG suites & adakites and classical volcanic arcs, separated by a blue boundary trend. Fine-grained tonalites and medium-grained tonalites from this study cluster mostly within the Archean TTG suites & adakites field, showing high Sr/Y at low Y values. Coarse-grained trondhjemites and granodiorite sheets also fall within the TTG-adakite field, with a decreasing Sr/Y trend at increasing Y. TTGs From Clemens *et al*. (2006) are concentrated in the Archean TTG suites & adakites domain, displaying high Sr/Y ratios consistent with high-pressure melting processes. Most tonalites and trondhjemites from Muhlberg *et al*. (2021) plot in the Archean TTG suites & adakites field, aligning with high-pressure conditions. A few samples, particularly at higher Y values, extend into the classical volcanic arcs field, showing lower Sr/Y ratios.

5.5 Geochemical characterization of amphibolite xenoliths

This section presents the bulk geochemistry of the 5 amphibolite rock samples, namely mafic amphibolite xenoliths contained within the Stolzburg pluton at Crusher's Quarry.

Table 5.2: *Major element (wt.%) and trace element (ppm) data of 5 amphibolite samples from Crusher's Quarry, Barberton. Abbreviations: bdl = below detection limit, L.O.I= loss on ignition.*

Sample	CT4	CT10	CT11	CT15	CT18
SiO_2	48.07	49.75	49.02	48.46	45.53
TiO_2	0.82	0.75	0.76	0.91	0.62
$Al2O_3$	11.49	9.64	9.46	10.39	12.37
Fe_2O_3	12.34	12.22	12.65	12.64	11.09
FeO^T	11.1	11.0	11.38	11.37	9.98
MnO	0.20	0.20	0.21	0.21	0.15
MgO	12.14	13.23	13.61	12.62	15.85
CaO	6.82	8.23	7.98	9.12	4.85
Na_2O	0.97	0.94	0.62	1.68	0.89
K_2O	5.79	3.70	4.39	1.96	3.96

Table 5.2 *(cont).*

P_2O_5	0.06	0.07	0.07	0.09	0.03
Cr_2O_3	0.16	0.17	0.18	0.16	0.25
L.O.I	0.94	1.12	0.87	1.39	4.69
Sum of conc.	**99.81**	**100.02**	**99.82**	**99.63**	**100.28**
Sc	24.5	23.8	25.1	26.7	25.2
V	159.6	171.7	181.7	189.9	166.8
Cr	1020.3	1127.9	1148.3	1134.1	1773.4
Co	60.1	63.5	67.0	66.7	70.6
Ni	463.4	544.1	538.8	498.4	824.5
Cu	10.2	26.8	92.8	130	6.2
Zn	147.3	122.7	116.5	116	108.7
Rb	228.9	123.6	131.3	67.7	230.8
Sr	151.1	120.3	118.5	208.3	88.5
Y	10.3	15.8	15.2	17.6	9.3
Zr	60	60.2	60.4	71.5	48.5
Nb	10.1	6.5	5.8	7	8.2
Mo	0.7	0.7	0.6	0.9	0.7
Cs	25.0	17.7	14.8	12.3	94
Ba	487.4	239.2	218.8	141.1	333.8
La	5.8	6.4	6.0	8.1	4.7
Ce	13.9	15.3	14.7	19.6	9.9
Pr	1.8	2.1	2	2.6	1.2
Nd	8.7	9.5	9.6	11.7	4.9
Sm	2.1	2.4	2.4	3.3	1.2
Eu	0.6	0.9	0.8	1.0	0.3
Gd	1.9	2.9	2.8	3.2	1.5
Tb	0.3	0.5	0.4	0.5	0.2
Dy	1.9	2.9	2.9	3.6	1.7
Ho	0.4	0.6	0.6	0.7	0.3
Er	1.2	1.7	1.8	1.9	1
Tm	0.2	0.3	0.3	0.3	0.2
Yb	1.	1.5	1.8	1.8	1.1
Lu	0.2	0.2	0.2	0.3	0.2
Hf	1.6	1.7	1.5	1.9	1.7
Ta	0.4	0.4	0.3	0.4	0.5
Pb	6	16.5	6.7	3.8	1.4
Th	0.8	0.7	0.8	1.1	1.4
U	0.5	0.4	0.3	0.5	0.6

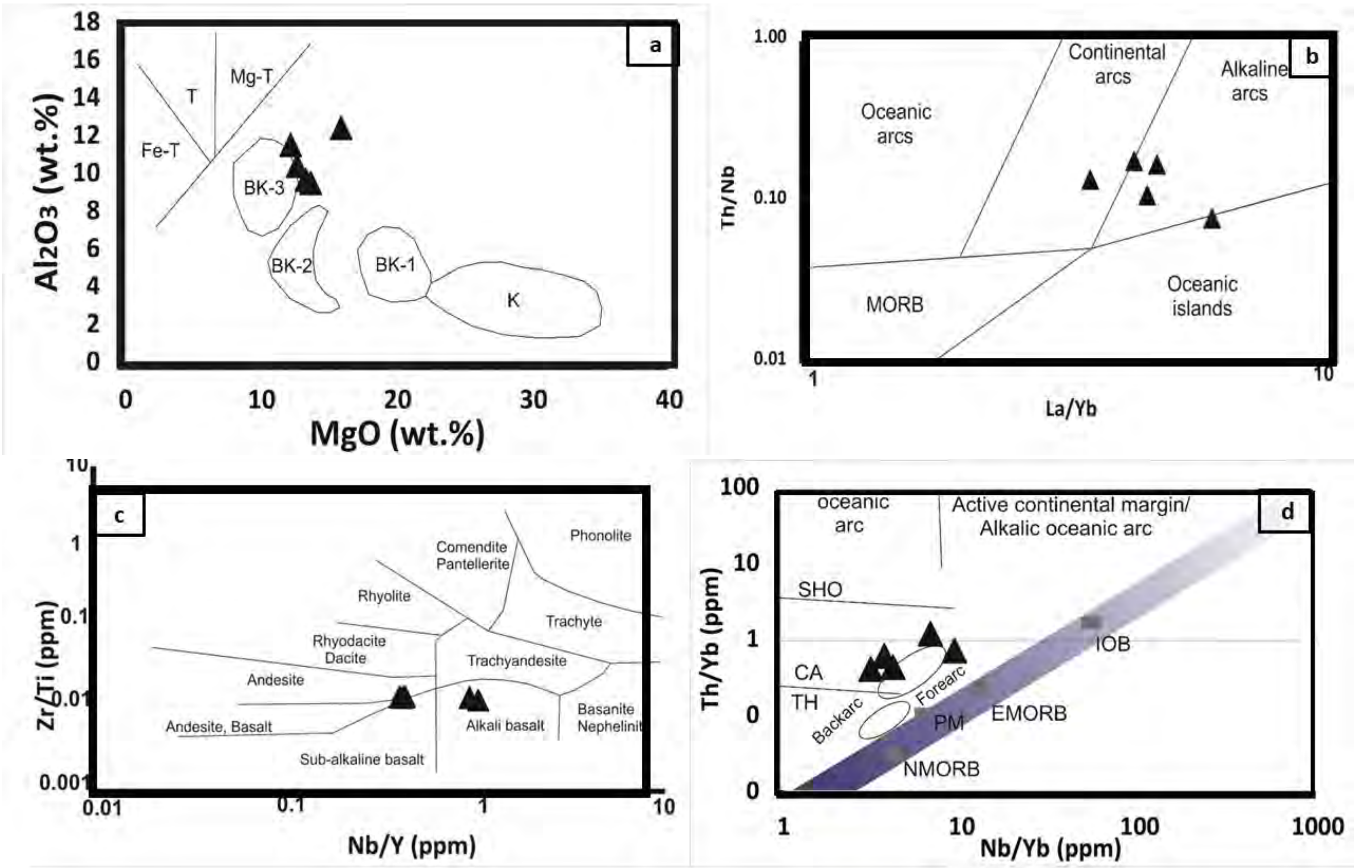

***Figure 5.16**. Major element and trace element ratio diagrams. (a) Al_2O_3 versus MgO diagram after (Viljoen et al., 1983; Pearce, 1996), (b) Th/Nb versus La/Yb diagram after (Hollocher et al., 2012), (c) Zr/Ti versus Nb/Y diagram and (d) Th/Yb versus Nb/Yb diagram*

after (Metcalf and Shervais, 2008). Abbreviations: Fe-T & Mg-T: Iron and Magnesium Tholeiite, T: Tholeiite BK-1: Geluk-type basaltic komatiites, BK-2: Badplaas-type basaltic komatiites, BK-3: Barberton-type basaltic komatiites, K: Komatiites, MORB: Mid-Oceanic Ridge Basalt, TH: Tholeiitic, CA: Continental Arc, SHO: Shoshonitic, IOB: Intra-oceanic basalt, EMORB: Enriched Mid-Oceanic Ridge Basalt, PM: Primitive Mantle, NMORB: Normal Mid-Oceanic Ridge Basalt.

The major element and trace element ratio plots in Figure 5.11 are useful in classifying the amphibolite protoliths. Figure 5.11 (a) shows one amphibolite sample plotting in the continental arcs field, three samples plotting in alkaline arcs and the last sample plotting between the alkaline arcs and oceanic islands fields. The amphibolite samples plot in the alkali basalt field and the rest of the amphibolites plot on the andesite, basalt and sub-alkaline basalt field boundaries on figure 5.11 (b). In the Th/Yb vs Nb/Yb diagram (Figure 5.11c by Pearce, 1996) shows the amphibolite samples plotting around the subduction-related forearc field above the mantle array. Figure 5.11 (d) is another classification diagram that shows amphibolites plotting between back arc basin and MORBs. These tectonic discrimination diagrams do have some limitations for Archean rocks, namely because the diagrams and their related fields are based on modern basalts. The amphibolites plot near the BK-3 field which is the Barberton basaltic komatiite type field at Al_2O_3 contents ranging between 8 and 13 wt.% and MgO contents ranging between 10 and 17 wt.% on Figure 5.11 (e).

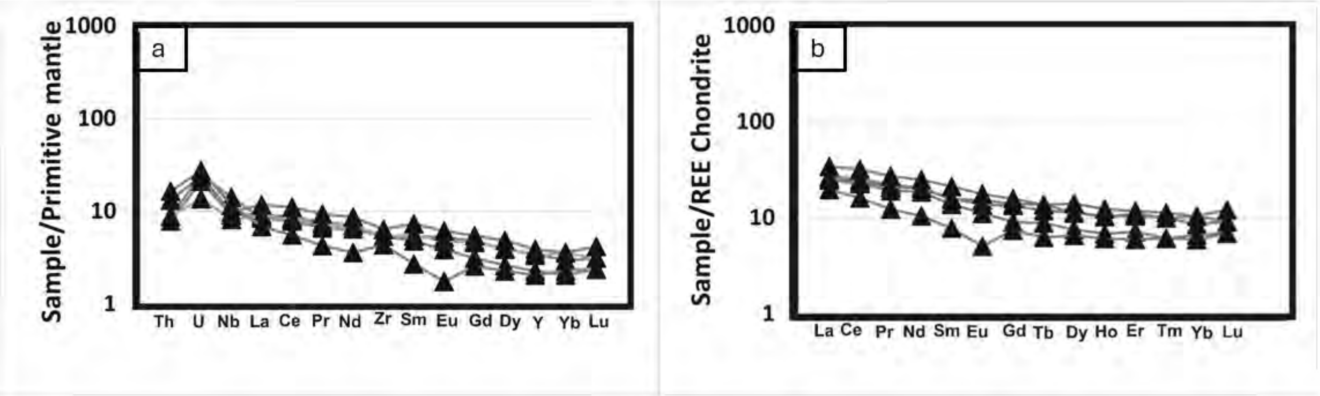

Figure 5.17: (a) *Primitive mantle normalized (Sun and McDonough, 1989) plot of amphibolites.* ***(b)*** *C1-Chondrite normalized (Sun and McDonough, 1989) Rare Earth Element (REE) plot of amphibolites.*

The primitive mantle plot of Figure 5.12 (a) shows amphibolites displaying flat patterns with samples showing a positive U anomaly and a less pronounced positive Zr anomaly. The amphibolites are also enriched in LREEs such as La. One amphibolite sample displays a negative Eu anomaly and a depletion in the elements from Sm to Lu. Figure 5.12 (b) is a chondrite-normalized plot that shows an enrichment in LREEs (La to Sm) relative to the HREEs (Gd to Lu) which display a depletion in the amphibolites. There is a subtle negative Eu anomaly. Figure 5.12 (a) and (b) both show relatively flat REE patterns.

5.6 Oxygen isotope geochemistry of quartz in Stolzburg TTGs

Oxygen is the most abundant element in the Earth's crust, and it exists in different isotopic forms, primarily ^{16}O and ^{18}O (Taylor 1968). The ratio of these two isotopes ($\delta^{18}O$) in minerals such as quartz provides information on the conditions of rock formation. Quartz, a robust mineral in TTGs, incorporates oxygen during crystallization, preserving the isotopic signature of the source material and the conditions at the time of formation (Taylor 1968; Lei *et al*., 2023). In fresh TTG samples, this isotopic record reflects the primary source of the magma (Taylor 1968; Lei *et al*., 2023).

The $\delta^{18}O$ values in quartz from TTGs can distinguish between mantle-derived, crustal, or altered sources. Mantle derived magmas typically have a lower $\delta^{18}O$ value of ~5.7 per mil (Ito *et al*., 1987; Bindeman, 2008). Fresh igneous rocks that record $\delta^{18}O$ values higher than mantle values have likely undergone crustal contamination in their magma source (Abraham *et al*., 2011; Faure and Harris (1991). It is important to determine the petrogenetic origin of the quartz in TTGs to understand crustal evolution as quartz is the major mineral in TTGs. The $\delta^{18}O$ signature of quartz in TTGs is a potential way of investigating how the Archean continental crust formed (Smith and Pell, 1997).

5.6.1 Analytical Methods for oxygen isotope analyses of quartz.

The methods used for the determination of the oxygen isotope composition of quartz in granitoid rocks is described in detail in Harris and Vogeli (2010) and is only briefly described here. The fresh tonalite or trondhjemite sample material was disaggregated using a small stainless steel crusher. Quartz grains were selected using tweezers under the microscope. Material was cleaned in ethanol and dried before oxygen isotope analysis. All oxygen isotope data were obtained by Prof. Chris Harris using facilities at the University of Cape Town (UCT).

The laser system uses a 20 W New Wave CO_2 laser, mounted on a moveable stage. For laser fluorination, approximately 1 to 3 mg of quartz was analysed (between 1 and 5 grains). The laser fluorination method used ClF_3. Ten samples and two standards were loaded into a highly polished pure Ni sample holder. All O-isotope ratios were measured off-line using a Finnegan DeltaXP mass spectrometer, in dual inlet mode. All data are reported in the familiar δ notation, where $\delta^{18}O = (R_{sample}/R_{standard} - 1)*1000$ and $R = {}^{18}O/{}^{16}O$, and SMOW is the standard. For laser analysis, O-isotope ratios were measured on O_2 gas. The isotope composition of the O_2 reference gas was determined by converting an aliquot of O_2 to CO_2 using the carbon convertor on the conventional extraction line. This value was used to calculate raw δ values of each sample relative to the SMOW scale. The long-term analytical precision is 0.16‰ (2σ) based on 393 duplicate analyses of MON GT (see Harris and Vogeli, 2010).

5.6.2 The $\delta^{18}O$ values of quartz in Stolzburg TTG samples.

Table 5.3 below lists the oxygen isotope $\delta^{18}O$ quartz values of the TTG samples obtained in this study. There are $\delta^{18}O$ values of quartz for 4 out of 8 fine- to medium-grained tonalite samples, 5 out of 6 coarse-grained trondhjemite samples and for all 3 of the felsic granodiorite sheet samples that were collected at Crusher's quarry.

Table 5.3: *$\delta^{18}O$ quartz values of TTGs from Crusher's quarry, Barberton. The 2-sigma error bar for each $\delta^{18}O$ of quartz value is 0.3 per mil.*

Rock type	**Sample name**	**$\delta^{18}O$ (‰)**
Fine to medium-grained tonalite	CT 1	9.56
	CT 7	9.16
	CT 12	9.13
	CT 17	9.71

Average		**9.39**
Standard deviation		**0.29**
Coarse-grained trondhjemite	CT 6	9.39
	CT 9	8.72
	CT 16	9.43
	CT 20	9.09
	CT 21	9.3
Average		**9.19**
Standard deviation		**0.29**
Felsic sheets	CT 2	9.25
	CT 3	8.96
	CT 8	8.91
Average		**9.04**
Standard deviation		**0.18**

In Table 5.3, fine to medium-grained tonalites have $\delta^{18}O$ quartz values that range from 9.13 to 9.71‰ with the average quartz $\delta^{18}O$ and standard deviation for this rock type being 9.39‰ and 0.29 respectively. Coarse-grained trondhjemites have $\delta^{18}O$ quartz values ranging from 8.72 to 9.43‰ with an average of 9.19 ‰ and standard deviation of 0.29. Felsic sheet samples have $\delta^{18}O$ quartz values ranging from 8.91 to 9.25‰, averaging 9.04‰, with a standard deviation of 0.18. The range in $\delta^{18}O$ values for each of the 3 groups is slightly larger than the 2-sigma variation on the MONGT standard, and the average for the 3 groups has a range of only 0.35 per mil. Hence, the quartz $\delta^{18}O$ values across all rock types is close to being constant.

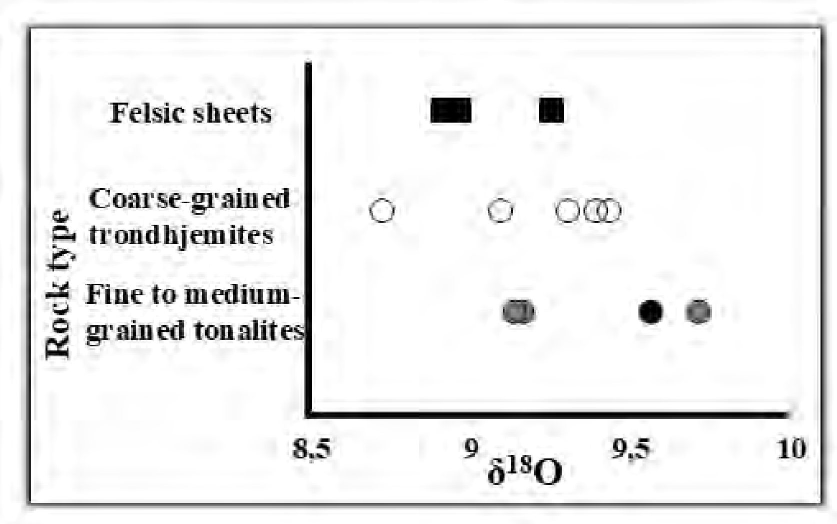

Figure 5.18: *Plot showing the range of $\delta^{18}O$ quartz values for fine to medium-grained tonalites, coarse-grained trondhjemites and felsic sheets. The 2-sigma error bar for each $\delta^{18}O$ of quartz value is 0.3 per mil.*

The rock types on Figure 5.12 all have narrow ranges of $\delta^{18}O$ quartz values. Felsic granodiorite sheets have the narrowest range in $\delta^{18}O$ quartz values, whereas the coarse-grained trondhjemites have the widest range of $\delta^{18}O$ quartz values. The plot in Figure 5.12 is a visual representation of how the $\delta^{18}O$ quartz values overlap between ~8.72 and ~9.56 ‰ across all the rock types. All the $\delta^{18}O$ quartz values for the various TTG samples are within error of each other.

Quartz $\delta^{18}O$ values measured on TTG rocks from the Barberton greenstone belt are scarce in the literature. Using a similar analytical method, Faure and Harris (1991) report an average $\delta^{18}O$ quartz value of 9.7‰ (± 0.3‰) for the 3.23 Ga Kaap Valley tonalite pluton in the north-western part of the belt. The $\delta^{18}O$ quartz values reported herein are very similar to that of the Kaap Valley pluton. Further discussion on this comparison will be given in the Discussion and Interpretation section of this thesis.

6 ZIRCON GEOCHRONOLOGY

6.1 U-Pb zircon geochronology analytical methods

The U-Pb zircon analyses was performed by Mrs Riana Rossouw, CAF, University of Stellenbosch. The zircons from samples CT17 a medium-grained tonalite and CT20, a coarse-grained trondhjemite were mounted in 1-inch epoxy mounts and polished. The U-Pb dating of zircons was conducted by laser ablation ICPMS using a Thermo Element 2 SF ICP-MS instrument and an Applied Spectra Resolution 193nm ArF laser at the Central Analytical Facility, Stellenbosch University. The laser was run in static spot ablation mode with a wavelength of 193 nm and a pulse width of 4 ns. The repetition rate was 8 Hz, the ablation duration 18 seconds and the spot diameter was 25 µm. The carrier gas was 100% Helium (He) in the cell, mixed with Ar and N_2 in the funnel before transport to the ICP. The calibration strategy involved using GJ1 (609 Ma, Jackson *et al*., 2004); as primary reference material, with Plešovice (337 Ma, Sláma *et al*., 2008) and 91500 (1065 Ma $^{207}Pb/^{206}Pb$ age, Wiedenbeck 1995) used as secondary validation standards. Iolite software was used for data normalization, uncertainty propagation. Age calculations were done using Isoplot (Ludwig, 1988). In terms of uncertainty, ages are quoted at 2 sigma absolute. The data was screened for high common Pb in zircon.

6.2 U-Pb zircon geochronology Results

The measured U-Pb isotope zircon analysis spot data is shown in Tables 6.1 for sample CT20 accompanied by zircon backscatter BSE images which show locations of spot analysis.

Table 6.1. *Sample CT20 zircon spot analysis data*

CT20 zircons	**$^{207}Pb/^{235}U$**	**$^{207}Pb/^{235}U$**	**$^{206}Pb/^{238}U$**	**$^{206}Pb/^{238}U$**	**$^{207}Pb/\_^{206}Pb$**	**$^{207}Pb/\_^{206}Pb$**
CT-20_89 – 1	3172	17	2739	49	3457	16
CT-20_90 – 1	2622	26	2122	40	3042	23
CT-20_92 – 1	3467	25	3476	81	3468	22
CT-20_93 – 1	3292	33	2835	54	3588	24
CT-20_94 – 1	3558	14	3715	41	3464	10
CT-20_95 – 1	3419	12	3428	35	3411	9,8
CT-20_96 – 1	3267	22	3080	54	3392	15
CT-20_97 – 1	2198	11	1031	22	3591	33
CT-20_99 – 1	3747	27	3174	91	4076	23
CT-20_100 – 1	3255	16	3092	34	3358	13
CT-20_101 – 1	2885	37	2540	66	3146	20
CT-20_102 – 1	1402	22	835	21	2418	17
CT-20_103 – 1	3353	14	3112	49	3502	17
CT-20_104 – 1	3072	26	2549	62	3445	19

Table 6.1 *(cont).*

CT-20_105 – 1	3493	16	3642	48	3402	16
CT-20_107 – 1	3381	24	3378	70	3390	28
CT-20_108 – 1	3318	14	3174	43	3411	15
CT-20_109 – 1	2499	37	1255	50	3587	35
CT-20_113 – 1	2541	37	1988	53	3033	20
CT-20_116 – 1	2911	20	2310	43	3358	16
CT-20_118 – 1	2138	32	1409	42	2945	26
CT-20_119 – 1	3304	13	3117	34	3421	10
CT-20_120 – 1	3214	31	3067	98	3315	38
CT-20_122 – 1	3384	73	2220	120	4168	47
CT-20_124 – 1	3074	57	2610	120	3427	18
CT-20_128 – 1	3098	19	2834	46	3282	15
CT-20_131 – 1	2729	38	1794	87	3525	33
CT-20_132 – 1	3125	15	2674	39	3431	14
CT-20_134 – 1	3353	15	3229	44	3433	13
CT-20_136 – 1	3161	31	2802	77	3404	24
CT-20_138 – 1	3416	13	3418	41	3413	12
CT-20_139 – 1	3351	14	2660	65	3809	41
CT-20_140 – 1	3463	12	3139	35	3656	13
CT-20_142 – 1	3223	28	2933	78	3418	28

Table 6.1 *(cont)*.

CT-20_143 – 1	3437	26	3483	78	3417	25
CT-20_144 – 1	2302	39	1428	52	3215	16
CT-20_152 – 1	3327	16	3213	48	3390	14
CT-20_159 – 1	3093	14	2695	35	3353	15
CT-20_160 – 1	3435	14	3436	45	3441	13
CT-20_166 – 1	2852	34	2354	61	3233	28
CT-20_167 – 1	3453	17	3455	65	3458	24
CT-20_169 – 1	2707	35	1546	66	3572	31
CT-20_170 – 1	2887	21	2458	50	3210	23
CT-20_174 – 1	2829	19	2126	40	3374	15
CT-20_175 – 1	3400	12	3358	38	3430	13
CT-20_176 – 1	3333	25	3179	80	3434	24
CT-20_177 – 1	2522	22	1623	27	3363	14
CT-20_178 – 1	3627	17	4054	66	3392	19
CT-20_179 – 1	3264	18	2845	49	3536	19
CT-20_180 – 1	3286	39	2930	110	3519	27
CT-20_185 – 1	3490	20	3211	48	3659	18
CT-20_186 – 1	3423	14	3421	43	3433	15
CT-20_190 – 1	3320	36	3210	96	3394	29
CT-20_191 – 1	2550	14	1989	25	3016	13

Table 6.1 *(cont)*.

CT-20_192 – 1	2267	19	1112	20	3572	17
CT-20_193 – 1	2514	24	1219	36	3817	18

The cores of zircons from sample CT20 were analyzed, and fractured areas of the zircons were mostly avoided. Sample CT-20 zircon grains show various degrees of zoning and preservation thus reflecting various stages of crystallization. Most of the zircon grains exhibit well defined concentric zoning which is interrupted by fractures. The fractures are indicative of mechanical deformation. Faint zoning can be seen towards the rims of some of the grains which suggests that these grains initially went through steady magmatic growth which was later followed by slow crystal growth and alteration. Zoning patterns are disrupted by fractures that run through the core and rim, possibly erasing the original zoning pattern of the grain. The bright luminescent areas on the zircon grains suggests zones with high uranium concentrations which are susceptible to radiation damage.

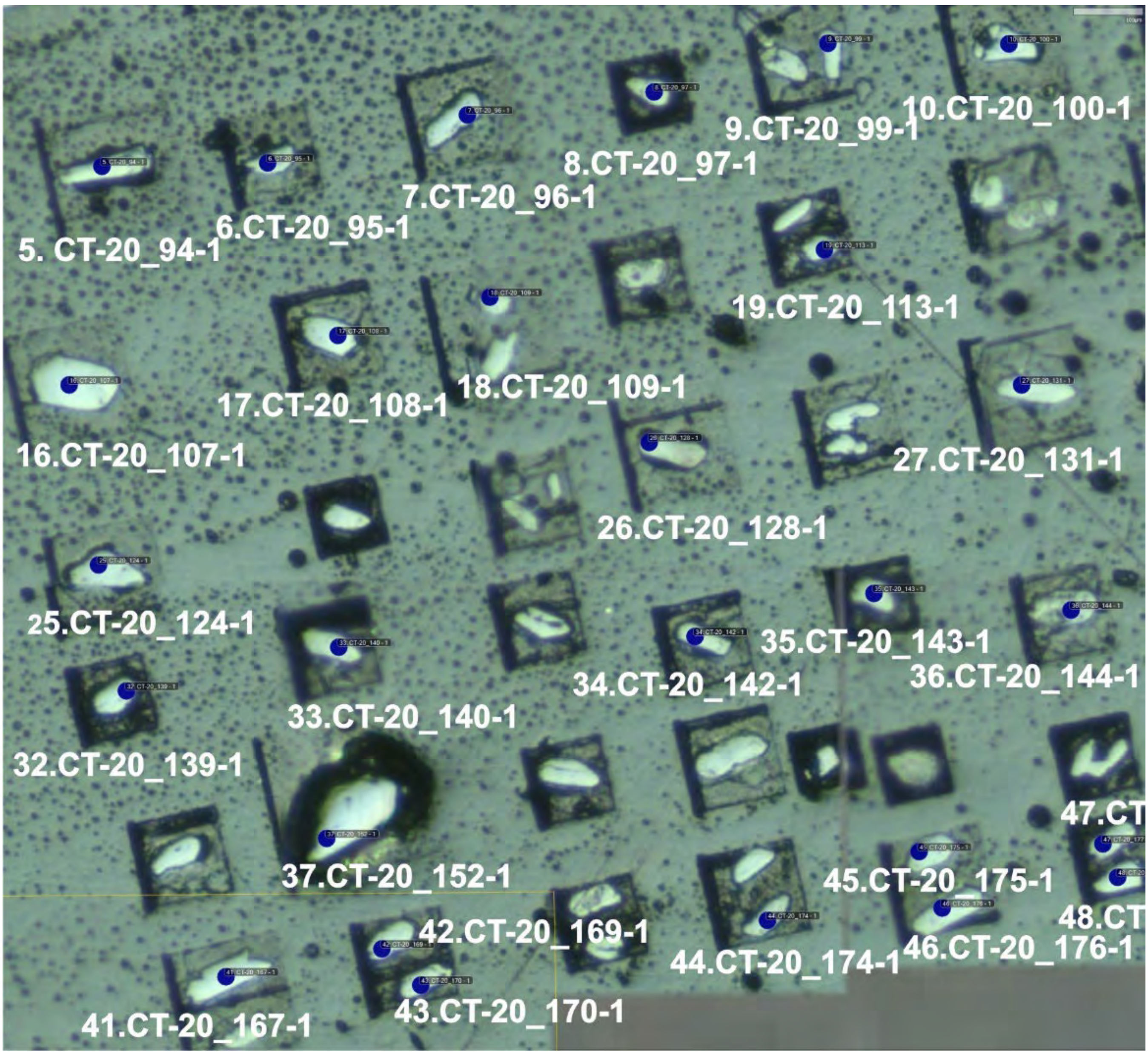

Figure 6.1. Selected zircon backscatter BSE images for sample CT20 showing locations of spot analysis.

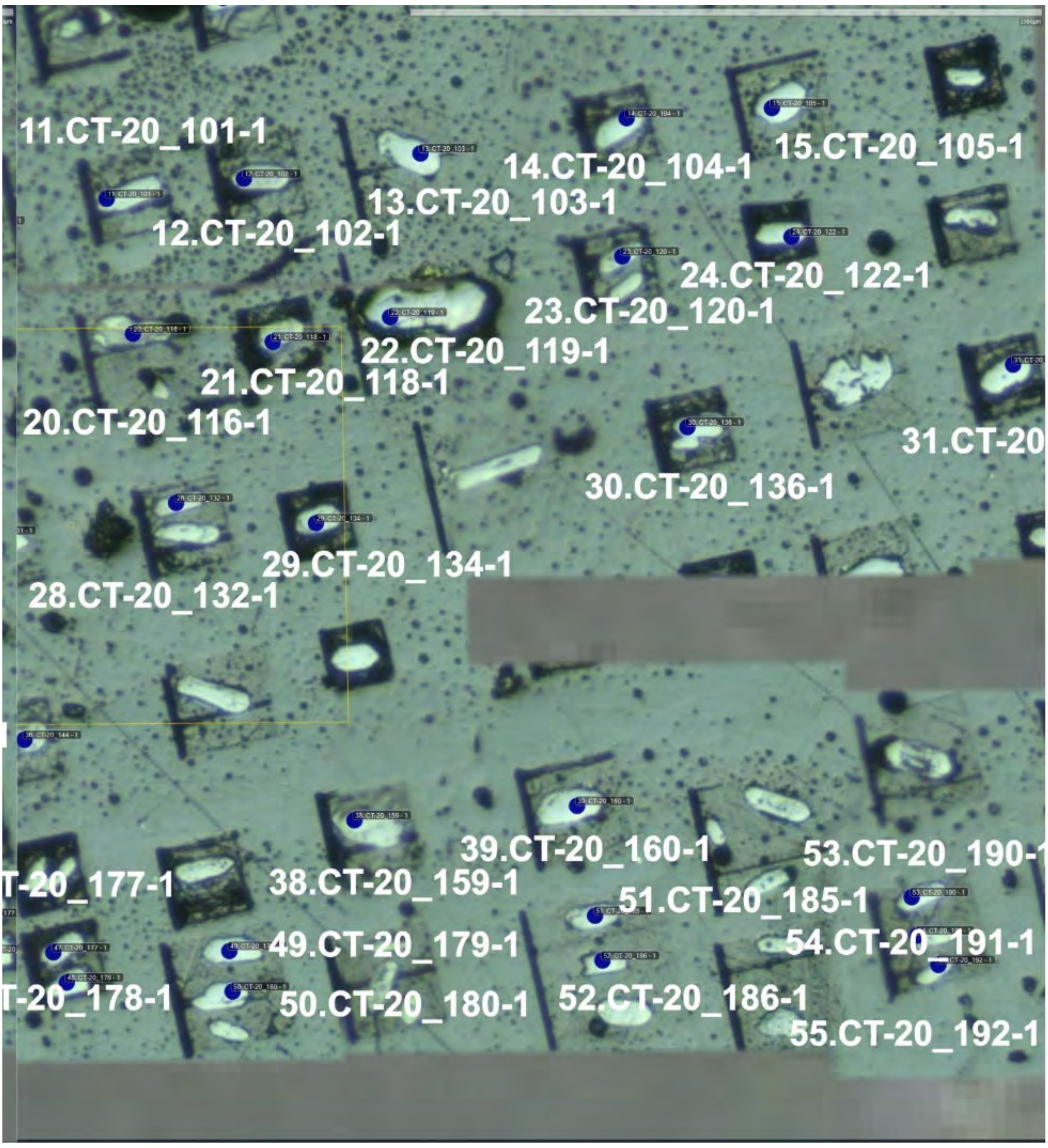

Figure 6.1. *(continued).*

Sample CT17 zircon spot analysis data and selected zircon backscatter BSE images for sample CT17 showing locations of spot analysis are in Appendix D.

6.3 U-Pb zircon geochronology Results

The measured U-Pb isotope ratios and calculated ages are shown in Tables 6.2 for sample CT17 and Table 6.3 for sample CT20.

Table 6.2: *$^{207}Pb/^{235}U$, $^{206}Pb/^{238}U$, $^{207}Pb/^{206}Pb$ isotope data for sample CT17 a medium-grained tonalite of the Stolzburg Pluton, Barberton.*

Isotopic ratios							Calculated ages (Ma)					
$^{207}Pb/^{235}U$	± 2 sigma	$^{206}Pb/^{238}U$	± 2 sigma	Rho	$^{207}Pb/^{206}Pb$	± 2 sigma	$^{207}Pb/^{235}U$	± 2 sigma	$^{206}Pb/^{238}U$	± 2 sigma	$^{207}Pb/^{206}Pb$	± 2 sigma
7,8900	0,1900	0,3069	0,0060	0,0316	0,1874	0,0029	2216	21	1724	30	2716	25
15,1600	0,4300	0,4680	0,0110	0,0256	0,2336	0,0025	2811	27	2468	48	3072	17
26,5600	0,7300	0,6540	0,0230	0,0315	0,2962	0,0044	3365	27	3239	88	3449	23
28,4300	0,4300	0,7050	0,0130	0,0302	0,2941	0,0030	3432	15	3437	47	3437	16
12,0200	0,1800	0,3951	0,0076	0,0422	0,2210	0,0027	2604	14	2145	35	2985	19
5,7560	0,0780	0,2572	0,0037	0,0474	0,1629	0,0012	1938	12	1475	19	2484	13
7,4500	0,1100	0,2989	0,0044	0,0400	0,1805	0,0018	2166	14	1685	22	2654	16
3,9310	0,0510	0,1930	0,0026	0,0510	0,1475	0,0011	1618	11	1137	14	2316	13
27,5100	0,3000	0,6761	0,0084	0,0280	0,2954	0,0022	3401	10	3326	32	3444	11
6,7100	0,1100	0,2528	0,0057	0,0518	0,1943	0,0024	2076	15	1452	29	2777	21
17,6300	0,2700	0,5263	0,0085	0,0315	0,2427	0,0019	2967	15	2723	36	3136	12
7,8400	0,1500	0,3201	0,0064	0,0427	0,1768	0,0019	2211	18	1789	31	2621	18
7,7300	0,1800	0,3014	0,0071	0,0394	0,1864	0,0014	2196	21	1696	35	2709	13
11,1900	0,3600	0,3870	0,0120	0,0333	0,2103	0,0038	2537	31	2108	57	2906	29
27,9300	0,3700	0,6988	0,0094	0,0254	0,2887	0,0020	3413	13	3412	35	3408	11
10,5200	0,2600	0,3549	0,0084	0,0323	0,2149	0,0027	2478	23	1956	40	2940	20
23,6500	0,5100	0,5870	0,0160	0,0314	0,2938	0,0047	3252	21	2975	64	3435	24
12,0200	0,1700	0,3899	0,0053	0,0312	0,2233	0,0019	2604	13	2124	25	3001	14
7,1100	0,1400	0,2748	0,0057	0,0407	0,1883	0,0013	2121	18	1563	29	2726	11

Table 6.2 *(cont).*

27,5500	0,7200	0,6670	0,0210	0,0292	0,3017	0,0039	3398	26	3287	80	3476	20
5,6600	0,1100	0,2447	0,0043	0,0391	0,1677	0,0014	1923	17	1410	22	2531	14
12,1400	0,1800	0,4071	0,0053	0,0294	0,2166	0,0019	2611	14	2200	24	2952	14
6,2600	0,1900	0,2544	0,0056	0,0295	0,1767	0,0021	2004	25	1459	29	2617	19
16,0800	0,3800	0,4770	0,0130	0,0342	0,2457	0,0035	2879	22	2514	57	3155	22
6,6560	0,0990	0,2675	0,0041	0,0414	0,1802	0,0014	2063	13	1527	21	2652	13
10,7500	0,2400	0,3558	0,0090	0,0375	0,2206	0,0040	2500	20	1961	43	2981	30
27,7300	0,3400	0,6954	0,0096	0,0282	0,2886	0,0023	3407	12	3400	37	3409	13
10,0600	0,2600	0,3615	0,0075	0,0288	0,2002	0,0023	2433	24	1987	35	2824	19
24,4200	0,3400	0,6450	0,0110	0,0324	0,2761	0,0024	3283	14	3204	42	3339	14
13,2600	0,1800	0,3933	0,0065	0,0361	0,2463	0,0018	2700	13	2135	30	3160	12
27,1400	0,5600	0,6920	0,0130	0,0232	0,2841	0,0031	3384	20	3387	51	3383	17
24,2300	0,4300	0,6230	0,0100	0,0233	0,2822	0,0023	3272	17	3115	42	3374	13
23,0200	0,6600	0,6170	0,0150	0,0227	0,2691	0,0025	3212	30	3090	59	3297	15
25,4900	0,5400	0,6160	0,0160	0,0296	0,3022	0,0045	3326	20	3090	63	3479	23
17,1000	0,2200	0,4770	0,0069	0,0314	0,2600	0,0018	2939	12	2512	30	3245	11
4,8800	0,1500	0,2191	0,0074	0,0493	0,1622	0,0026	1796	25	1277	39	2477	26
21,0100	0,3600	0,5410	0,0110	0,0306	0,2821	0,0030	3134	17	2788	45	3370	17
25,7300	0,3600	0,6560	0,0100	0,0278	0,2855	0,0023	3333	14	3245	40	3390	13
12,3700	0,2900	0,3905	0,0077	0,0266	0,2290	0,0023	2627	22	2121	35	3041	16
18,9600	0,3800	0,5390	0,0100	0,0263	0,2584	0,0028	3040	20	2778	43	3235	17
11,1100	0,1600	0,3802	0,0050	0,0313	0,2118	0,0018	2529	14	2079	24	2918	13
21,6900	0,4900	0,5760	0,0160	0,0327	0,2749	0,0040	3167	22	2930	66	3332	22
18,9100	0,4400	0,5230	0,0120	0,0273	0,2651	0,0033	3034	22	2710	52	3275	19
7,5100	0,1000	0,2896	0,0043	0,0430	0,1880	0,0015	2171	13	1638	21	2724	13
14,7800	0,5100	0,4130	0,0130	0,0255	0,2577	0,0029	2797	33	2237	58	3230	18
12,9400	0,2100	0,4236	0,0081	0,0386	0,2231	0,0024	2673	15	2275	37	3001	17
18,0000	1,0000	0,5010	0,0210	0,0210	0,2601	0,0066	2976	59	2614	93	3243	41
16,2900	0,2700	0,4635	0,0088	0,0326	0,2552	0,0019	2893	17	2451	39	3215	12

Table 6.2 *(cont).*

7,2400	0,1400	0,2836	0,0039	0,0279	0,1855	0,0023	2136	17	1608	19	2697	21
15,6400	0,4600	0,4640	0,0110	0,0239	0,2451	0,0032	2848	27	2453	49	3154	21

Table 6.3: *$^{207}Pb/^{235}U$, $^{206}Pb/^{238}U$, $^{207}Pb/^{206}Pb$ isotope data for sample CT20 a coarse-grained trondhjemite of the Stolzburg Pluton, Barberton.*

Isotopic ratios							Calculated ages (Ma)					
$^{207}Pb/^{235}U$	± 2 sigma	$^{206}Pb/^{238}U$	± 2 sigma	Rho	$^{207}Pb/^{206}Pb$	± 2 sigma	$^{207}Pb/^{235}U$	± 2 sigma	$^{206}Pb/^{238}U$	± 2 sigma	$^{207}Pb/^{206}Pb$	± 2 sigma
21,7900	0,3800	0,5300	0,0120	0,0316	0,2980	0,0030	3172	17	2739	49	3457	16
12,3000	0,3300	0,3886	0,0090	0,0273	0,2291	0,0033	2622	26	2122	40	3042	23
29,4800	0,7700	0,7160	0,0220	0,0286	0,2999	0,0041	3467	25	3476	81	3468	22
32,3300	0,4500	0,7810	0,0110	0,0244	0,2990	0,0019	3558	14	3715	41	3464	10
28,0600	0,3300	0,7030	0,0092	0,0279	0,2891	0,0018	3419	12	3428	35	3411	9,8
24,0800	0,5500	0,6130	0,0140	0,0255	0,2857	0,0027	3267	22	3080	54	3392	15
23,7800	0,3800	0,6163	0,0086	0,0226	0,2794	0,0024	3255	16	3092	34	3358	13
16,5400	0,5900	0,4860	0,0150	0,0254	0,2448	0,0029	2885	37	2540	66	3146	20
2,9910	0,0840	0,1385	0,0037	0,0440	0,1567	0,0016	1402	22	835	21	2418	17
26,1900	0,3900	0,6210	0,0120	0,0308	0,3064	0,0033	3353	14	3112	49	3502	17
19,6000	0,4900	0,4860	0,0140	0,0286	0,2956	0,0036	3072	26	2549	62	3445	19
30,2300	0,4900	0,7600	0,0130	0,0265	0,2875	0,0029	3493	16	3642	48	3402	16
25,3100	0,3700	0,6370	0,0110	0,0297	0,2893	0,0028	3318	14	3174	43	3411	15
11,4300	0,4300	0,3620	0,0110	0,0256	0,2280	0,0028	2541	37	1988	53	3033	20
16,6400	0,3500	0,4314	0,0095	0,0271	0,2796	0,0028	2911	20	2310	43	3358	16
7,2500	0,2700	0,2446	0,0082	0,0304	0,2156	0,0035	2138	32	1409	42	2945	26
24,9600	0,3300	0,6225	0,0087	0,0264	0,2909	0,0020	3304	13	3117	34	3421	10
20,3000	1,2000	0,5040	0,0280	0,0233	0,2923	0,0034	3074	57	2610	120	3427	18

Table 6.3 *(cont).*

20,2300	0,4000	0,5510	0,0110	0,0275	0,2663	0,0025	3098	19	2834	46	3282	15
20,8000	0,3100	0,5153	0,0092	0,0297	0,2932	0,0026	3125	15	2674	39	3431	14
26,2200	0,4200	0,6510	0,0110	0,0262	0,2932	0,0024	3353	15	3229	44	3433	13
21,5600	0,6800	0,5450	0,0180	0,0265	0,2877	0,0044	3161	31	2802	77	3404	24
27,9300	0,3600	0,6990	0,0110	0,0306	0,2895	0,0023	3416	13	3418	41	3413	12
22,9700	0,6600	0,5770	0,0190	0,0288	0,2905	0,0053	3223	28	2933	78	3418	28
28,6000	0,7500	0,7180	0,0210	0,0280	0,2904	0,0046	3437	26	3483	78	3417	25
8,7900	0,3800	0,2490	0,0100	0,0263	0,2553	0,0027	2302	39	1428	52	3215	16
25,4900	0,4000	0,6470	0,0120	0,0300	0,2854	0,0026	3327	16	3213	48	3390	14
20,0700	0,3000	0,5195	0,0083	0,0277	0,2782	0,0026	3093	14	2695	35	3353	15
28,5100	0,4100	0,7050	0,0120	0,0293	0,2948	0,0025	3435	14	3436	45	3441	13
15,6600	0,5400	0,4410	0,0130	0,0241	0,2583	0,0046	2852	34	2354	61	3233	28
29,0200	0,5100	0,7100	0,0170	0,0333	0,2981	0,0046	3453	17	3455	65	3458	24
16,2300	0,3700	0,4650	0,0110	0,0297	0,2546	0,0038	2887	21	2458	50	3210	23
15,2700	0,3000	0,3912	0,0088	0,0293	0,2824	0,0027	2829	19	2126	40	3374	15
27,5000	0,3200	0,6843	0,0099	0,0309	0,2927	0,0024	3400	12	3358	38	3430	13
25,7000	0,6600	0,6380	0,0200	0,0303	0,2935	0,0045	3333	25	3179	80	3434	24
11,0900	0,2400	0,2867	0,0053	0,0221	0,2806	0,0025	2522	22	1623	27	3363	14
34,6700	0,5800	0,8730	0,0180	0,0310	0,2858	0,0035	3627	17	4054	66	3392	19
24,0300	0,4300	0,5570	0,0120	0,0279	0,3142	0,0038	3264	18	2845	49	3536	19
24,4900	0,9700	0,5760	0,0270	0,0278	0,3099	0,0053	3286	39	2930	110	3519	27
28,0900	0,4300	0,7010	0,0110	0,0256	0,2933	0,0028	3423	14	3421	43	3433	15
11,3100	0,1700	0,3619	0,0054	0,0318	0,2253	0,0018	2550	14	1989	25	3016	13

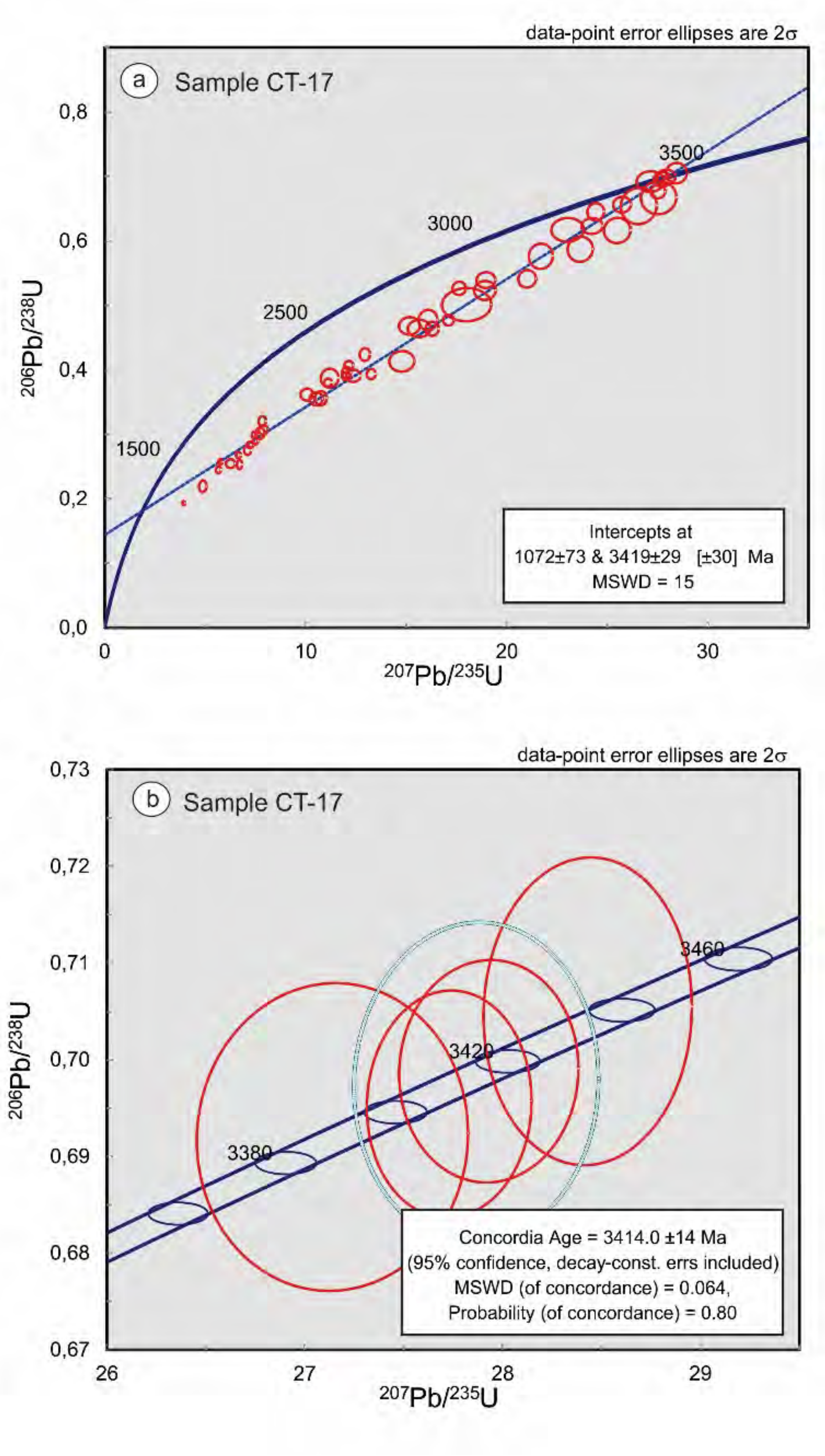

Figure 6.2: (a) *U-Pb Concordia plot showing an upper intercept age of 3419 ± 29 Ma in sample CT17 and (b) enlarged Concordia plot for selected concordant zircon grains showing the Concordia age of sample CT17 of the Stolzburg pluton, Barberton. All uncertainties at the 2σ level.*

For sample CT17 a medium-grained tonalite, both the $^{206}Pb/^{238}U$ and $^{207}Pb/^{235}U$ ratios are regressed to yield an upper intercept age that plots on the Concordia curve shown in Fig 6.2 (a). The data yields an upper intercept ages of 3419 ± 29 Ma and a lower intercept age of 1072 ± 73 Ma. The upper intercept is taken as the initial crystallization age. Four zircon grains that are very concordant give a mean age of 3414 ± 14 Ma (Figure 6.2b).

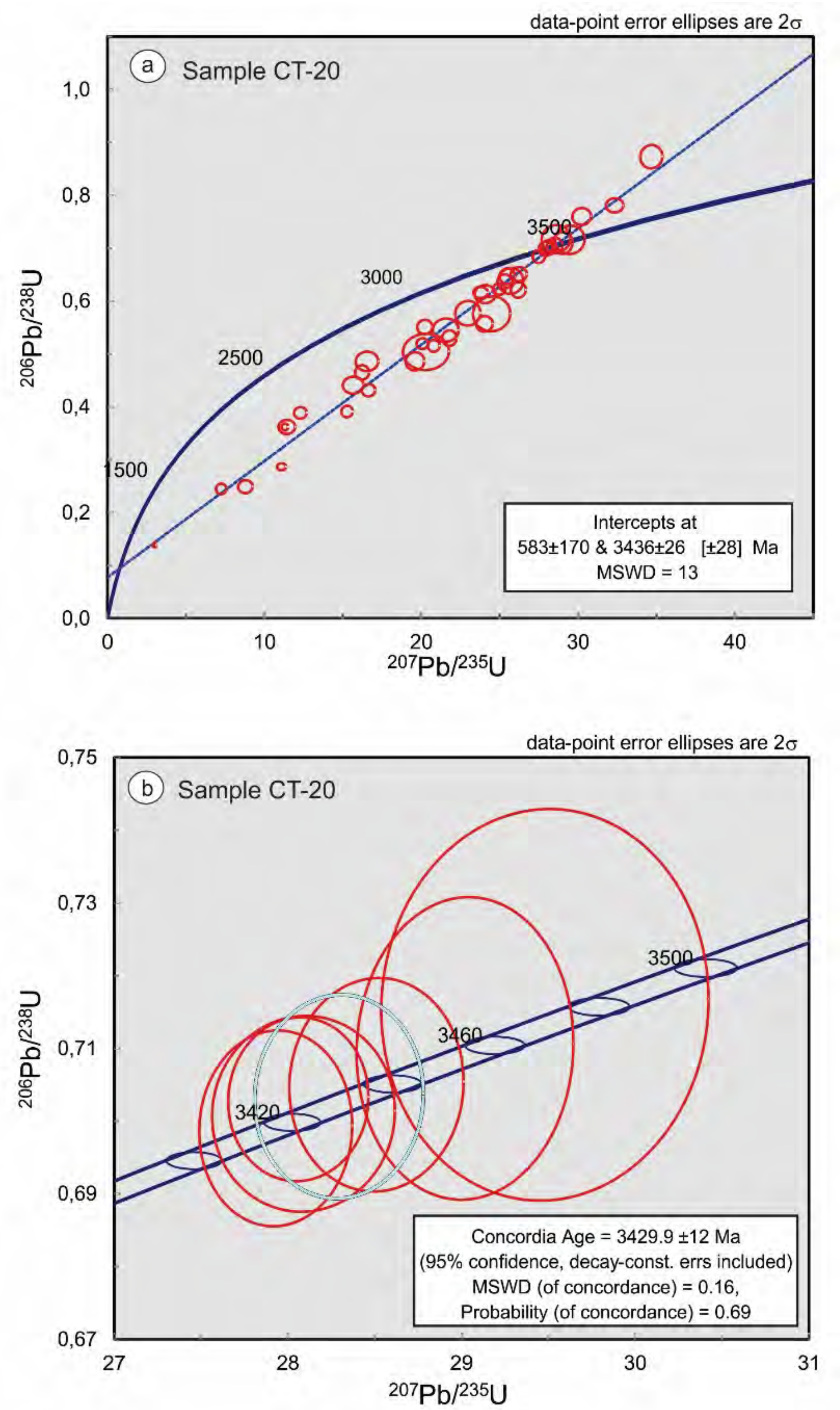

Figure 6.3: (a)*U-Pb Concordia plot showing an upper intercept age of 3436 ± 26 Ma in sample CT20 and (b) enlarged Concordia plot for six selected concordant zircon grains showing the Concordia age of sample CT20 of the Stolzburg pluton, Barberton. All uncertainties at the 2σ level.*

For sample CT20, a coarse-grained trondhjemite the $^{206}Pb/^{238}U$ and $^{207}Pb/^{235}U$ ratios are regressed to yield an upper intercept age that plots on the Concordia curve shown in Fig 6.3 (a) below. The diagram shows an upper intercept age of 3436 ± 26 Ma (Figure 6.3a) and a lower intercept age of 583 ± 170 Ma Six zircon grains that are very concordant give a mean age of 3429.9 ± 12 Ma (Figure 6.3b).

While lower intercept ages were known to represent the onset of metamorphism or the timing of thermal events in rocks (Wetherill, 1956), the lower intercept ages of samples CT17 and CT20 of this study show significant variability. This discrepancy raises questions as the rocks exhibit similar Concordia ages. The study of Kramers *et al*, (2009) may explain why there is such a big gap between the lower intercepts. In zircons, radiogenic Pb is predominantly in the Pb^{2+} state, which is more mobile than Pb^{4+}, meaning it can more easily migrate out of the zircon under certain conditions (Kramers *et al*., 2009). This mobility is influenced by factors such as radiation damage, temperature, and fluid interactions. As a result, Pb loss is not always a simple, single-event process but can occur over extended periods or in multiple episodes (Kramers *et al*., 2009).

Pb loss may occur gradually over time in zircons that have experienced prolonged thermal disturbances or radiation damage (Kramers *et al*., 2009). This can result in a lower intercept age that does not correspond to a specific metamorphic event but rather reflects an average of continuous Pb loss over a range of temperatures (Kramers *et al*., 2009). Hydrothermal or metamorphic fluids can interact with zircon crystals, leaching out Pb and other elements (Kramers *et al*., 2009). This process is highly selective and can preferentially remove Pb^{2+} due to its mobility (Kramers *et al*., 2009; Hansen and Friderichsen, 1989). Leaching can occur during metamorphism, but it can also happen during later fluid-rock interactions unrelated to the metamorphic event (Kramers *et al*., 2009). If Pb loss is caused by leaching, the lower intercept age may not reflect the timing of metamorphism but rather the timing of fluid activity (Kramers *et al*., 2009).

The upper intercept ages of samples CT17 and CT20 are within error of each other. The upper intercept ages are in agreement with the published age range of 3437-3455 Ma for the Stolzburg pluton (Kamo and Davis, 1994).

The mean ages for the Concordant grains are more precise for both samples. The Concordant age of 3414 ± 14 Ma for sample CT17 is younger that the published Stolzburg Pluton ages whereas the Concordant age of 3429.9 ± 12 Ma for sample CT20 falls within error of the published Stolzburg Pluton ages (Table 6.3), which range from 3437 Ma to 3455 Ma. The published Stolzburg Pluton ages were obtained from different methods of dating other than Laser Ablation ICP-MS used in this study.

Table 6.3. *A summary of the estimated age of the Stolzburg Pluton based on different studies.*

	Muhlberg (2022)	**Kamo and Davis (1994)**	**Dziggel *et al*. (2002; 2005)**	**Schoene *et al*. (2008)**	**Armstrong *et al*., (1991)**
Method of dating	Single zircon evaporation age	Single zircon evaporation age	Ion microprobe	U-Pb ID-TIMS	Single zircon ion microprobe
Age in Ma	ca. 3450-3400	ca. 3437-3448	3455 ± 6	3455.5 ± 0.6	ca. 3437-3448
Uncertainties	Concordia age at 2σ	Not specified	Not specified	Concordia age	Concordia age at 2σ

The method of dating used in this study is Laser Ablation ICP-MS, which is different from the methods of dating used in other studies (Table 6.3). The following paragraphs will delve into the limitations of Laser Ablation, which could possibly explain the younger sample CT17 age.

Laser ablation can cause elemental and isotopic fractionation, where certain elements or isotopes are preferentially ablated or ionized compared to others. This can lead to inaccuracies in U–Pb age determinations (Jackson *et al*., 2004). Jackson *et al*., 2004 suggest using well-characterized external standards to minimize fractionation effects. Additionally, using a laser with a flat energy profile and optimizing ablation conditions such as spot size can reduce fractionation.

Laser ablation provides good spatial resolution, but this can also be a limitation when analyzing zoned zircons with complex U–Pb distributions (Jackson *et al*., 2004). Combining LA-ICP-MS with imaging techniques to identify and target specific zircon domains could avoid this limitation (Li *et al*., 2001; Horstwood *et al*., 2001).

The presence of common Pb (non-radiogenic Pb) in zircon can significantly affect U–Pb age calculations, leading to inaccurate results. Applying common Pb correction and using highly sensitive instruments can mitigate this. Contamination can introduce mercury (Hg) to the mass spectrometer and this is problematic because Hg interferes with the measurement of Pb isotopes. If Hg is present, it can lead to inaccurate measurements of ^{204}Pb, which in turn affects common Pb correction and the accuracy of the U-Pb age (Kramer *et al*., 1991).

The composition and physical properties of the sample can influence the ablation process, leading to biases in U–Pb measurements (Tiepolo *et al*., 2003; Johnson *et al*., 2004). The authors emphasize the importance of using matrix-matched standards and conducting careful calibration to account for matrix effects (Tiepolo *et al*., 2003).

This MSc study paper highlights that LA-ICP-MS is a powerful tool for U-Pb zircon geochronology, however, it acknowledges that Laser Ablation ICP-MS does have limitations when attempting to dating Archean zircons. These limitations explain why the Stolzburg ages for CT-17 and CT-20 in this study are not entirely accurate, even though they are both older than 3400 Ma.

7 DISCUSSION & INTERPRETATION

7.1 Summary of Data and Interpretation

In this chapter, the characteristics of the tonalite-trondhjemite-granodiorite (TTG) samples which include field geology, petrography, geochemistry, $\delta^{18}O$ of quartz and U-Pb geochronology are summarized and used to address the petrogenesis of Crusher's quarry TTGs and the possible geodynamic setting(s) in which they formed on the early Earth.

7.1.1 Field Geology

Field mapping of six outcrop faces in Crusher's quarry identified five distinct rock types: coarse-grained trondhjemites, medium-grained tonalites, fine-grained tonalites, granodiorite sheets and amphibolite xenoliths (Figure 7.1). Coarse-grained trondhjemites make up ~28% of the quarry, medium-grained tonalites make up ~40%, fine-grained tonalites make up ~18%, amphibolites make up ~6% and felsic veins and granodiorite sheets make up ~8% of the quarry. The cross-cutting relationships between these rock types were studied to construct their timing of emplacement. Figure 7.1.1 summarizes these relationships, illustrating the sequence of intrusion and the spatial distribution of TTGs and amphibolites within the quarry.

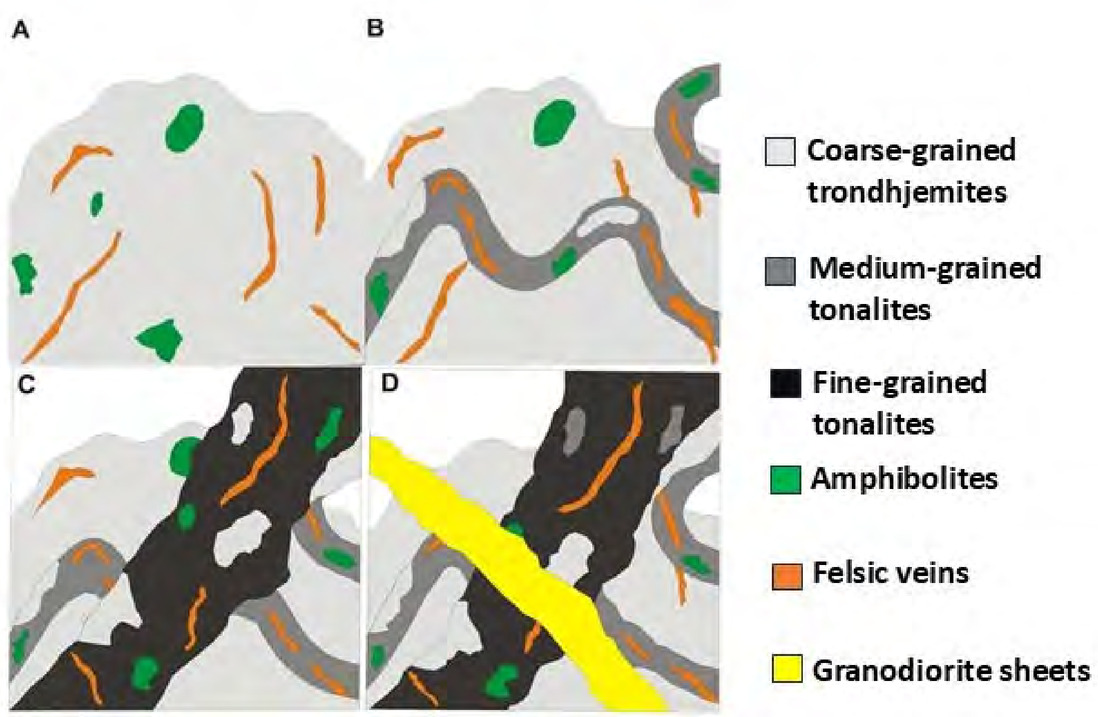

Figure 7.1.1: *A schematic model summarising the crosscutting relationships in Crusher's quarry, derived from field mapping of six outcrop faces. Key lithologies described in legend.*

Coarse-grained trondhjemites are contained as xenoliths in both fine and medium-grained grained tonalites (Figure 7.1.1 (b) (c) and (d)), which suggests that coarse-grained trondhjemites were intruded earlier than the fine and medium-grained tonalites.

Medium-grained tonalites are found to be enveloped in fine-grained tonalites on some faces of the quarry, suggesting that the medium-grained tonalites are older than fine-grained tonalites. Generally, the coarse-grained trondhjemites appear to have intruded first then followed by medium-grained tonalites and then lastly by the fine-grained tonalites.

The trondhjemites and tonalites all contain felsic veins. The felsic veins include several different generations, because they are found in rocks which intruded at separate times. Felsic veins that are contained in the coarse-grained trondhjemites represent the first generation and those contained within the medium and fine-grained tonalites are second and third generation, respectively. Granodiorite sheets cut across every rock type in the quarry which suggests that they were the last phase to intrude.

Amphibolites occur as xenoliths in coarse-grained trondhjemites as well as in fine- and medium-grained tonalites, suggesting that TTGs intruded pre-existing amphibolites and the amphibolites were entrained in each of the magma pulses.

7.1.2 Petrography

TTGs encompass a wide range of rock types with variable mineralogies. TTGs are quartz-rich igneous rocks with plagioclase, k-feldspar (which is proportionally less than the plagioclase), biotite and minor amphibole and accessory minerals such as zircon, apatite, epidote and titanite (Moyen, 2007; Martin *et al*., 2005; Clemens *et al*., 2006). Fine-grained tonalite samples from Crusher’s quarry are made up of quartz, plagioclase, microcline, orthoclase, biotite, hornblende and sphene. Quartz has the highest modal mineralogy of >65 % while hornblende is present in minor proportions and sphene is present as an accessory mineral. Similar to fine-grained tonalites, medium-grained tonalites are composed of >70 % quartz, orthoclase, plagioclase, biotite and accessory hornblende and sphene. Medium-grained tonalite samples from Crushers’ Quarry do not exhibit any microcline. The ferromagnesian minerals biotite and hornblende occur in clusters that are unevenly dispersed in the rock. Sphene grains are present where there is a ferromagnesian mineral cluster.

Coarse-grained trondhjemite samples contain brown biotite and accessory sphene. No amphibole was identified in the coarse-grained trondhjemites. The proportion of mafic minerals decreases from the finer rocks to the coarser rocks.

Grey coloured fine and medium-grained tonalites do not have any mineralogical differences, but rather textural differences exist in terms of the grain sizes. Coarse-grained trondhjemites are mineralogically different from the tonalites in that they do not contain any amphibole i.e., hornblende. This is consistent with observations by Moyen *et al*., (2020) who reported that tonalites can contain hornblende and biotite, whereas trondhjemites contain only biotite with no hornblende. Granodiorite felsic sheets are made up of c. 60 % quartz, c.10 % microcline and c.30 % plagioclase. The amphibolites are composed of c. 80 % hornblende, c. 20 % with minor amounts of, quartz and plagioclase. The amphibolites have a foliated texture which is defined by the hornblende and biotite grains.

7.1.3 Geochemistry

Medium-grained tonalites overlap with fine-grained tonalites but extend to slightly higher SiO_2 values (65-70 wt.%). Coarse-grained trondhjemites plot at even higher SiO_2 values (70-75 wt.%). TiO_2, Al_2O_3, FeOT, MgO, CaO, and P_2O_5 all show negative correlations with SiO_2, decreasing from fine- and medium-grained tonalites to granodiorite sheets. Na_2O displays a scattered distribution but generally decreases slightly with increasing SiO_2 from fine-grained tonalites to granodiorite sheets. K_2O exhibits a positive trend across all rock types, increasing with SiO_2, with granodiorite sheets having the highest K_2O content. L.O.I values show no clear trend with SiO_2 but display a positive correlation with MgO.

Clemens *et al*. (2006) emphasize that the geochemical characteristics of Barberton TTGs, such as high Na_2O, low K_2O, and distinct rare earth element (REE) patterns, are inconsistent with crystal fractionation processes. These features are observed in the Stolzburg pluton TTGs. There is no strong trace element versus SiO_2 relationships on the trace element Harker plots with the exception of Nb, Y and Zn. This suggests that crystal fractionation was not the dominant process in the formation of the Stolzburg TTGs (Clemens *et al.*, 2006). This is because when crystal fractionation occurs, it results in systematic changes in trace element compositions relative to SiO_2 as different minerals crystallize out of the magma. These rocks may be cumulate rocks or not related by simple fractional crystallization.

The concentration of Nb in TTGs is significant in constraining the petrogenesis and geodynamic model of TTGs, because Nb in contrast to other trace elements is minutely affected by early-stage crystal fractionation as it is immobile during such magmatic processes (Pearce and Peate, 1995). The immobility of Nb during the crystallization of common fractionating minerals (e.g. plagioclase, amphibole, pyroxenes) makes it a reliable indicator of tectonic setting and petrogenetic processes. This makes Nb anomalies in TTGs quite informative (Pearce and Peate, 1995; Rollinson, 1993). The Nb concentration in TTGs is also influenced by the source rocks from which the TTGs formed (Clemens *et al.*, 2006; Rollinson, 1993).

Oceanic crust rocks are known to have low Nb (HFSE) concentrations in comparison to the upper mantle (Pearce and Peate, 1995; Woodhead *et al.*, 2011). A negative Nb anomaly is commonly interpreted as evidence of a subduction zone origin (Pearce and Peate, 1995). During subduction, the subducting oceanic slab releases fluids and melts that are rich in large ion lithophile elements (LILEs) but poor in high field strength elements (HFSEs) (Foley *et al.*, 2002; Rapp and Watson, 1995; Pearce and Peate, 1995). This geochemical pattern suggests that TTGs were derived from partial melting of hydrated basaltic rocks (oceanic crust) in a subduction zone setting (Pearce and Peate, 1995; Martin, 1999; Foley *et al.*, 2002). The amphiboles and micas in the melts from the subducted slab selectively mobilize HFSEs (Ta and Nb), but they have strong preference for Ta over Nb due to its slightly smaller ionic radius and higher charge, therefore leaving Nb behind, resulting in its depletion in the melts that eventually form TTGs (Ionov and Hofmann, 1995; Hawkesworth *et al.*, 1984). Nb can be retained in certain residual phases such as rutile or ilmenite, which do not readily melt. This retention creates a relative Nb depletion in the melt, leading to negative Nb anomalies (Foley *et al.*, 2000; Hawkesworth *et al.*, 1984). Therefore, oceanic crust rocks which are low in Nb are possibly a more suitable protolith for the Stolzburg TTGs, which have low Nb concentrations hence the Nb anomalies displayed on Figure 5.8.

Nb anomalies are also exhibited in arc magmas due to the involvement of subduction-related melts that have interacted with amphibole and mica bearing mantle sources. Nb being less mobile in subduction fluids together with the preferential retention of Ta in these minerals during metasomatism and partial melting results in the characteristic depletion of Nb in arc magmas (Ionov and Hofmann, 1995; Hawkesworth *et al.*, 1984).

According to Liou and Guo (2019), tonalite melts form in low pressure settings with lower Sr/Y ratios, whereas trondhjemite melts form in high pressure settings and have high Sr/Y ratios due to the presence of garnet. The TTG data from this study are compatible with Liou and Guo's (2019) findings, because the coarse-grained Stolzburg trondhjemites generally have higher Sr/Y ratios than the fine to medium-grained tonalites. This is evident in Figure 5.7 as the coarse-grained trondhjemites plot on the high-pressure field, whereas the fine to medium-grained tonalites plot on the medium pressure field, and some of the fine to medium-grained tonalites plot on the high and medium pressure field intersection.

TTGs generally fall within the low-K to medium-K fields, whereas granitoids which are associated with post-Archean magmatism fall in the high-K series. The K_2O and SiO_2 discriminant diagram shown in Figure 5.4b therefore help differentiate TTGs from high-K granitoids which have a different origin from TTGs and it also helps infer the tectonic setting and depth of TTG formation. It classifies the Crushers' Quarry rocks as true TTGs, because the tonalites and trondhjemite samples plot within the true TTG field/ medium K series field, with the exception, of one coarse and one medium-grained outliers that plot on the high K series. Plotting within the low and medium-K domains aligns with the composition typical of Archean TTG suites. A few samples, such as the felsic sheets, plot within the High-K series, which may suggest contamination from potassic-rich sources (Davis *et al.*, 1993; Reimink and Smye, 2014). The samples analyzed in this study plot within the peraluminous field on Figure 5.13, as defined by the A/CNK ratio, indicating a strong signature of crustal contamination of a basaltic melt with ancient intermediate TTG crust and sediments (e.g. Reimink and Smye, 2024).

The normative ternary diagram on Figure 5.5 further classifies the coarse-grained samples as trondhjemites, the fine and medium-grained samples as tonalites, and the felsic sheets as granodiorites. The clustering of tonalites and trondhjemites within the tonalite and trondhjemite fields aligns with the characteristics of Archean TTG suites. The presence of felsic sheets with higher orthoclase content suggests late-stage magmatic differentiation or assimilation of potassium-rich components, leading to granite-like compositions. This ternary plot in Figure 5.5 supports the differentiation sequence observed in the field, where granodiorite felsic sheets represent the latest and most evolved phase, while tonalites and trondhjemites represent earlier, less evolved stages in the magmatic history of this suite.

TTGs are known to have a depletion in HREEs (heavy rare Earth elements) hence they have elevated Sr/Y and La_N/Yb_N ratios and no Eu anomaly (Moyen *et al*., 2007; Liou and Guo, 2019). This appears to be true for the TTG samples in this study. The chondrite normalized REE plots (Figure 5.9) show a depletion in HREEs and an enrichment in LREEs (light rare Earth elements) and Sr-Eu contents. According to Clemens *et al*., (2006) and Martin (1986), partial melting of the basaltic source leaves behind residual garnet and/or amphibole. The residual garnet and/or amphibole tend to incorporate HREEs, whereas the plagioclase in TTGs tends to incorporate Sr and Eu hence the depletion of HREEs (Clemens *et al*., 2006).

The TTG samples are closely grouped on the geochemical diagrams (Figures 5.1 and 5.2) suggesting that they formed from a common source or similar sources.

The amphibolite samples have lower SiO_2 values ranging from 45.53 wt.‰ to 49.75 wt.‰. They have more elevated proportions of K_2O, MgO and TiO_2 ranging from 1.96-5.79, 12.14-15.85 and 0.62-0.91 wt.‰, respectively. The amphibolite xenoliths classify as komatiitic basalts on the MgO versus Al_2O_3 discriminant diagram on Figure 5.10 (e). The Th/Yb versus Nb/Yb tectonic discriminant diagram on Figure 5.10 (c), for example, displays a volcanic arc geochemical signature for the amphibolite xenoliths, suggesting that they may have formed in a subduction zone setting prior to intrusion of the TTGs. However, this geochemical signature may also be due to crustal contamination.

7.1.4 Oxygen isotopes

Coarse-grained trondhjemites, fine to medium-grained tonalites and granodiorite sheets all have $\delta^{18}O$ quartz values that overlap, with a limited range from 8.72‰ to 9.71‰. There is no distinction between the $\delta^{18}O$ quartz values of the TTG rock types. The $\delta^{18}O$ quartz values of these TTG rock types being similar suggests that the same or similar source rock was melted to produce the coarse-grained trondhjemites, fine to medium-grained tonalites and granodiorite sheets of the Stolzburg pluton. According to Smith *et al*., (1984) and Faure and Harris (1991), mantle derived magmas have $\delta^{18}O$ quartz values of ~5.7‰. The $\delta^{18}O$ quartz values reported for the TTGs in this study are significantly higher than mantle values suggesting that the TTGs of the Stolzburg pluton could not have been entirely mantle derived but also could have been produced by either: (i) melting of the Archean mantle with crustal contamination, and/or (ii) direct melting of a mafic crustal amphibolite source followed by crustal assimilation.

Studies of oxygen isotopes in igneous rocks reveal that Archean zircon $\delta^{18}O$ quartz values generally fall between 5‰ and 7‰, reflecting their origin from primarily mantle-derived magmas (Bucholz and Spencer, 2019). However, during the late Archean, these values rose notably, reaching up to 10‰ (Valley, 2003; Valley *et al*., 2005; Spencer *et al*., 2014, 2017; Payne *et al*., 2015). This increase has been attributed to several factors, such as the onset or acceleration of subduction, which promoted the recycling of sediments into magma source regions, and changes in weathering processes linked to the Great Oxidation Event (Spencer *et al*., 2019).

The $\delta^{18}O$ quartz values of the Stolzburg TTGs, which suggest a crustal or mixed mantle-crustal source, can be compared to similar studies on late Archean TTGs in other regions. For example, Lei *et al*., 2023 report $\delta^{18}O$ quartz values for 2.95–2.93 Ga TTGs in China of 8.91 ± 0.05 ‰ to 9.94 ± 0.07 ‰ and 8.82 ‰ ± 0.05 ‰ (2SE) to 10.02 ‰ ± 0.07 ‰ for 2.75–2.71 Ga TTGs. They also report $\delta^{18}O$ quartz values of 9.43 ‰ ± 0.15 ‰ to 10.61 ‰ ± 0.17 ‰ (2SE) for 2.56–2.54 Ga TTGs (Lei *et al*., 2023). The authors propose that the decoupled Si–O isotopes in zircons indicate the influence of both supracrustal materials and komatiite-derived fluids in TTG genesis. This implies that the quartz oxygen isotopes in TTGs would reflect a mixture of these sources, with contributions from both the silicification of supracrustal materials and the interaction with fluids derived from komatiitic sources (Lei *et al*., 2023, Bucholz and Spencer, 2019).

7.1.5 U-Pb Zircon geochronology

The zircon age data for one coarse-grained trondhjemite (CT20) and one medium-grained tonalite (CT17) reveals crystallization ages of 3436 ± 26 Ma and 3419 ± 29 Ma, respectively. The ages overlap and are within error indicating that these TTGs intruded closely in time. The medium-grained tonalite was emplaced soon after the coarse-grained trondhjemite. This is supported by field relationships, which indicate coarse-grained trondhjemite xenoliths within the grey fine to medium-grained tonalite. The U-Pb ages (particularly for CT-17) are slightly younger than the published Stolzburg pluton ages ranging from 3437-3455 Ma, and this could be due to the nature of the Archean zircons and the method of dating that was used in this study which is different from the methods used to date the pluton previously.

7.2 TTG Petrogenesis and Geodynamic Models

TTG rocks are generally thought to have formed primarily through the partial melting of hydrated metabasaltic crust at pressures between 10 and 15 kbar (Laurent *et al*., 2024). These pressure conditions are typically found in subduction zone settings or under thickened oceanic plateau crustal settings. However, some studies have challenged this (Hernandez-Montenegro *et al*., 2021), proposing alternative geodynamic settings for TTG formation that do not rely on subduction or crustal thickening.

One such model is the plume-influenced rift setting for TTG generation, which argues that high Sr/Y and La/Yb ratios that are also seen in the Stolzburg TTGs, often attributed to high-pressure melting in subduction zones, can also result from partial melting of hydrated mafic crust in rift environments (Reimink et al., 2016). In this model, mantle plumes drive extensive mafic magmatism, with fractional crystallization and remelting producing TTG-like compositions. Similarly, Kamber (2015) suggests that TTGs could have formed through the melting at the base of basaltic plateaus buried to eclogite-facies depths (>40 km) by crustal thickening and volcanic loading, with mantle plume-induced heating facilitating partial melting (Bédard, 2006; Johnson *et al*., 2017; Van Kranendonk *et al*., 2014). This model helps explain TTG associations with greenstone belts.

Kendrick and Yakymchuk (2020) further complicate the subduction interpretation by demonstrating that garnet fractionation during melt migration and melt loss can also generate HREE-depleted signatures and alter trace element ratios (e.g., La/Yb, Sr/Y) also seen in Stolzburg TTGs, resembling high-pressure melting conditions. Additionally, bulk compositional variations in metabasalt protoliths influence TTG geochemistry independently of melting depth. A transitional model reconciles these views, suggesting that early Archean TTGs (pre-3.0 Ga) formed predominantly in non-subduction settings, while late Archean TTGs (post-3.0 Ga) reflect subduction zones as plate tectonics began to emerge (Kamber, 2015; Smit *et al*., 2019).

The following diagram (Figure 7.2) summarizes variations of the end-member models; the subduction and thickened oceanic plateau models.

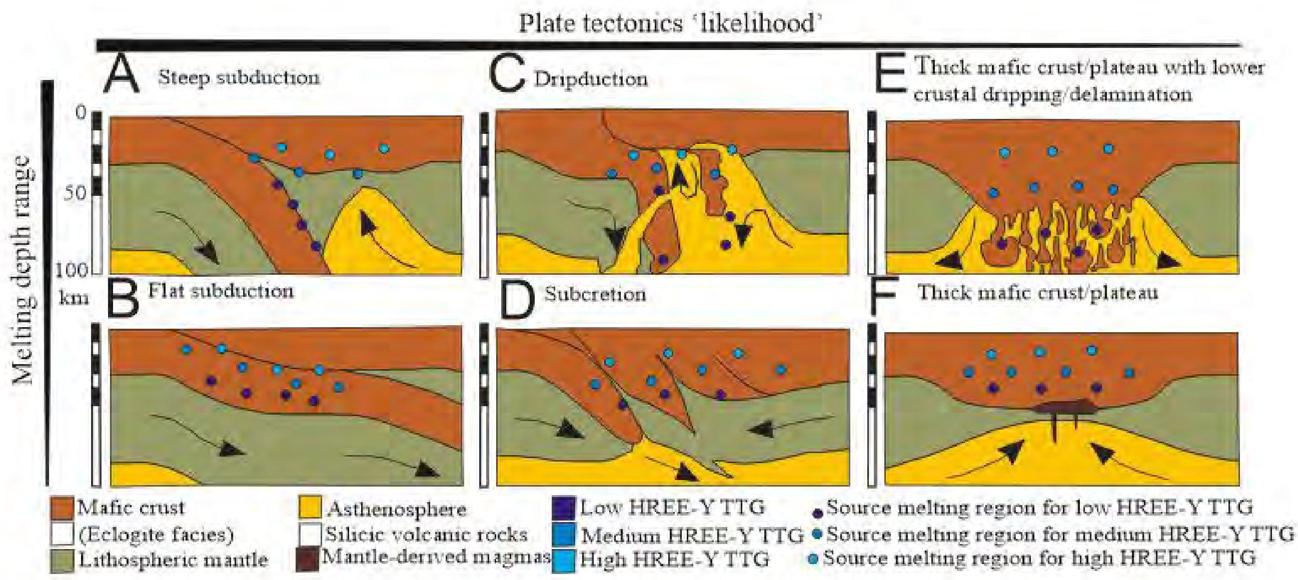

Figure 7.2: *A diagram showing possible geodynamic environments for the formation of TTGs. The top row represents wide range melting depth (20km - 100km) and the bottom row represents a narrow melting depth range (20km – 50km). The columns from left to right represent possible locations for these plate tectonic settings in various geodynamic environments (Modified after Laurent et al., 2024).*

Given the limitations and complexities of the alternative models explained above, subduction and thickened oceanic plateau still remain critical end-member scenarios for TTG petrogenesis. The subduction model is illustrated in Figure 7.2 (a) and (b), the only difference between the two scenarios being the angle (steep or shallow) of subduction. The subducting oceanic plate interacts with ocean water and is therefore hydrated with water and volatiles. As the oceanic plate subducts beneath another plate, it interacts with the mantle wedge where there are higher pressure and temperature conditions. The oceanic plate undergoes metamorphism where it releases water and volatiles thus lowering the melting temperature of the overlying mantle wedge. This leads to the partial melting of the mantle wedge to produce felsic magmas that are silica, aluminium and sodium rich. The felsic melt then ascends to emplacement levels where it forms part of the Earth's crust.

The subduction zone model is limited in explaining how the felsic TTG melts are able to ascend to their emplacement levels without reacting with mantle peridotites. Martin and Moyen, (2002) show that generally, 2.5 Ga TTGs have higher Mg# as compared to 4.0 Ga old TTGs suggesting that the mantle wedge was possibly too thin to have had substantially interacted with Archean TTG melts, or the melts did not have to ascend through the mantle wedge at all (as in the case of a flat subduction zone model).

Figure 7.2 (c) and (d) show variations of subduction and crustal thickening models referred to as “dripduction” and “subcretion” respectively. Dripduction which can also be referred to as delamination, involves the dripping of dense mafic crust into the mantle which can result in the melting of the crust at various depths in the mantle. Subcretion, on the other hand, occurs when the subducting mafic crust is added to the overriding crust, thus thickening the crust and subsequently resulting in the melting of the thickened crust due to high pressure.

The thickened oceanic plateau crust model is another model used to explain the formation of TTGs. The metabasaltic base of the thickened oceanic plateau interacts with the hot mantle and subsequently melts to produce TTG magmas (Figure 7.2 e and f). The thickened crust model can explain the low Mg# of Archean TTGs as interactions of the TTG melt and mantle are non-existent in this scenario.

Figure 7.2 shows the regions where TTGs with different HREE concentrations are found. The HREE concentrations seem to be influenced by different pressure conditions, however recent research shows that water-fluxed melting, the source rock and magma differentiation all contribute to the concentrations of elements in TTGs, thus affecting estimates of the depth of melting for TTGs (Laurent *et al*., 2024).

Given the higher $\delta^{18}O$ quartz values, it is highly likely that the Stolzburg TTGs were derived from isotopically heavier crustal material rather than only mantle material because the reported range of $\delta^{18}O$ quartz values of this study is significantly higher than that of mantle-derived magmas. The higher $\delta^{18}O$ quartz values reported herein indicate that a crustal component is required in the melt source of the Stolzburg pluton TTGs. The findings of this study imply that melt produced from metabasalt heating was contaminated with older intermediate TTG crust and possibly metasediments. This type of argument has been used for the petrogenesis of the 3.223 Ga Kaap Valley tonalite pluton (Faure and Harris, 1991). The strongly peraluminous geochemical signature recorded in the TTGs of the Stolzburg pluton also attests to mafic melt that experienced significant levels of crustal contamination. Possible sources of the crustal contaminant could be the much older c. 3.509 Ga Steynsdorp trondhjemite that was emplaced at varying crustal depths into early Archean oceanic lithosphere. It is proposed herein that trondhjemite-tonalite-granodiorite (TTG) suites and their significant geochemical heterogeneity, such as that recorded in the Stolzburg pluton, could be due to a number of factors. These include: (i) composition of the early Archean tholeiitic metabasaltic source rock (e.g. see Kendrick and Yakymchuk 2020), (ii) degree of hydrothermal alteration of the metabasaltic source, (iii) the extent of silicification of the metabasaltic source rock or contamination with silicified basalts (see Andre *et al.*, 2019), (iv) degree of partial melting in the source and (iv) extent of crustal contamination with older trondhjemitic-tonalitic intermediate composition crust (and possibly volcaniclastic sediments) during ascent and emplacement. The latter appears to be an important factor in the generation of the TTG rocks of the Stolzburg pluton. A spectrum of TTG rock compositions can be generated considering these factors. A more water-rich metabasalt source would produce an amphibole-bearing tonalite for example, whereas a drier, partially silicified metabasaltic source may produce a SiO_2 -rich, biotite bearing trondhjemite. It is also possible that komatiitic basalts were melted in the source.

The depth of metabasaltic melt generation could not be constrained in this MSc thesis. The geodynamic setting of the Stolzburg pluton TTG rocks remain unresolved based on the limitations of the datasets presented herein. Melting of metabasaltic sources could have taken place in a subduction zone or in a thickened oceanic plateau (plume) setting. However, it is interesting to point out that Mühlberg *et al*. (2021) reported that 3.45 Ga U-Pb apatite ages in the Stolzburg TTG pluton were not reset above the closure temperature of ~ 600^{o}C. This indicates that the Stolzburg pluton has remained relatively cool and undeformed since c. 3.45 Ga. The model proposed by Mühlberg *et al*. (2021), that kept the Stolzburg TTG crust relatively cool and protected from reheating, is the formation of a proto-keel or sublithospheric mantle at depth by lateral accretion or 'subcretion' of tectonically imbricated oceanic crust. Other field, metamorphic, U-Pb detrital zircon and metabasalt geochemical studies have also proposed the possibility of horizontal tectonics operating at c. 3.45 Ga in the BGGT (e.g. see Cutts *et al.*, 2023; Grosch *et al.*, 2011; de Wit *et al.*, 2011). Hence, the geochemical signatures recorded in the Stolzburg pluton could possibly be recording processes in a short-lived, proto-subduction zone setting on the early Archean Earth c. 3.45 billion years ago.

8. CONCLUSIONS

8 CONCLUSIONS

The geological mapping and geochemical analysis of Crusher's quarry reveal a complex intrusion sequence that is marked by distinct cross-cutting relationships among five rock types. The inclusion of coarse-grained trondhjemites within fine and medium-grained tonalites provide clear evidence that the trondhjemites represent the earliest phase of intrusion. The enveloping relationships of medium-grained tonalites by the fine-grained tonalites establishes a timeline where medium-grained tonalites were intruded before the fine-grained tonalites.

The felsic veins occurring in successive generations across these units further validate the time sequence, with the first-generation present in the oldest trondhjemites and subsequent generations cutting across the younger tonalites. The granodiorite sheets which crosscut all other units represent the final intrusive phase of the Stolzburg TTG pluton. The amphibolite xenoliths that occur in the trondhjemites and both tonalitic phases suggest multiple episodes of incorporation.

Petrographic data reveals the variations in mineralogy and texture across the TTG suite. The absence of hornblende in coarse-grained trondhjemites, contrasted with its presence in fine to medium-grained tonalites, points out the mineralogical differences between trondhjemites and tonalites. The presence of biotite and sphene across all TTG types, alongside polysynthetic zoning in plagioclase grains, suggests that these rocks crystallized under conditions of fluctuating melt composition, potentially because of changing pressure during magma ascent.

U-Pb zircon geochronology of the coarse-grained trondhjemite (CT 20) and medium-grained tonalite (CT 17) from the Stolzburg pluton reveals overlapping crystallization ages which fall within error, indicating that these TTGs were emplaced closely in time in the Archean. This proximity in time is consistent with field evidence showing xenoliths of coarse-grained trondhjemite within the medium-grained tonalite, suggesting that the medium-grained tonalite was emplaced shortly after the trondhjemite. Future work would require the use of a more sensitive and accurate U-Pb dating technique, such as Secondary Ion Microprobe (SIMS) or SHRIMP.

The geochemistry of the Stolzburg TTGs reveals important clues about their genesis. The high SiO_2 and low MgO and TiO_2 contents of the coarse-grained trondhjemites, compared to the fine to medium-grained tonalites, indicate progressive differentiation of the melt during its evolution. The observed negative Nb anomalies (Figure 5.8) and the lack of strong trace element versus SiO_2 relationships (Figure 5.1) Harker plots suggest that fractional crystallization played a minor role in TTG formation. Additionally, the depletion in heavy Rare Earth Elements (HREEs) and enrichment in light Rare Earth Elements (LREEs) and Sr-Eu contents, as demonstrated by the chondrite-normalized REE plots, further verifies the role of garnet (and possibly amphibole) in the metabasaltic source during TTG production. Garnet incorporates HREEs, while plagioclase incorporates Sr and Eu, leading to the observed geochemical patterns. The geochemistry of the amphibolite xenoliths is difficult to interpret: they could be recording crustal contamination with older TTG crust and/or have formed in an early Archean subduction zone setting. Further work is required to test the source characteristics of the amphibolites (e.g. whole rock Lu-Hf isotope studies).

The TTG rocks of the Stolzburg pluton record a strong peraluminous signature. These rocks also have elevated (above mantle) $\delta^{18}O$ quartz values of the Stolzburg pluton TTG rocks ranging between 8.72 to 9.71‰. These geochemical signatures point to melt generation from a metabasalt in the garnet stability field that was subsequently heavily contaminated by older intermediate crust during ascent and emplacement. A number of factors are reported herein that controlled the mineralogy and composition of the Stolzburg pluton TTG suite. These include the composition of the metabasaltic source, the degree of hydrothermal alteration in the metabasalt source and the extent of crustal contamination of the metabasaltic melt with older, pre-existing TTG crust and sediments. The geodynamic setting of the Stolzburg TTG pluton remains an open question. It is possible that the setting was a thickened oceanic plateau or that thickening of the lithosphere occurred by lateral tectonic processes. In light of recent geological and petrological studies, a geodynamic model of thickening by horizontal subcretion and tectonic imbrication of oceanic lithosphere before melting of metabasalt to produce TTGs is a possibility.

9 REFERENCES

Abraham, K., Hofmann, A., Foley, S.F., Cardinal, D., Harris, C., Barth, M.G. and André, L., 2011. Coupled silicon–oxygen isotope fractionation traces Archaean silicification. *Earth and Planetary Science Letters*, 301(1-2), pp.222-230.

Anhaeusser, C.R., Robb, L.J., and Viljoen, M.J., 1983. Notes on the provisional geological map of the Barberton greenstone belt and surrounding granitic terrane, eastern Transvaal and Swaziland (1: 250 000 colour map).

Anhaeusser, C.R., Mason, R., Viljoen, M.J. and Viljoen, R.P., 1969. A reappraisal of some aspects of Precambrian shield geology. *Geological Society of America Bulletin*, *80*(11), pp.2175-2200.

Anhaeusser, C.R., 2019. The geology and tectonic evolution of the northwest part of the Barberton Greenstone Belt, South Africa: A review. *South African Journal of Geology 2019*, *122*(4), pp.421-454.

André, L., Abraham, K., Hofmann, A., Monin, L., Kleinhanns, I.C. and Foley, S., 2019. Early continental crust generated by reworking of basalts variably silicified by seawater. *Nature Geoscience*, 12(9), pp.769-773.

Armstrong, R.A., Compston, W., De Wit, M.J. and Williams, I.S., 1990. The stratigraphy of the 3.5-3.2 Ga Barberton Greenstone Belt revisited: a single zircon ion microprobe study. *Earth and Planetary Science Letters*, *101*(1), pp.90-106.

Arndt, N.T., 2013. Section 5. Generation of TTG and Archean Tectonics. *Geochemical Perspectives*, *2*(3), pp.436-462.

Barker, F., 1979. Trondhjemite: definition, environment and hypotheses of origin. In *Developments in petrology* (Vol. 6, pp. 1-12). Elsevier.

Bédard, J.H., 2006. A catalytic delamination-driven model for coupled genesis of Archaean crust and sub-continental lithospheric mantle. *Geochimica et cosmochimica acta*, *70*(5), pp.1188-1214.

Belcher, R.W. and Kisters, A.F., 2006. Progressive adjustments of ascent and emplacement controls during incremental construction of the 3.1 Ga Heerenveen batholith, South Africa. *Journal of Structural Geology*, *28*(8), pp.1406-1421.

Bindeman, I.N., Ionov, D.A., Tollan, P.M. and Golovin, A.V., 2022. Oxygen isotope (δ18O, Δ' 17O) insights into continental mantle evolution since the Archean. *Nature Communications*, 13(1), p.3779.

Brandl, G., Cloete, M. and Anhaeusser, C.R., 2006. Archaean greenstone belts. *The Geology of South Africa*, pp.9-56.

Bucholz, C.E. and Spencer, C.J., 2019. Strongly peraluminous granites across the Archean–Proterozoic transition. *Journal of Petrology*, *60*(7), pp.1299-1348.

Chen, S., Li, J., Yuan, F., Jowitt, S.M., Li, L., Deng, Y., Liu, H. and Jiang, R., 2023. Modern-style subduction during the late Neoarchean to early Paleoproterozoic? Geochemical evidence from ca. 2.45 Ga arc-type magmatism in the Feidong Complex, northeastern Yangtze Craton, South China. *Precambrian Research*, *388*, p.106999.

Clemens, J.D., Yearron, L.M. and Stevens, G., 2006. Barberton (South Africa) TTG magmas: geochemical and experimental constraints on source-rock petrology, pressure of formation and tectonic setting. *Precambrian Research*, *151*(1-2), pp.53-78.

Clemens, J.D., Belcher, R.W. and Kisters, A.F., 2010. The Heerenveen batholith, Barberton Mountain Land, South Africa: Mesoarchaean, potassic, felsic magmas formed by melting of an ancient subduction complex. *Journal of Petrology*, *51*(5), pp.1099-1120.

Cosca, M.A., Essene, E.J. and Bowman, J.R., 1991. Complete chemical analyses of metamorphic hornblendes: Implications for normalizations, calculated H 2 O activities, and thermobarometry. *Contributions to Mineralogy and Petrology*, 108, pp.472-484.

Cox, K.G., Bell, J.D. and Pankhurst, R.J., 1979. The Interpretation of Igneous Rocks. *George Allen & Unwin Limited, London*, 450 pp.

Cutts, K.A., Stevens, G., Hoffmann, J.E., Buick, I.S., Frei, D. and Münker, C., 2014. Paleo-to Mesoarchean polymetamorphism in the Barberton Granite-Greenstone Belt, South Africa: Constraints from U-Pb monazite and Lu-Hf garnet geochronology on the tectonic processes that shaped the belt. *Bulletin*, *126*(3-4), pp.251-270.

Cutts, K.A., Maneiro, K.A., Stevens, G. and Baxter, E.F., 2021. Metamorphic evolution for the Inyoni shear zone: Investigating the geodynamic evolution of a 3.20 Ga terrane boundary in the Barberton granitoid greenstone terrane, South Africa. *South African Journal of Geology 2021*, *124*(1), pp.163-180.

Cutts, K.A., Lana, C., Stevens, G. and Buick, I.S., 2023. In situ Pb–Pb garnet geochronology as a tool for investigating polymetamorphism: a case for Paleoarchean lateral tectonic thickening.

Dann, J.C., 2000. The 3.5 Ga Komati Formation, Barberton greenstone belt, South Africa, part I: new maps and magmatic architecture. *South African Journal of Geology*, 103(1), pp.47-68.

de Ronde, C.E. and de Wit, M.J., 1994. Tectonic history of the Barberton greenstone belt, South Africa: 490 million years of Archean crustal evolution. *Tectonics*, 13(4), pp.983-1005.

de Ronde, C.E. and Kamo, S.L., 2000. An Arch1 an arc-arc collisional event: a short-lived (ca 3 Myr) episode, Weltevreden area, Barberton greenstone belt, South Africa. *Journal of African Earth Sciences*, *30*(2), pp.219-248.

de Wit, M.J., 1983. Notes on a preliminary 1: 25 000 geological map of the southern part of the Barberton greenstone belt.

de Wit, M.J., Furnes, H. and Robins, B., 2011. Geology and tectonostratigraphy of the Onverwacht Suite, Barberton greenstone belt, South Africa. *Precambrian Research*, 186(1-4), pp.1-27.

Diener, J. F. A., and A. Dziggel. 2021. Can mineral equilibrium modelling provide additional details on metamorphism of the Barberton garnet amphibolites? *South African Journal of Geology*, 124(1), pp 211-224.

Diener, J.F., Stevens, G., Kisters, A.F. and Poujol, M., 2005. Metamorphism and exhumation of the basal parts of the Barberton greenstone belt, South Africa: Constraining the rates of Mesoarchaean tectonism. *Precambrian Research*, *143*(1-4), pp.87-112.

Dziggel, A., Stevens, G., Poujol, M., Anhaeusser, C.R. and Armstrong, R.A., 2002. Metamorphism of the granite–greenstone terrane south of the Barberton greenstone belt, South Africa: an insight into the tectono-thermal evolution of the 'lower'portions of the Onverwacht Group. *Precambrian Research*, *114*(3-4), pp.221-247.

Eriksson, P.G., Altermann, W., Nelson, D.R., Mueller, W.U., Catuneanu, O. and Catuneanu, O. eds., 2004. *The Precambrian Earth: tempos and events* (Vol. 12). Elsevier.

Faure, K. and Harris, C., 1991. Oxygen and carbon isotope geochemistry of the 3.2 Ga Kaap Valley tonalite, Barberton greenstone belt, South Africa. *Precambrian Research*, 52(3-4), pp.301-319.

Foley, S., Tiepolo, M. and Vannucci, R., 2002. Growth of early continental crust controlled by melting of amphibolite in subduction zones. *Nature*, 417(6891), pp.837-840.

Foley, S.F., Buhre, S. and Jacob, D.E., 2003. Evolution of the Archaean crust by delamination and shallow subduction. *Nature*, 421(6920), pp.249-252.

Grosch, E. G., 2011. Determining the physico-chemical conditions on the early Earth: Barberton scientific drilling project, South Africa. Western Cape: University of Cape Town (Doctoral Thesis).

Grosch, E.G., Kosler, J., McLoughlin, N., Drost, K., Slama, J., Pedersen, R.B., 2011. Paleoarchean detrital zircon ages from the earliest tectonic basin in the Barberton Greenstone Belt, Kaapvaal craton, South Africa, *Precambrian Research* 191 (1-2), 85-99.

Grosch, E.G., Vidal, O., Abu-Alam, T. and McLoughlin, N., 2012. P–T constraints on the metamorphic evolution of the Paleoarchean Kromberg type-section, Barberton Greenstone Belt, South Africa. *Journal of Petrology*, *53*(3), pp.513-545.

Grosch, E.G., 2019. Metamorphic processes preserved in early Archean supracrustal rocks of the Barberton Greenstone Belt, South Africa. *Geological Society, London, Special Publications*, *478*(1), pp.315-334.

Grosch, E.G., Viola, G. and Ndlela, S., 2020. Geological record of Paleoarchean oceanic flake tectonics preserved in the c. 3.3 Ga Kromberg volcanic type-section, Barberton greenstone belt, South Africa. *Precambrian Research*, *346*, p.105815.

Grosch, E.G. and Slama, J., 2021. On the volcanic architecture, petrology and geodynamic setting of the 3.48 Ga Barberton komatiite suite, South Africa. *South African Journal of Geology 2021*, *124*(2), pp.343-352.

Harris, C. and Vogeli, J., 2010. Oxygen isotope composition of garnet in the Peninsula Granite, Cape Granite Suite, South Africa: constraints on melting and emplacement mechanisms. *South African Journal of Geology*, *113*(4), pp.401-412.

Hawkesworth, C.J., Marsh, J.S., Duncan, A.R., Erlank, A.J. and Norry, M.J., 1984. The role of continental lithosphere in the generation of the Karoo volcanic rocks: evidence fom combined Nd-and Sr-isotopes studies. *Geol. Soc. South Afr. Spec. Publ*, *13*, pp.341-354.

Herzberg, C., 1992. Depth and degree of melting of komatiites. *Journal of Geophysical Research: Solid Earth*, *97*(B4), pp.4521-4540.

Hofmann, A. and Harris, C., 2008. Silica alteration zones in the Barberton greenstone belt: a window into subseafloor processes 3.5–3.3 Ga ago. *Chemical Geology*, 257(3-4), pp.221-239.

Hofmann, A.W., 1997. Mantle geochemistry: the message from oceanic volcanism. *Nature*, 385(6613), pp.219-229.

Hollocher, K., Robinson, P., Walsh, E. and Roberts, D., 2012. Geochemistry of amphibolite-facies volcanics and gabbros of the Støren Nappe in extensions west and southwest of Trondheim, Western Gneiss Region, Norway: a key to correlations and paleotectonic settings. *American Journal of Science*, *312*(4), pp.357-416.

Horstwood, M.S.A., Foster, G.L., Parrish, R.R. and Noble, S.R., 2001, May. Common-Pb and inter-element corrected U-Pb geochronology by la-mc-icp-ms. In *Eleventh Annual VM Goldschmidt Conference* (p. 3698).

Huang, X.L., Niu, Y., Xu, Y.G., Yang, Q.J. and Zhong, J.W., 2010. Geochemistry of TTG and TTG-like gneisses from Lushan-Taihua complex in the southern North China Craton: implications for late Archean crustal accretion. *Precambrian Research*, *182*(1-2), pp.43-56.

Hunter, D.R., Barker, F. and Millard Jr, H.T., 1978. The geochemical nature of the Archean Ancient Gneiss Complex and Granodiorite Suite, Swaziland: a preliminary study. *Precambrian Research*, *7*(2), pp.105-127.

Ionov, D.A. and Hofmann, A.W., 1995. Nb-Ta-rich mantle amphiboles and micas: Implications for subduction-related metasomatic trace element fractionations. *Earth and Planetary Science Letters*, *131*(3-4), pp.341-356.

Jackson, S., Pearson, N.J., Griffin, W.L. and Belousova, E.A., 2004. The application of laser ablation-inductively coupled plasma-mass spectrometry to in situ U-Pb zircon geochronology. *Chemical Geology*, 211(1-2), pp.47-69.

Johnson, T.E., Brown, M., Gardiner, N.J., Kirkland, C.L. and Smithies, R.H., 2017. Earth's first stable continents did not form by subduction. *Nature*, *543*(7644), pp.239-242.

Johnson, T.E., Kirkland, C.L., Gardiner, N.J., Brown, M., Smithies, R.H. and Santosh, M., 2019. Secular change in TTG compositions: Implications for the evolution of Archaean geodynamics. *Earth and Planetary Science Letters*, *505*, pp.65-75.

Kamber, B.S., 2015. The evolving nature of terrestrial crust from the Hadean, through the Archaean, into the Proterozoic. *Precambrian Research*, *258*, pp.48-82.

Kamo, S.L. and Davis, D.W., 1994. Reassessment of Archean crustal development in the Barberton Mountain Land, South Africa, based on U-Pb dating. *Tectonics*, *13*(1), pp.167-192.

Kato, D., Aoki, K., Komiya, T., Yamamoto, S., Sawaki, Y., Asanuma, H., Sato, T., Tsuchiya, Y., Shozugawa, K., Matsuo, M. and Windley, B.F., 2018. Constraints on the P–T conditions of high-pressure metamorphic rocks from the Inyoni shear zone in the mid-Archean Barberton Greenstone Belt, South Africa. *Precambrian Research*, *315*, pp.1-18.

Kendrick, J. and Yakymchuk, C., 2020. Garnet fractionation, progressive melt loss and bulk composition variations in anatectic metabasites: Complications for interpreting the geodynamic significance of TTGs. *Geoscience Frontiers*, *11*(3), pp.745-763.

Kieffer, M.A., Mathieu, L., Bedeaux, P., Gaboury, D. and Hamilton, M.A., 2022. Petrogenesis and mode of emplacement of a Neoarchean tonalite–trondhjemite–diorite suite: the Eau Jaune Complex, Abitibi greenstone belt. *Canadian Journal of Earth Sciences*, 59(2), pp.87-110.

Kisters, A.F. and Anhaeusser, C.R., 1995. Emplacement features of Archaean TTG plutons along the southern margin of the Barberton greenstone belt, South Africa. *Precambrian Research*, *75*(1-2), pp.1-15.

Knauth, L.P. and Lowe, D.R., 2003. High Archean climatic temperature inferred from oxygen isotope geochemistry of cherts in the 3.5 Ga Swaziland Supergroup, South Africa. *Geological Society of America Bulletin*, *115*(5), pp.566-580.

Kramers, J., Frei, R., Newville, M., Kober, B. and Villa, I., 2009. On the valency state of radiogenic lead in zircon and its consequences. *Chemical Geology*, *261*(1-2), pp.4-11.

Kröner, A. and Tegtmeyer, A., 1994. Gneiss-greenstone relationships in the Ancient Gneiss Complex of southwestern Swaziland, southern Africa, and implications for early crustal evolution. *Precambrian Research*, 67(1-2), pp.109-139.

Kröner, A., Hegner, E., Wendt, J.I. and Byerly, G.R., 1996. The oldest part of the Barberton granitoid-greenstone terrain, South Africa: evidence for crust formation between 3.5 and 3.7 Ga. *Precambrian Research*, *78*(1-3), pp.105-124.

Laurent, O., Martin, H., Moyen, J.F. and Doucelance, R., 2014. The diversity and evolution of late-Archean granitoids: Evidence for the onset of “modern-style” plate tectonics between 3.0 and 2.5 Ga. *Lithos*, *205*, pp.208-235.

Laurent, O., Guitreau, M., Bruand, E. and Moyen, J.F., 2024. At the dawn of continents: Archean tonalite-trondhjemite-granodiorite suites. *Elements*, 20(3), pp.174-179.

Layer, P.W., Kröner, A. and York, D., 1992. Pre-3000 Ma thermal history of the Archean Kaap Valley puton, South Africa. *Geology*, *20*(8), pp.717-720.

Lei, K., Wang, H., Wang, X., Zhang, Q. and Li, X.H., 2023. Decoupled Zircon Si–O Isotopes Tracing the Supracrustal Silicification and Komatiitic-Derived Fluids in the Source of TTGs. *Geophysical Research Letters*, *50*(16), p.e2023GL104002.

Liou, P. and Guo, J., 2019. Generation of Archaean TTG gneisses through amphibole-dominated fractionation. *Journal of Geophysical Research: Solid Earth*, 124(4), pp.3605-3619.

Lowe, D.R., 1999. Geologic evolution of the Barberton Greenstone Belt and vicinity.

Lowe, D.R. and Byerly, G.R., 1999. Stratigraphy of the west-central part of the Barberton Greenstone Belt, South Africa.

Lowe, D.R. and Byerly, G.R., 2007. An overview of the geology of the Barberton Greenstone Belt and vicinity: implications for early crustal development. *Developments in Precambrian geology*, *15*, pp.481-526.

Luais, B. and Hawkesworth, C.J., 1994. The generation of continental crust: an integrated study of crust-forming processes in the Archaean of Zimbabwe. *Journal of Petrology*, 35(1), pp.43-94.

Maré, L.P. and Fourie, C.J.S., 2012. New geochemical and palaeomagnetic results from Neoarchaean dyke swarms in the Badplaas-Barberton area, South Africa. *South African Journal of Geology*, *115*(2), pp.145-170.

Martin, H., 1986. Effect of steeper Archean geothermal gradient on geochemistry of subduction-zone magmas. *Geology*, *14*(9), pp.753-756.

Martin, H., 1999. Adakitic magmas: modern analogues of Archaean granitoids. *Lithos*, *46*(3), pp.411-429.

Martin, H., Smithies, R.H., Rapp, R., Moyen, J.F. and Champion, D., 2005. An overview of adakite, tonalite–trondhjemite–granodiorite (TTG), and sanukitoid: relationships and some implications for crustal evolution. *Lithos*, *79*(1-2), pp.1-24.

Metcalf, R.V., Shervais, J.W. and Wright, J.E., 2008. Suprasubduction-zone ophiolites: Is there really an ophiolite conundrum?. *Special Papers-Geological Society of America*, *438*, p.191.

Moyen, J.F., 2011. The composite Archaean grey gneisses: petrological significance, and evidence for a non-unique tectonic setting for Archaean crustal growth. *Lithos*, *123*(1-4), pp.21-36.

Moyen, J.F. and Martin, H., 2012. Forty years of TTG research. *Lithos*, 148, pp.312-336.

Moyen, J.F., Stevens, G. and Kisters, A., 2006. Record of mid-Archaean subduction from metamorphism in the Barberton terrain, South Africa. *Nature*, *442*(7102), pp.559-562.

Moyen, J.F., Stevens, G., Kisters, A.F. and Belcher, R.W., 2007. TTG plutons of the Barberton granitoid-greenstone terrain, South Africa. *Developments in Precambrian Geology*, 15, pp.607-667.

Moyen, J.F., 2020. Archean granitoids: classification, petrology, geochemistry and origin.

Mühlberg, M., Stevens, G., Moyen, J.F., Kisters, A.F. and Lana, C., 2021. Thermal evolution of the Stolzburg Block, Barberton granitoid-greenstone terrain, South Africa: Implications for Paleoarchean tectonic processes. *Precambrian Research*, *359*, p.106082.

Muhlberg, M., 2022. *Magmatic and metamorphic evolution of the Stolzburg Block, Barberton Granitoid-Greenstone Terrain* (Doctoral dissertation, Stellenbosch: Stellenbosch University).

Ouyang, D., Bao, H., Byerly, G.R. and Li, Q., 2024. Light oxygen isotopic composition in deep mantle reveals oceanic crust subduction before 3.3 billion years ago. *Communications Earth & Environment*, 5(1), p.34.

Paton, C., Hellstrom, J., Paul, B., Woodhead, J. and Hergt, J., 2011. Iolite: Freeware for the visualisation and processing of mass spectrometric data. *Journal of Analytical Atomic Spectrometry*, *26*(12), pp.2508-2518.

Payne, J.L., Hand, M., Pearson, N.J., Barovich, K.M. and McInerney, D.J., 2015. Crustal thickening and clay: Controls on O isotope variation in global magmatism and siliciclastic sedimentary rocks. *Earth and Planetary Science Letters*, *412,* pp.70-76.

Pearce, J.A. and Peate, D.W., 1995. Tectonic implications of the composition of volcanic arc magmas. *Annual Review of Earth and Planetary Sciences*, 23, pp.251-286.

Peccerillo, A. and Taylor, S.R., 1976. Geochemistry of Eocene calc-alkaline volcanic rocks from the Kastamonu area, northern Turkey. *Contributions to mineralogy and petrology*, *58*, pp.63-81.

Peng, T., Wang, G.D., Wang, H.Y., Liu, J.H., Zhang, H.C., Chen, H.X. and Wu, C.M., 2019. Metamorphic PT path and geochronology of garnet-bearing amphibolite of the Inyoni Shear Zone, southwestern Barberton Greenstone Belt, South Africa. *Precambrian Research*, *321*, pp.261-276.

Proteau G., Scaillet B., Pichavant M., Maury R., 2001. Evidence for mantle metasomatism by hydrous silicic melts derived from subducted oceanic crust. Nature 410, 197-200.

Rapp, R.P., Watson, E.B. and Miller, C.F., 1991. Partial melting of amphibolite/eclogite and the origin of Archean trondhjemites and tonalites. *Precambrian Research*, *51*(1-4), pp.1-25.

Rapp, R.P., Shimizu, N. and Norman, M.D., 2003. Growth of early continental crust by partial melting of eclogite. *Nature*, *425*(6958), pp.605-609.

Rapp, R.P. and Watson, E.B., 1995. Dehydration melting of metabasalt at 8–32 kbar: implications for continental growth and crust-mantle recycling. *Journal of Petrology*, *36*(4), pp.891-931.

Reimink, J.R., Chacko, T., Stern, R.A. and Heaman, L.M., 2016. The birth of a cratonic nucleus: Lithogeochemical evolution of the 4.02–2.94 Ga Acasta Gneiss Complex. *Precambrian Research*, *281*, pp.453-472.

Reimink, J.R. and Smye, A.J., 2024. Subaerial weathering drove stabilization of continents. *Nature*, *629*(8012), pp.609-615.

Rey, P.F., Coltice, N. and Flament, N., 2024. Archean geodynamics underneath weak, flat, and flooded continents. *Elements*, *20*(3), pp.180-186.

Reymer, A. and Schubert, G., 1984. Phanerozoic addition rates to the continental crust and crustal growth. *Tectonics*, *3*(1), pp.63-77.

Robb, L.J., Barton Jr, J.M., Kable, E.J.D. and Wallace, R.C., 1986. Geology, geochemistry and isotopic characteristics of the Archaean Kaap Valley pluton, Barberton mountain land, South Africa. *Precambrian Research*, *31*(1), pp.1-36.

Robb, L.J., Brandl, G., Anhaeusser, C.R., Poujol, M., Johnson, M.R. and Thomas, R.J., 2006. Archaean granitoid intrusions. *The Geology of South Africa*, pp.57-94.

Rollinson, H.R., 1993. A terrane interpretation of the Archaean Limpopo Belt. *Geological Magazine*, *130*(6), pp.755-765.

Rudnick, R.L., 1995. Making continental crust. *Nature*, *378*(6557), pp.571-578.

Sarkar, T., Dubinina, E.O., Harris, C., Maier, W.D. and Mouri, H., 2018. Petrogenesis of ultramafic rocks of komatiitic composition from the Central Zone of the Limpopo Belt, South Africa: Evidence from O and H isotopes. *Journal of African Earth Sciences*, 147, pp.68-77.

Schoene, B., de Wit, M.J. and Bowring, S.A., 2008. Mesoarchean assembly and stabilization of the eastern Kaapvaal craton: A structural-thermochronological perspective. *Tectonics*, *27*(5).

Shan, H., Zhai, M., Oliveira, E.P., Santosh, M. and Wang, F., 2015. Convergent margin magmatism and crustal evolution during Archean-Proterozoic transition in the Jiaobei terrane: Zircon U–Pb ages, geochemistry, and Nd isotopes of amphibolites and associated grey gneisses in the Jiaodong complex, North China Craton. *Precambrian Research*, *264*, pp.98-118.

Shervais, J.W., 1982. Ti-V plots and the petrogenesis of modern and ophiolitic lavas. *Earth and planetary science letters*, *59*(1), pp.101-118.

Sláma, J., Košler, J., Condon, D.J., Crowley, J.L., Gerdes, A., Hanchar, J.M., Horstwood, M.S., Morris, G.A., Nasdala, L., Norberg, N. and Schaltegger, U., 2008. Plešovice zircon—a new natural reference material for U–Pb and Hf isotopic microanalysis. *Chemical Geology*, *249*(1-2), pp.1-35.

Smit, M.A., Scherstén, A., Naeraa, T., Emo, R.B., Scherer, E.E., Sprung, P., Bleeker, W., Mezger, K., Maltese, A., Cai, Y. and Rasbury, E.T., 2019. Formation of Archean continental crust constrained by boron isotopes. *Geochemical Perspectives Letters*, *12*, pp.23-26.

Smith, M.A. and Pell, S., 1997. Oxygen-isotope ratios in quartz as indicators of the provenance of archaeological ochres. *Journal of Archaeological Science*, *24*(9), pp.773-778.

Smithies, R.H., 2000. The Archaean tonalite–trondhjemite–granodiorite (TTG) series is not an analogue of Cenozoic adakite. *Earth and Planetary Science Letters*, *182*(1), pp.115-125.

Spencer, C.J., Cawood, P.A., Hawkesworth, C.J., Raub, T.D., Prave, A.R. and Roberts, N.M., 2014. Proterozoic onset of crustal reworking and collisional tectonics: Reappraisal of the zircon oxygen isotope record. *Geology*, *42*(5), pp.451-454.

Spencer, C.J., Cavosie, A.J., Raub, T.D., Rollinson, H., Jeon, H., Searle, M.P., Miller, J.A., McDonald, B.J., Evans, N.J. and Edinburgh Ion Microprobe Facility (EIMF), 2017. Evidence for melting mud in Earth's mantle from extreme oxygen isotope signatures in zircon. *Geology*, *45*(11), pp.975-978.

Spencer, C.J., Partin, C.A., Kirkland, C.L., Raub, T.D., Liebmann, J. and Stern, R.A., 2019. Paleoproterozoic increase in zircon δ18O driven by rapid emergence of continental crust. *Geochimica et Cosmochimica Acta*, *257*, pp.16-25.

Sun, G., Liu, S., Cawood, P.A., Tang, M., van Hunen, J., Gao, L., Hu, Y. and Hu, F., 2021. Thermal state and evolving geodynamic regimes of the Meso-to Neoarchean North China Craton. *Nature Communications*, *12*(1), p.3888.

Sun, S.S. and McDonough, W.F., 1989. Chemical and isotopic systematics of oceanic basalts: implications for mantle composition and processes. *Geological Society, London, Special Publications*, *42*(1), pp.313-345.

Tiepolo, M., 2003. In situ Pb geochronology of zircon with laser ablation–inductively coupled plasma–sector field mass spectrometry. *Chemical geology*, *199*(1-2), pp.159-177.

Valley, J.W., 2003. Oxygen isotopes in zircon. *Reviews in mineralogy and geochemistry*, *53*(1), pp.343-385.

Valley, J.W., Lackey, J.S., Cavosie, A.J., Clechenko, C.C., Spicuzza, M.J., Basei, M.A.S., Bindeman, I.N., Ferreira, V.P., Sial, A.N., King, E.M. and Peck, W.H., 2005. 4.4 billion years of crustal maturation: oxygen isotope ratios of magmatic zircon. *Contributions to Mineralogy and Petrology*, *150*, pp.561-580.

Van Kranendonk, M.J., Hugh Smithies, R., Hickman, A.H. and Champion, D.C., 2007. secular tectonic evolution of Archean continental crust: interplay between horizontal and vertical processes in the formation of the Pilbara Craton, Australia. *Terra Nova*, *19*(1), pp.1-38.

Van Kranendonk, M.J., Kröner, A., Hoffmann, J.E., Nagel, T. and Anhaeusser, C.R., 2014. Just another drip: Re-analysis of a proposed Mesoarchean suture from the Barberton Mountain Land, South Africa. *Precambrian Research*, *254*, pp.19-35.

Vezinet, A., Pearson, D.G., Thomassot, E., Stern, R.A., Sarkar, C., Luo, Y. and Fisher, C.M., 2018. Hydrothermally-altered mafic crust as source for early Earth TTG: Pb/Hf/O isotope and trace element evidence in zircon from TTG of the Eoarchean Saglek Block, N. Labrador. *Earth and Planetary Science Letters*, *503*, pp.95-107.

Viljoen, R.P. and Viljoen, M.J., 1969. The relationship between mafic and ultramafic magma derived from the upper mantle and the ore deposits of the Barberton region. *Geol., Soc. South Africa Spec. Pub*, *2*, pp.221-244.

Viljoen, M.J., Viljoen, R.P., Smith, H.S., Erlank, A.J., 1983. Geological, textural and geochemical features of komatiitic flows from the Komati Formation. Geol. Soc. South Africa Spec. Publ. 1–20.

Wan, J., Wang, A., Pan, J., Liu, C., Zhao, Y., Zhou, Z. and Luo, X., 2021. Episodic Crustal growth and Reworking at the southeastern margin of the North China Craton: evidence from Zircon U–Pb and Lu–Hf isotopes of Archean tonalite–trondhjemite–granodiorite gneisses in the Bengbu-Wuhe area. *Acta Geochimica*, *40*, pp.366-389.

Wetherill, G.W., 1956. Discordant uranium-lead ages, I. *Eos, Transactions American Geophysical Union*, *37*(3), pp.320-326.

Wiedenbeck, M.A.P.C., Alle, P., Corfu, F.Y., Griffin, W.L., Meier, M., Oberli, F.V., Quadt, A.V., Roddick, J.C. and Spiegel, W., 1995. Three natural zircon standards for U-Th-Pb, Lu-Hf, trace element and REE analyses. *Geostandards newsletter*, *19*(1), pp.1-23.

Woodhead, J., Hergt, J., Greig, A. and Edwards, L., 2011. Subduction zone Hf-anomalies: Mantle messenger, melting artefact or crustal process?. *Earth and Planetary Science Letters*, *304*(1-2), pp.231-239.

Yearron, L.M., 2003. *Archaean granite petrogenesis and implications for the evolution of the Barberton Mountain Land, South Africa* (Doctoral dissertation, Kingston University).

10 APPENDICES

10.1 Appendix A: Field photos

Figure 10.1.1. A rock body on Crusher's quarry exhibiting coarse-grained trondhjemites entrained in a fine-grained tonalite and some granodioritic felsic sheets running through the fine-grained tonalite.

Figure 10.1.2.(a) and (b) show amphibolite xenoliths entrapped in the TTGs of Crusher's quarry. (c) shows amphibolite slivers and weathered TTGs in a river section 1.7 km west of Crusher's Quarry.

Figure 10.1.3. An image showing more field crosscutting relationships where coarse-grained trondhjemites are entrained in medium-grained tonalites. There are also granodioritic felsic sheets within the medium-grained tonalites.

Figure 10.1.4. A picture of a granodioritic felsic sheet cutting across medium-grained tonalite.

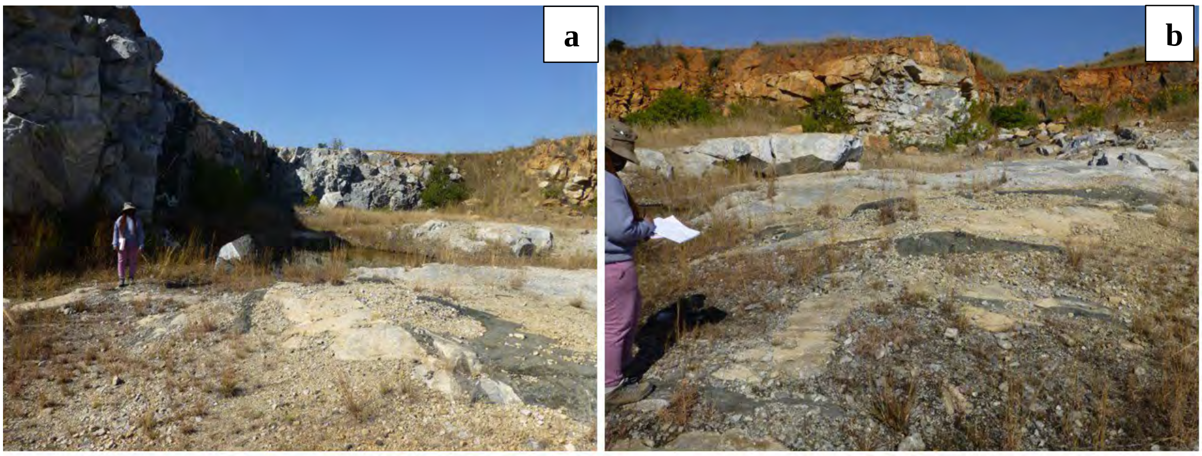

Figure 10.1.5. (a) Picture showing the east face connecting to the north face. (b) Picture showing the north face connecting with the weathered southwest face that could not be mapped.

Figure 10.1.6: A photo showing the extent of weathering on the southwest face.

Figure 10.1.7. Shows the weathering on the southwest face tapering away at the top closer to the diabase intrusion.

10.2 Appendix B: Ternary plots data normalized to 100%.

Table 10.2.1. Fine-grained tonalite normalized data

Components	Raw data	Normalized data
	Sample CT1	
An	24.3	29.3
Ab	47.893	57.74
Or	10.756	12.97
Total	**82.949**	**100.01**
	Sample CT5	
An	22.5	26.8
Ab	53.055	63.2

Or	8.3917	10.0
Total	**83.9467**	**100.0**

Table 10.2.2. Medium-grained tonalite normalized data

Components	Raw data	Normalized data
	Sample CT7	
An	24.1	28.56
Ab	50.178	59.46
Or	10.105	11.98
Total	**84.383**	**100**
	Sample CT12	
An	23.9	28.56
Ab	48.147	57.53
Or	11.642	13.91
Total	**83.689**	**100.0**
	Sample CT14	
An	24.3	29.23
Ab	47.555	57.20
Or	11.287	13.58
Total	**83.142**	**100.01**
	Sample CT17	
An	18.5	23.60
Ab	48.316	61.63
Or	11.583	14.77
Total	**78.399**	**100.0**
	Sample CT22	
An	22.1	27.57
Ab	46.539	58.06
Or	11.524	14.38
Total	**80.163**	**100.01**
	Sample CT23	
An	22.0	27.33

Ab	46.962	58.35
Or	11.524	14.32
Total	**80.486**	**100.0**

Table 10.2.3. Coarse-grained trondhjemite normalized data

Components	Raw data	Normalized data
	Sample CT6	
An	14.6	19.36
Ab	52.547	69.67
Or	8.2735	10.97
Total	**75.4205**	**100.0**
	Sample CT9	
An	15.1	19.55
Ab	42.393	54.89
Or	19.738	25.56
Total	**77.231**	**100.0**
	Sample CT13	
An	15.1	19.52
Ab	50.093	64.75
Or	12.174	15.74
Total	**77.367**	**100.01**
	Sample CT16	
An	15.7	21.14
Ab	46.032	62.0
Or	12.528	16.87
Total	**74.26**	**100.01**
	Sample 20	
An	14.4	19.46
Ab	48.655	65.76
Or	10.933	14.78

Total	**73.988**	**100.0**
	Sample CT21	
An	13.9	18.92
Ab	44.847	61.05
Or	14.715	20.03
Total	**73.462**	**100.0**

Table 10.2.4. Granodiorite sheets normalized data

Components	Raw data	Normalized data
	Sample CT2	
An	16.3	23.50
Ab	30.97	44.64
Or	22.102	31.86
Total	**69.372**	**100.0**
	Sample CT3	
An	11.7	16.38
Ab	28.516	39.93
Or	31.203	43.69
Total	**71.419**	**100.0**
	Sample CT8	
An	14.0	19.55
Ab	31.562	44.10
Or	26.061	36.39
Total	**71.623**	**100.0**

10.3 Appendix C: Analytical standards.

Table 10.3.1. *Analytical standards for trace element whole rock data.*

	Values in ppm	Sc	V	Cr	Co	Ni	Cu	Zn	Rb
	Instrument DL	*0,007*	*0,006*	*0,054*	*0,003*	*0,033*	*0,011*	*0,033*	*0,001*
	Method DL (fusions)	*0,098*	*0,081*	*0,698*	*0,057*	*0,512*	*0,128*	*0,546*	*0,017*
Certified BCR-2G glass		**33,00**	**425,00**	**17,00**	**38,00**	**13,00**	**21,00**	**125,00**	**47,00**
	BCR-2G	32,61	406,59	15,06	37,75	12,00	17,39	140,70	47,26
	BCR-2G	31,97	408,98	14,87	37,85	11,96	17,29	149,93	47,42
	BCR-2G	33,47	415,35	15,13	37,51	12,04	17,27	151,81	46,40
	Average Analysed	**32,69**	**410,30**	**15,02**	**37,70**	**12,00**	**17,32**	**147,48**	**47,03**
	% Deviation	*1,0*	*3,5*	*11,6*	*0,8*	*7,7*	*17,5*	*18,0*	*0,1*
Certified BHVO-2G glass		**33,00**	**308,00**	**293,00**	**44,00**	**116,00**	**127,00**	**102,00**	**9,20**
	BHVO-2G	29,65	292,99	272,11	43,49	115,15	118,98	107,06	9,17
	BHVO-2G	30,13	292,72	269,84	43,69	118,13	123,37	111,02	9,07
	BHVO-2G	30,66	300,62	272,79	43,69	119,77	126,52	113,78	9,10
	Average Analysed	**30,14**	**295,44**	**271,58**	**43,63**	**117,68**	**122,96**	**110,62**	**9,11**
	% Deviation	*8,7*	*4,1*	*7,3*	*0,9*	*1,5*	*3,2*	*8,5*	*0,9*
Certified BHVO powder		**31,42**	**313,80**	**287,60**	**44,90**	**120,00**	**137,20**	**105,10**	**9,52**
	BHVO-1	31,19	327,85	301,30	45,33	126,77	135,15	100,97	9,09
	BHVO-1	31,55	329,87	303,53	45,26	131,07	137,72	116,54	9,17
	BHVO-1	31,31	322,85	293,48	44,17	129,43	133,07	110,50	8,66
	BHVO-1	29,43	303,08	270,63	40,27	123,60	125,39	100,14	8,21
	BHVO-1	30,25	311,39	275,05	43,11	123,69	129,02	112,80	8,77
	BHVO-1	30,07	303,44	272,42	40,70	120,68	123,32	107,11	8,44
	BHVO-1	32,24	332,53	294,23	45,17	129,64	134,29	113,81	9,16
	Average Analysed	**30,86**	**318,72**	**287,23**	**43,43**	**126,41**	**131,14**	**108,84**	**8,79**

	% Deviation	*1,8*	*1,6*	*0,1*	*3,3*	*5,3*	*4,4*	*3,6*	*7,7*
Certified BCR powder		**33,53**	**417,60**		**37,33**		**19,66**	**129,50**	**46,02**
	BCR-2	33,36	438,73		37,72		19,80	134,54	45,54
	BCR-2	34,00	421,44		36,75		20,81	148,40	44,48
	BCR-2	33,92	428,41		38,22		21,22	146,59	45,32
	BCR-2	31,92	398,33		35,10		21,26	139,00	41,72
	BCR-2	32,18	413,46		35,55		21,07	143,80	42,91
	BCR-2	34,40	434,65		38,06		20,50	149,04	45,30
	Average Analysed	**33,30**	**422,51**		**36,90**		**20,78**	**143,56**	**44,21**
	% Deviation	*0,7*	*1,2*		*1,2*		*5,7*	*10,9*	*3,9*

Table 10.3.2. *Analytical standards for whole rock major elements*

		Meas.date/time	Al_2O_3	CaO	Cr_2O_3	Fe_2O_3	K2O	MgO	MnO
BE-N **Basalt Reference values**			**9,98**	**13,99**		**12,70**	**1,42**	**13,06**	**0,20**
BE-N STD	MajorBasic32+Zn	2022/06/28 09:13	10,16	14,03	0,05	12,88	1,42	13,09	0,20
BE-N STD	MajorBasic32+Zn	2022/07/29 11:32	10,26	14,07	0,05	12,85	1,43	13,11	0,19
BE-N STD	MajorBasic32+Zn	2022/09/01 00:00	10,09	14,08	0,05	12,82	1,41	13,13	0,20
BE-N STD	MajorBasic32+Zn	2022/09/08 13:01	10,22	14,07	0,05	12,82	1,41	13,13	0,19
BE-N STD	MajorBasic32+Zn	2022/10/06 00:00	10,12	14,04	0,05	12,88	1,42	13,11	0,20
BE-N STD	MajorBasic32+Zn	2022/10/21 14:16	10,13	14,11	0,05	12,87	1,43	13,14	0,19
BE-N STD	MajorBasic32+Zn	2022/11/01 12:39	10,13	14,06	0,04	12,88	1,44	13,17	0,19
BE-N STD	MajorBasic32+Zn	2022/11/09 12:59	9,90	14,11	0,04	12,91	1,54	13,15	0,20
BE-N STD	MajorBasic32+Zn	2022/11/22 12:24	9,26	14,10	0,05	12,89	1,54	13,14	0,20

BE-N	**std**	MajorBasic32+Zn	2022/12/01 09:59	10,10	14,01	0,05	12,82	1,50	13,07	0,19
Average				10,04	14,07	0,05	12,86	1,45	13,12	0,20
Relative standard deviation (%)				0,55	0,56		1,28	2,25	0,49	2,60

JB-1				**14,53**	**9,33**	**0,07**	**8,99**	**1,42**	**7,81**	**0,15**
Basalt (depleted) Reference values										
JB-1	**std**	MajorBasic32+Zn	2022/06/28 09:22	14,88	9,31	0,06	8,88	1,45	7,89	0,16
JB-1	**std**	MajorBasic32+Zn	2022/07/29 11:41	14,65	9,30	0,06	8,88	1,46	7,87	0,16
JB-1	**std**	MajorBasic32+Zn	2022/09/01 00:00	15,03	9,29	0,06	8,89	1,44	7,89	0,16
JB-1	**STD**	MajorBasic32+Zn	2022/09/08 13:10	14,99	9,31	0,06	8,85	1,45	7,88	0,16
JB-1	**std**	MajorBasic32+Zn	2022/10/06 00:00	15,10	9,33	0,06	8,88	1,45	7,89	0,16
JB-1	**std**	MajorBasic32+Zn	2022/10/21 14:25	15,00	9,30	0,06	8,87	1,45	7,88	0,16
JB-1	**std**	MajorBasic32+Zn	2022/11/01 12:48	15,01	9,31	0,07	8,91	1,47	7,88	0,16
JB-1	**std**	MajorBasic32+Zn	2022/11/09 13:08	15,03	9,36	0,06	8,88	1,46	7,91	0,16
JB-1	**std**	MajorBasic32+Zn	2022/11/22 12:33	15,06	9,32	0,06	8,90	1,46	7,90	0,16
JB-1	**std**	MajorBasic32+Zn	2022/12/01 10:08	15,03	9,26	0,07	8,84	1,46	7,80	0,16
Average				14,98	9,31	0,06	8,88	1,46	7,88	0,16
Relative standard deviation (%)				3,08	0,23	8,82	1,25	2,46	0,92	7,10

BHVO-1

Basalt Reference values				**13,69**	**11,43**	**0,04**	**12,32**	**0,53**	**7,21**	**0,17**
BHVO-1	**std**	MajorBasic32+Zn	2022/06/28 09:31	14,00	11,45	0,04	12,36	0,53	7,22	0,16
BHVO-1	**std**	MajorBasic32+Zn	2022/07/29 11:50	14,01	11,43	0,04	12,35	0,52	7,26	0,17
BHVO-1	**std**	MajorBasic32+Zn	2022/09/01 00:00	13,98	11,42	0,04	12,31	0,52	7,26	0,17
BHVO-1	**std**	MajorBasic32+Zn	2022/09/08 13:19	14,06	11,44	0,04	12,29	0,52	7,25	0,17
BHVO-1	**std**	MajorBasic32+Zn	2022/10/06 00:00	14,02	11,43	0,04	12,31	0,53	7,24	0,17
BHVO-1	**std**	MajorBasic32+Zn	2022/10/21 14:34	14,01	11,47	0,04	12,31	0,53	7,26	0,17
BHVO-1	**std**	MajorBasic32+Zn	2022/11/01 12:57	14,11	11,45	0,04	12,34	0,53	7,32	0,17
BHVO-1	**std**	MajorBasic32+Zn	2022/11/09 13:17	13,95	11,45	0,04	12,34	0,53	7,31	0,16
BHVO-1	**std**	MajorBasic32+Zn	2022/11/22 12:42	14,03	11,43	0,04	12,30	0,53	7,27	0,17
BHVO-1	**std**	MajorBasic32+Zn	2022/12/01 10:17	13,93	11,40	0,04	12,30	0,52	7,12	0,17
Average				14,01	11,44	0,04	12,32	0,53	7,25	0,17
Relative standard deviation (%)				2,34	0,06		0,01	0,08	0,53	0,53

JG-1										
Granodiorite Reference values				**14,20**	**2,18**	**0,01**	**2,14**	**3,97**	**0,74**	**0,06**
JG-1	**std**	MajorBasic32+Zn	2022/06/28 09:40	14,70	2,18	bdl	2,09	4,00	0,66	0,06
JG-1	**std**	MajorBasic32+Zn	2022/07/29 11:59	14,49	2,17	bdl	2,09	4,00	0,67	0,06
JG-1	**std**	MajorBasic32+Zn	2022/09/01 00:00	14,77	2,16	0,01	2,09	4,01	0,66	0,07
JG-1	**std**	MajorBasic32+Zn	2022/09/08 13:28	14,75	2,15	bdl	2,08	3,99	0,66	0,06
JG-1	**std**	MajorBasic32+Zn	2022/10/06 00:00	14,74	2,17	0,01	2,09	4,02	0,66	0,06
JG-1	**std**	MajorBasic32+Zn	2022/10/21 14:43	14,80	2,16	bdl	2,10	4,05	0,66	0,07
JG-1	**std**	MajorBasic32+Zn	2022/11/01 13:07	14,73	2,16	bdl	2,10	4,06	0,66	0,07
JG-1	**std**	MajorBasic32+Zn	2022/11/09 13:26	14,76	2,16	0,01	2,10	4,05	0,66	0,07

JG-1 std	MajorBasic32+Zn	2022/11/22 12:51	14,55	2,18	0,01	2,10	4,04	0,67	0,06
JG-1 std	MajorBasic32+Zn	2022/12/01 10:27	14,68	2,17	0,01	2,08	4,01	0,67	0,06
Average			14,70	2,17	0,01	2,09	4,02	0,66	0,06
Relative standard deviation (%)			3,50	0,64	6,38	2,24	1,34	10,41	1,59

Quality control for 2010-2011									
Average HUSG		**1900/01/13 17:55**	**13,75**	**1,52**	**0,00**	**3,78**	**4,66**	**1,04**	**0,06**
STDEV		**1900/01/00 04:51**	**0,20**	**0,04**	**0,00**	**0,14**	**0,06**	**0,04**	**0,01**
MIN		**1900/01/13 00:57**	**13,04**	**1,48**	**0,00**	**3,64**	**4,55**	**0,94**	**0,05**
MAX		**1900/01/14 07:06**	**14,30**	**1,63**	**0,01**	**4,56**	**4,80**	**1,22**	**0,08**
HUSG-1 STD	MajorBasic32+Zn	2022/06/02 21:39	14,22	1,55	bdl	3,73	4,64	1,01	0,06
STD HUSG-1	MajorBasic32+Zn	2022/06/06 12:35	14,19	1,56	bdl	3,73	4,65	1,02	0,05
HUSG-1 std	MajorBasic32+Zn	2022/06/21 14:39	14,19	1,55	bdl	3,72	4,65	1,03	0,06
HUSG-1 std	MajorBasic32+Zn	2022/06/24 20:57	14,13	1,55	bdl	3,71	4,63	1,01	0,06
HUSG-1 std	MajorBasic32+Zn	2022/09/01 00:00	14,20	1,55	bdl	3,71	4,62	1,01	0,05
HUSG-1 STD	MajorBasic32+Zn	2022/10/06 00:00	14,18	1,55	bdl	3,73	4,64	1,02	0,05
HUSG-1 STD	MajorBasic32+Zn	2022/10/21 15:40	14,18	1,57	bdl	3,74	4,68	1,02	0,05
HUSG-1 std	MajorBasic32+Zn	2022/10/28 21:02	14,39	1,58	bdl	3,82	4,63	1,03	0,06
HUSG-1 std	MajorBasic32+Zn	2022/11/09 12:50	14,28	1,55	bdl	3,72	4,70	1,02	0,06
HUSG-1 std	MajorBasic32+Zn	2022/11/22 16:51	14,25	1,56	0,00	3,70	4,71	1,04	0,05
Average			14,22	1,56	0,00	3,73	4,66	1,02	0,06
Relative standard deviation (%)			3,45	2,34	100,00	1,20	0,01	2,21	14,63

10.4 Appendix D: Sample CT17 zircon spot analysis data

CT17 zircons	**$^{207}Pb\_^{235}U$**	**$^{207}Pb\_^{235}U$**	**$^{206}Pb\_^{238}U$**	**$^{206}Pb\_^{238}U$**	**$^{207}Pb\_^{206}Pb$**	**$^{207}Pb\_^{206}Pb$**
CT-17_90 - 1	2216	21	1724	30	2716	25
CT-17_91 - 1	3070	28	2888	74	3200	26
CT-17_92 - 1	2811	27	2468	48	3072	17
CT-17_93 - 1	3365	27	3239	88	3449	23
CT-17_94 - 1	3432	15	3437	47	3437	16
CT-17_95 - 1	2604	14	2145	35	2985	19
CT-17_96 - 1	1007	36	417	26	2460	30
CT-17_98 - 1	1938	12	1475	19	2484	13
CT-17_99 - 1	2166	14	1685	22	2654	16
CT-17_100 – 1	1618	11	1137	14	2316	13
CT-17_101 - 1	2903	23	2742	59	3026	19
CT-17_102 - 1	2481	26	1699	32	3209	19
CT-17_103 - 1	3401	10	3326	32	3444	11
CT-17_104 - 1	3204	12	3202	40	3213	14
CT-17_109 - 1	2076	15	1452	29	2777	21
CT-17_110 - 1	2967	15	2723	36	3136	12
CT-17_111 - 1	2211	18	1789	31	2621	18
CT-17_112 - 1	2510	25	1650	46	3123	27
CT-17_113 - 1	2196	21	1696	35	2709	13
CT-17_114 - 1	2537	31	2108	57	2906	29
CT-17_115 - 1	3413	13	3412	35	3408	11

CT-17_117 - 1	2478	23	1956	40	2940	20
CT-17_118 - 1	3252	21	2975	64	3435	24
CT-17_119 - 1	2589	18	1869	37	3223	18
CT-17_120 - 1	2604	13	2124	25	3001	14
CT-17_121 - 1	2121	18	1563	29	2726	11
CT-17_122 - 1	1977	20	1178	26	2970	32
CT-17_124 - 1	3398	26	3287	80	3476	20
CT-17_125 - 1	1923	17	1410	22	2531	14
CT-17_127 - 1	2611	14	2200	24	2952	14
CT-17_128 - 1	3313	17	2909	51	3560	17
CT-17_129 - 1	2004	25	1459	29	2617	19
CT-17_130 - 1	2658	17	2365	35	2892	12
CT-17_131 - 1	2879	22	2514	57	3155	22
CT-17_132 - 1	2063	13	1527	21	2652	13
CT-17_133 - 1	1184	56	554	25	2618	69
CT-17_134 - 1	2500	20	1961	43	2981	30
CT-17_135 - 1	2378	17	1426	25	3342	16
CT-17_136 - 1	3407	12	3400	37	3409	13
CT-17_137 - 1	1420	30	847	29	2453	16
CT-17_141 - 1	3049	18	3005	39	3081	14
CT-17_143 - 1	2433	24	1987	35	2824	19
CT-17_144 - 1	3283	14	3204	42	3339	14
CT-17_146 - 1	2700	13	2135	30	3160	12

CT-17_148 - 1	3384	20	3387	51	3383	17
CT-17_152 - 1	2359	23	124,9	6,7	11070	320
CT-17_153 - 1	3272	17	3115	42	3374	13
CT-17_155 - 1	2394	25	2122	52	2638	20
CT-17_157 - 1	3212	30	3090	59	3297	15
CT-17_159 - 1	3326	20	3090	63	3479	23
CT-17_161 - 1	2939	12	2512	30	3245	11
CT-17_162 - 1	1796	25	1277	39	2477	26
CT-17_166 - 1	3134	17	2788	45	3370	17
CT-17_167 - 1	3333	14	3245	40	3390	13
CT-17_173 - 1	2627	22	2121	35	3041	16
CT-17_174 - 1	3040	20	2778	43	3235	17
CT-17_175 - 1	2529	14	2079	24	2918	13
CT-17_176 - 1	1802	88	1006	67	2828	73
CT-17_178 - 1	3167	22	2930	66	3332	22
CT-17_186 - 1	2874	14	3105	42	2726	13
CT-17_189 - 1	2754	13	2586	32	2884	11
CT-17_194 - 1	3034	22	2710	52	3275	19
CT-17_199 - 1	2825	17	2181	41	3329	21
CT-17_206 - 1	2171	13	1638	21	2724	13
CT-17_207 - 1	2797	33	2237	58	3230	18
CT-17_210 - 1	2996	33	2845	66	3119	26
CT-17_213 - 1	2673	15	2275	37	3001	17

CT-17_218 - 1	2976	59	2614	93	3243	41
CT-17_221 - 1	3286	17	3285	57	3287	15
CT-17_223 - 1	2893	17	2451	39	3215	12
CT-17_226 - 1	2136	17	1608	19	2697	21
CT-17_231 - 1	2848	27	2453	49	3154	21

10.5 Appendix C: Research Ethics Declaration

RHODES UNIVERSITY

Where leaders learn

RESEARCH ETHICS DECLARATION

To be included in the Appendices of research papers / dissertations / theses submitted for postgraduate examination where research did not involve interaction with human participants, or the use of animal subjects, and therefore did not require research ethics approval. Candidates whose research did require ethics clearance must include their ethics approval letter in the Appendix of their examination submission.

Name of Candidate: T.Mofammere

Name of Supervisor: Dr E Grosch

Degree: MSc

Title of research: see above thesis

DECLARATION

I declare that my research did not require ethical clearance because (tick all that apply):

I used previously collected data that had already received ethics clearance.	
I analysed documents / open-access digital texts that are freely available in the public domain.	
I did a literature review/analysis of theoretical or secondary material only.	
I used human datasets of non-sensitive information that are either anonymous (identifiers were never collected) or have been deidentified (identifiers have been completely removed).	
I used commercially produced human biological material (e.g. established human cell lines).	
I observed people in public spaces and natural environments where they had no reasonable expectation of privacy and I did not interact with them or intervene in any way.	
I used non-living animal materials (eg bones of already deceased organisms or fossils) while complying with any custody and/or jurisdiction requirements.	
I did a content analysis of public media (newspapers, advertisements, and social media posts).	
I did a simulation study with no real-world consequences and does not involve disturbing or distressing content.	
I observed flora, fauna, and ecosystems without interfering with or disturbing their natural state while complying with any jurisdiction requirements.	
Other: This MSc study sampled rocks and thus does not require research ethics approval	X

Signature of Candidate: T. Mofammere.

Date: 28 November 2024

Signature of Supervisor:

Date: 27 November 2024